

國立交通大學

電子物理學系

博士論文

自鎖模雷射的研究與應用

Investigations and Applications of Self-Mode-Locked Lasers

研究生：梁興弛

指導教授：陳永富 教授

中華民國九十九年五月

自鎖模雷射的研究與應用

Investigations and Applications of Self-Mode-Locked Lasers

研 究 生：梁興弛

Student：Hsing-Chih Liang

指 導 教 授：陳永富

Advisor：Yung-Fu Chen

國 立 交 通 大 學

電 子 物 理 學 系

博 士 論 文

A Dissertation

Submitted to Department of Electrophysics

College of Science

National Chiao Tung University

in partial Fulfillment of the Requirements

for the Degree of

Doctor of Philosophy

in

Electrophysics

May 2010

Hsinchu, Taiwan, Republic of China

中華民國九十九年五月

自鎖模雷射的研究與應用

學生：梁興弛

指導教授：陳永富

國立交通大學電子物理學系博士班

摘 要

本文主要是藉由 Nd:YVO₄ 和 Nd:GdVO₄ 較高的第三階非線性特性，搭配簡易的直線型雷射共振腔，且無須外加額外的元件，成功實現高重複率 (GHz) 自鎖模雷射。在 2.5W 激發功率下，可以產生 0.8W 的輸出，其波長為 1064nm，脈衝寬度 7.8ps；除了 1064nm 波段之外，在 10.2W 激發功率，亦產生了 1342nm 的 1.2W 雷射輸出，其脈衝寬度為 12ps。接著利用空間燒孔效應 (spatial hole burning effect) 來控制雷射輸出的縱模數，藉由縱模數目的控制來穩定自鎖模雷射，除了實驗結果外，這裡也建構了理論架構，且與實驗結果吻合。透過這個穩定的自鎖模雷射，本文也提出一個量測可穿透式晶體的折射率及熱光係數 (thermal optical coefficient) 的方法，其主要方法是利用自鎖模雷射重複率的改變來推算出。接著我們利用離軸激發方式，產生具有高階橫向 Hermite-Gaussian (HG) 模態的自鎖模雷射，並且藉由一對柱面鏡，在腔外將其轉換成帶有軌道角動量的高階 Laguerre-Gaussian 模態，透過這樣的腔外轉換，可以產生皮秒的光束漩渦。除此之外，我們也利用當有兩個高階模態偶合時，其自鎖模雷射所產生的拍頻現象來量測晶體的熱透鏡焦距。

Investigations and Application of Self-Mode-Locked Lasers

Student : Hsing-Chih Liang

Advisor : Yung-Fu Chen

Department of Electrophysics
National Chiao Tung University

ABSTRACT

The large third-order nonlinearities of Nd:YVO₄ and Nd:GdVO₄ are employed to realize the compact efficient self-mode-locking in the range of several GHz in solid-state lasers with a simple linear cavity. With a pump power of 2.5 W, the lasers produce greater than 0.7 W with the pulse width in the picosecond region at the operating wavelength of 1064 nm. Furthermore, we also have demonstrated the self-mode-locked Nd:YVO₄ laser at 1342 nm. The average output power was up to 1.2 W at an incident pump power of 10.2 W. The pulse width was experimentally found to be less than 12ps.

In order to improve the stability of self-mode-locked lasers, we have demonstrate the control of Nd:YVO₄ laser. The experimental results reveal that reducing the number of longitudinal lasing modes can diminish the fluctuation to effectively improve the pulse stability. Considering the spatial hole burning (SHB) effect, an analytical expression is derived to accurately estimate the maximum number of longitudinal lasing for a practical design guideline. Therefore, the stable self-mode-locked laser can induce a novel method to measure the refractive indexes and thermal optical coefficient of certain crystals. The experimental results are in good agreement with the results in texts.

Besides the fundamental mode self-mode-locked lasers, we have reported the self-mode-locked Hermite-Gaussian Nd:YVO₄ lasers with an off-axis pumping scheme. With a pump power of 2.2 W, the average output power for 3.5 GHz mode-locked HG modes vary in the range of 350-780 mW for the TEM_{0,m} modes from $m=9$ to $m=0$. We also use simple astigmatic mode converters (AMC) to convert the mode-locked HG TEM_{0,m} beams in to Laguerre-Gaussian (LG) modes for generating picosecond optical vortex pulses. Furthermore, the modulated pulse trains are observed as there are two adjacent transverse modes coupling. The modulated frequencies can apply to determination of thermal lens in mode-locked lasers.

誌謝

Acknowledgement

五年的時間一轉眼就過了，首先十分感謝陳永富老師，提供了一個非常好的研究環境，讓我可以無憂無慮的做研究，老師親切的指導，總是讓我能迅速地更深入了解研究的內容，同時，老師對研究的熱情也感染了我，令我常常因觀察到有趣的現象而感到興奮。在擔任老師的助教時，老師也常常花時間陪我討論，讓我在這些基礎的科目上打下了穩固的根基。除此之外，在生活上老師也非常照顧我，關心宿舍的情況、身體的狀況等等，真的非常感謝陳永富老師。

同時我也非常感謝黃凱風老師對我的指導，在實驗上除了提供研究所需要用的半導體元件外，黃老師對實驗總是有令人驚豔的想法，常常使一些看似一般的實驗變得更深入、更有趣。黃老師和藹可親的風範以及淵博的知識，更是令我非常的景仰。

兩位老師認真研究的態度，是我學習的最佳典範，往後的日子，我會繼續努力，在這個實驗室裡我學習到了許多的事情，讓我獲益良多，說再多次的謝謝也無法表達心中對陳永富老師和黃凱風老師的感謝。

在實驗室裡，除了兩位恩師之外，也要感謝許多人對我的幫助。首先要感謝冠暉老大從一開始便帶著我做實驗，你在實驗上細心及認真的態度，是我學習的模範；感謝哲彥學長，跟著你做了許多的實驗，你總是親切的指導我，令我受益匪淺；感謝亭樺學姊、仕璋學長，不論是在生活上或實驗上都給了我很大的協助；感謝以前的學長姐國欽、偉立、玲意、美玲，在我一年級時對我的照顧；當然還要感謝一起奮鬥的戰友們建誠、依萍、雅婷、恩毓，在這一路上互相的討論與切磋；此外還要感謝阿龍學長、文政、彥廷、小江、易純、毅帆、威哲、家禎、郁仁、毓捷、建至、昆毅，和你們討論實驗及課業，常常讓我收穫滿滿。

感謝我的太太瑋菱，謝謝妳一路上的陪伴與鼓勵，讓我有前進的動力。最後，感謝我摯愛的雙親，可以讓我無後顧之憂完成學業，要感謝的人太多，在此再次謝謝這一路上給與我協助的良師益友們！

Contents

Abstract	i
Contents	iv
List of Figures	vii
List of Tables	xii
Chapter1	Introduction.....	1
1.1	Mode-Locked Lasers.....	2
1.2	Transverse Modes of Laser Cavity.....	11
1.3	Beam Transformation.....	17
1.4	Overview of Thesis.....	23
Reference	25
Chapter2	Continuous-Wave Self-Mode-Locked Lasers.....	29
2.1	Phenomenon of Spontaneous Mode Locking.....	30
2.2	High Power Self-Mode-Locked Multi-GHz Nd:YVO ₄ and Nd:GdVO ₄ Lasers.....	32
2.2.1	Experimental Setup.....	33
2.2.2	Experimental Results and Discussions.....	35
2.3	Diode-Pumped Self-Mode-Locked Laser at 1342 nm.....	42
2.3.1	Experimental Setup.....	43
2.3.2	Experimental results and Discussions.....	45
2.4	Conclusion.....	51
Reference	53

Chapter3	Controlling the Number of Longitudinal Modes for Designing Reliable Self-Mode-Locked Lasers.....	57
3.1	Influence of the Number of Longitudinal Modes on the Self-Mode- Locked Lasers.....	58
3.2	Experimental Setup.....	61
3.3	Stability Improvement and Pulse Width Control for Short-Cavity Self-Mode-Locked Nd:YVO ₄ Lasers.....	64
3.4	Theoretical Model for Estimating the Maximum Longitudinal Lasing Modes in Self-Mode-Locked Lasers.....	71
3.5	Conclusion.....	79
Reference	80
Chapter4	Application of Self-Mode-Locked Lasers: Measurements of Refractive Indexes and Thermal Optical Coefficient.....	82
4.1	Refractive Index and Thermal Optical Coefficient.....	83
4.2	Experimental Setup.....	85
4.3	Experimental Results and Analysis.....	88
4.4	Conclusion.....	95
Reference	96
Chapter5	Self-Mode-Locked Lasers for High-Order Transverse Modes.....	99
5.1	Paraxial Approximation Maxwell's Equation : Wave Functions of Spherical Laser Cavity.....	100
5.2	Self-Mode-Locked High-Order Hermite-Gaussian Nd:GdVO ₄ Lasers.....	108
5.2.1	Theoretical Simulation of Mode-locked Laser for High-Order Hermite-Gaussian Modes.....	108
5.2.2	Experimental Setup.....	111

	5.2.3	Experimental Results and Discussions.....	114
5.3		Beam Transformation of Self-Mode-Locked Lasers : Picosecond Vortex Pulses.....	121
	5.3.1	Experimental Setup.....	122
	5.3.2	Experimental results and Analysis.....	122
5.4		Conclusion.....	128
Reference		129
Chapter6		Determination of Thermal Lens with Transverse Beat Frequencies: Application of the Self-Mode-Locked High-Order HG modes Lasers.....	133
6.1		Thermal Lens Effect.....	133
6.2		Experimental Setup.....	137
6.3		Experimental Results and Analysis.....	139
6.4		Conclusion.....	147
Reference		148
Chapter7		Summary and Future Work.....	152
7.1		Summary.....	153
7.2		Future Work.....	156

Curriculum Vitae

Publication List

List of Figures

Chapter1

Fig. 1.1-1.	Signal of a non-mode-locked laser. (a) In the frequency domain the intensities of the modes and the phase have a random distribution. (b) In the time domain the intensity has a random distribution of maximum.....	3
Fig. 1.1-2.	Signal of an ideally mode-locked laser. (a) In the frequency domain the intensities of the modes have a Gaussian distribution and the spectral phases are identically zero. (b) In the time domain the output signal is a transform-limited Gaussian pulse.....	4
Fig. 1.1-3.	The output intensity of a mode-locked laser pulse plotted as a function of time for the case of $N=3, 5,$ and 7 modes.....	8
Fig. 1.2-1.	The transverse mode patterns of Hermite-Gaussian modes with different order.....	12
Fig. 1.2-2.	The transverse mode patterns of Laguerre-Gaussian modes with different orders.....	13
Fig. 1.2-3.	The vortex beam of $LG_{0,1}$. (a) The intensity distribution. (b) The phase diagram. (c) The vector field structure.....	15
Fig. 1.3-1.	Numerical result according to Eq. (1.3.1). (a) Numerical result of $LG_{0,1}$. (b) Numerical result of $LG_{0,5}$	19
Fig. 1.3-2.	Conventional mode converter. (a) The spiral phase plate. (b) The sketch of computer-generated hologram.....	20
Fig. 1.3-3.	Diagram of Hermite-Gaussian modes convert into Laguerre- Gaussian mode by use of cylindrical lenses. (a)-(c) Numerical results of Hermite-Gaussian modes before transformation. (a')-(c') Numerical results of Laguerre- Gaussian modes after transformation.....	22

Chapter2

Fig.2.2-1.	Experimental setup for a diode-pumped self-mode-locked laser.....	34
Fig.2.2-2.	Pulse trains on two different timescales. (a) Time span of 5 μ s, demonstrating the amplitude oscillation. (b) Time span of 10 ns, demonstrating mode-locked pulses. (c) Power spectrum.....	36
Fig.2.2-3.	Same as Fig. 2.2-2 for the stable CW mode-locked operation.....	38
Fig.2.2-4.	(a) Average output powers versus incident pump power with the cavity alignments for maximum output and stable CW mode locking, respectively. (b) Corresponding optical spectrum of the mode locking. (c) Mode-locked pulse trains in time span of 1 ns. (d) Autocorrelation trace.....	40
Fig.2.2-5.	Experimental time trace for the multiple-pulse mode-locked operation at the cavity length of 11.3 cm.....	41
Fig.2.3-1.	Schematic of a diode-pumped self-mode-locked Nd:YVO ₄ laser at 1342 nm.....	44
Fig.2.3-2.	Average output power at 1342 nm versus incident pump power in maximum output power operation and mode-locked operation.....	46
Fig.2.3-3.	Pulse trains on two different time scales. (a) Time span of 5 μ s, demonstrating amplitude oscillation. (b) Time span of 5 ns, demonstrating mode-locked pulses. (c) Corresponding power spectrum.....	49
Fig.2.3-4.	(a) Autocorrelation trace of the output pulse from the cw mode-locked Nd:YVO ₄ laser. (b) Corresponding optical spectrum of the laser.....	50

Chapter3

Fig.3.1-1.	Output pulses in the ideal mode-locked operation and nonideal mode-locked operation with different longitudinal modes. (a) 5 longitudinal modes. (b) 10 longitudinal modes. (c) 30 longitudinal modes.....	60
Fig.3.2-1.	Schematic of a diode-pumped self-mode-locked Nd:YVO ₄ laser.....	63
Fig.3.3-1.	(a) Pulse trains for time span 2 ns, demonstrating the mode-locked pulses.	

	(b) Corresponding power spectrum.....	65
Fig. 3.3-2.	Optical spectrum for different crystal/mirror separations d . (a) $d = 1$ mm. (b) $d = 2$ mm. (c) $d = 5$ mm. (d) $d = 9$ mm.....	66
Fig. 3.3-3.	Mode-locked pulse width and bandwidth as function of crystal/mirror separation.....	67
Fig. 3.3-4.	Mode-locked pulse trains and power spectrum for two different crystal/mirror separation d . (a) Pulse trains of time span $5 \mu\text{s}$ for $d = 1$ mm . (b) Corresponding power spectrum. (c) $d = 11$ mm . (d) Corresponding power spectrum.....	69
Fig. 3.3-5.	Relative frequency deviation of the power spectrum $\Delta\nu/\nu$	70
Fig. 3.4-1.	Calculated results for $G_{res}(x, y, z, N)$ (darkred line) and $\langle I_N(x, y, z) \rangle$ (bule line) as function of z with $N = 11$, $x = y = 0$, and $m_0 = 200$	74
Fig. 3.4-2.	Calculated results for $\eta_{res}(N, d)$ as a function of N for several different value of d for the case of the Nd:YVO ₄ laser: $l_{cav} = 29$ mm , $l_g = 6$ mm , and $\alpha = 0.5$ mm ⁻¹	77
Fig. 3.4-3.	Theoretical estimations and experimental data for the maximum number of modes N_{max} as function of d	78
Chapter4		
Fig. 4.2-1.	The configuration of the refractive indexes measuring system.....	87
Fig. 4.3-1.	The experimental results for measuring refractive indexes of Nd:YVO ₄ with different doped concentrations. (a) For ordinary refractive indexes. (b) For extraordinary refractive indexes.....	93
Fig. 4.3-2.	Frequency shift versus the temperature of oven.....	94
Chapter5		
Fig. 5.1-1.	(a) Hermite-Gaussian modes with different order (m, n) . (b) Standing wave of Laguerre-Gaussian modes with different order (p, l)	107

Fig. 5.2-1.	The numerical results of the intensity $I_{0,0,5}(x, y, z)$. (a) In x-y plane. (b) In z-y plane.....	110
Fig. 5.2-2.	Resonator frequencies, demonstrating the mode-locking for fundamental mode and high-order transverse mode.....	112
Fig. 5.2-3.	The numerical results of the intensity of mode-locked laser for HG $TEM_{0,5}$. (a) In x-y plane. (b) In z-y plane at different time, where Tr is the round-trip time.	113
Fig. 5.2-4.	Schematic of a self-mode-locked high-order HG $TEM_{0,m}$ laser with an off-axis pumping scheme.	115
Fig. 5.2-5.	Dependence of the average output power on the variation off-axis displacement. Insert, transverse patterns observed in the mode-locked operation.	117
Fig. 5.2-6.	Pulse trains on two different time scales. (a) time span of 5 μ s, demonstrating the amplitude oscillation. (b) Time span of 5 ns, demonstrating the mode-locked pulses. (c) Autocorrelation trace of the output pulses. (d) Corresponding optical spectrum. All results are for HG $TEM_{0,5}$ mode.	118
Fig. 5.2-7.	Transverse patterns and pulse trains observed in the modulated mode-locked operation. (a) Transverse pattern of coupling TEM_{00} and TEM_{10} modes. (b) Time span of 50 ns, demonstrating, demonstrating the modulated amplitude oscillation. (c) Time span of 10 ns, demonstrating the mode-locked pulses.	120
Fig. 5.3-1.	Schematic of a cylindrical-lens mode converter.	124
Fig. 5.3-2.	Examples of the decomposition of HG beam with different transverse index $(n, m) = (0,1), (0,2), (0,3)$	125
Fig. 5.3-3.	The numerical simulations of the LG modes are reconstructed from HG modes.	126
Fig. 5.3-4.	The transformation of HG modes to LG modes. (a) The transverse patterns observed in mode-locked operation. (b) Corresponding transverse patterns	

after converting.	127
------------------------	-----

Chapter6

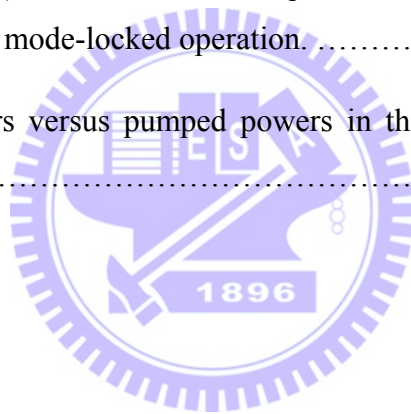
Fig. 6.2-1. Experimental setup of a self-mode-locked Nd:YVO ₄ laser for measuring the focal length of thermal lens of the gain medium.....	138
--	-----

Fig. 6.3-1. Transverse patterns and pulse trains observed in the stable and modulated mode-locked operation. (a) Transverse pattern of pure fundamental mode. (b) Time span of 50 ns, demonstrating stable cw mode-locked pulses. (c) Transverse patterns of coupling TEM ₀₀ and TEM ₁₀ modes. (d) Time span of 50 ns demonstrating modulated mode-locked pulses.	140
---	-----

Fig. 6.3-2. Power spectrum in the modulated mode-locked operation.	143
--	-----

Fig. 6.3-3. (a) Average output powers versus the pumped powers for the modulated mode locking. (b) Transverse beat frequencies versus the pumped powers in the modulated mode-locked operation.	144
---	-----

Fig. 6.3-4. The focal powers versus pumped powers in the modulated mode-locked laser.	146
---	-----



List of Tables


Chapter4

Table.	The experimentally measuring refractive indexes for different material at	
4.3-1.	operating wavelength of 1064 nm and 1342 nm.....	92



Chapter 1

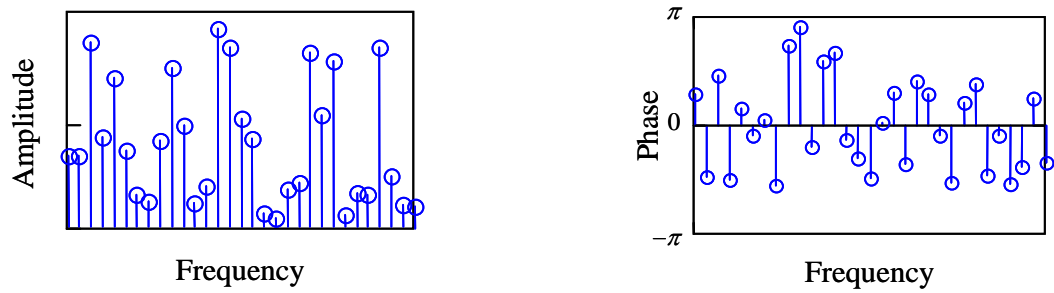
Introduction



1.1 Mode-Locked Laser

Ultrashort pulses with pulse duration in picosecond and femtosecond regime are obtained from solid-state lasers by mode-locking. This is a technique to obtain temporal control over the laser beam. It is achieved by controlling the relative phases and magnitudes of various longitudinal modes in the laser. Thus, this is the most efficient in lasers with numerous longitudinal modes running under the gain curve. In a free-running laser, the longitudinal modes oscillate without fixed mode-to-mode amplitude and phase. The resulting laser output is a time averaged statistical mean value. In Fig. 1.1-1 the spectral and temporal structure of the radiation inside a laser cavity are shown for a non-mode-locked laser. In the frequency domain, the radiation consists a large number of discrete spectral lines spaced by axial mode interval $c/2L$. Each mode oscillates independent of the others and the phases are randomly distributed in the range $-\pi$ to $+\pi$. In the time domain, the distribution of intensity shows a random distribution of maxima. On the other hand, by establishing a fixed-phase relationship among the longitudinal modes, a powerful well-defined single pulse circulating in the cavity can be generated. The laser is then said to be “mode-locked” or “phase locked.” Figure 1.1-2 demonstrates the output of an ideally mode-locked laser. The spectral amplitudes have a Gaussian distribution and the spectral phases are identically zero. In the time domain the output signal is a Gaussian pulse. As shown in figure, when all the initial randomness has been removed, the

(a)



(b)

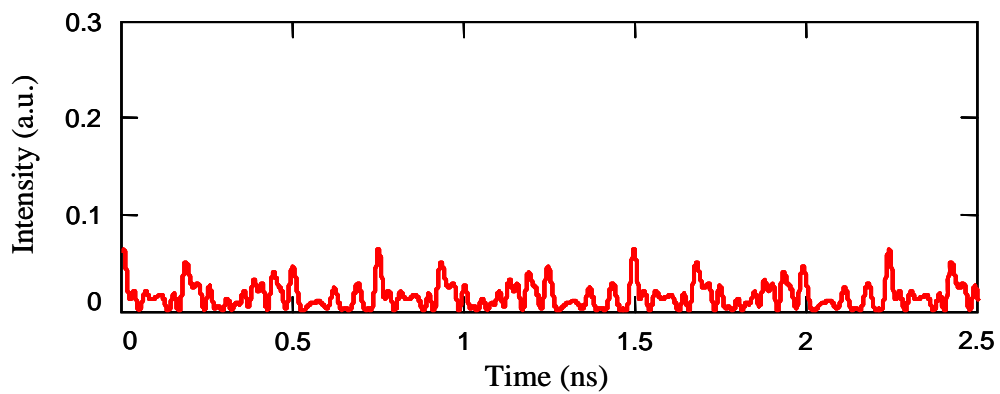


Fig. 1.1-1. Signal of a non-mode-locked laser. (a) In the frequency domain the intensities of the modes and the phase have a random distribution. (b) In the time domain the intensity has a random distribution of maximum.

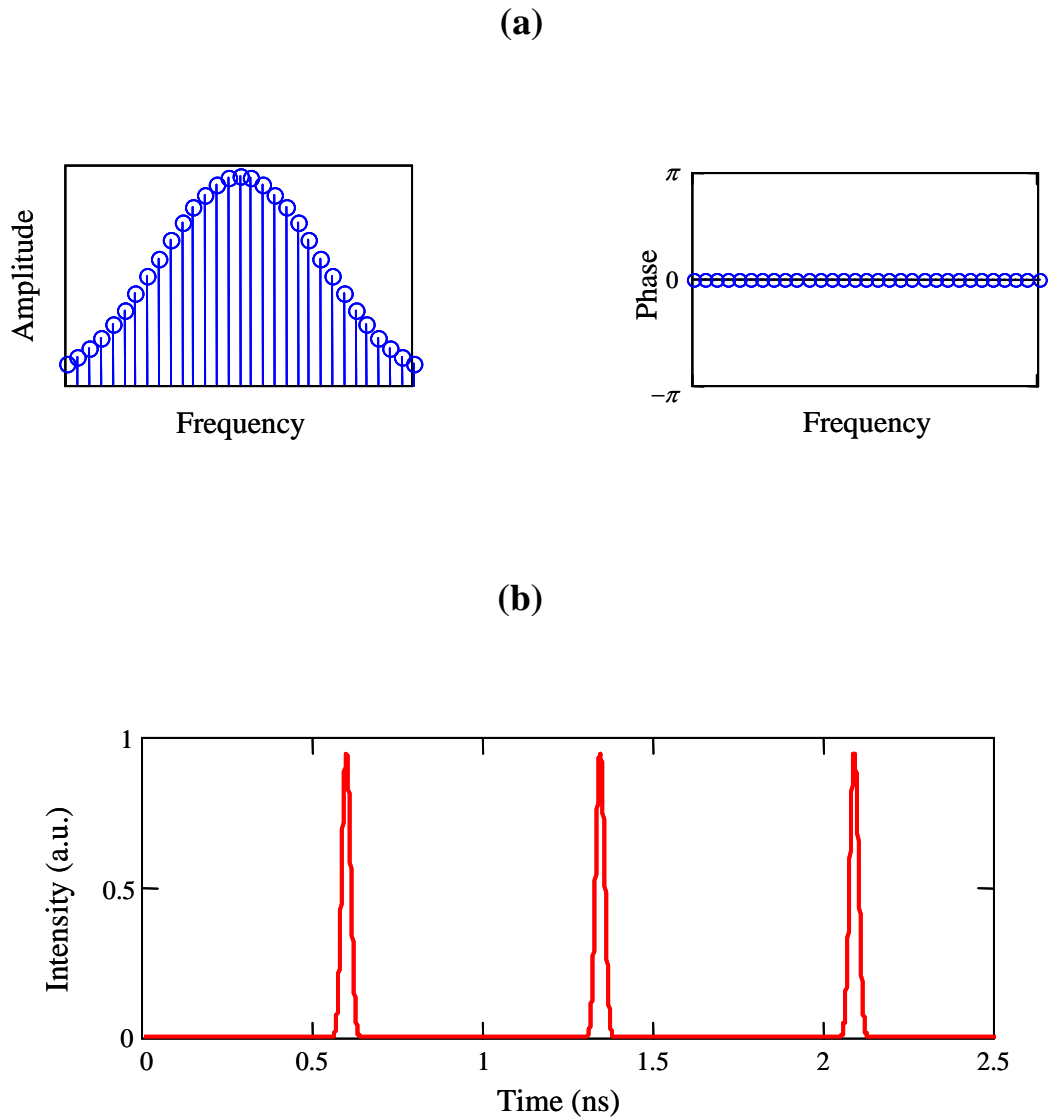


Fig. 1.1-2. Signal of an ideally mode-locked laser. (a) In the frequency domain the intensities of the modes have a Gaussian distribution and the spectral phases are identically zero. (b) In the time domain the output signal is a transform-limited Gaussian pulse.

longitudinal modes are locked and the radiation is localized in space in the form of a single pulse.

Mode-locking requires a mechanism that results in a lower loss for a more intensive radiation peak compared to the average intensity in the cavity. In passive mode-locking, it consists of a real or effective saturable absorber which generates a periodic modulation that forces the longitudinal modes to maintain fixed phase relationship. Real saturable absorbers are materials such as organic dyes, crystal, and semiconductor. The effective absorbers utilize the nonlinear refractive index of optical materials with spatial dependent loss mechanism. In active mode-locking, the electro-optical and acousto-optical modulator similar to those described for Q-switching can be also used for mode-locking. They induce a modulation of the amplitude (AM) or frequency (FM) of longitudinal modes that lead to higher gain for a mode-locked pulse train compared to cw operation.

The analytical description of mode-locking can be expressed as the sum of the electric field of all the various longitudinal modes. If the laser is restricted to a single transverse mode but that is oscillating at $N = 2M + 1$ longitudinal modes. Above and below the center frequency, there are $\pm M$ additional modes, whereby adjacent modes have a angular frequency separation ($\omega_{FSR} = 2\pi/T_r$) where T_r is the round trip time in the cavity ($Tr = 2L/c$). Thus, the electric field at an arbitrary point can be written as

$$E(t) = \sum_{n=-M}^M E_n e^{i(\omega_o + n \cdot \omega_{FSR}) t + \phi_n} \quad (1.1.1)$$

where ω_o is the frequency at the center of the gain bandwidth curve, E_n , and ϕ_n are the electric field amplitude and the phase of the n_{th} mode. Generally, the amplitude and the phase of different longitudinal modes are random with time. This causes the non-mode-locked laser as shown in Fig. 1.1-1. In a mode-locked laser, all the phase of the modes are equal. Thus, the random-looking temporal signal changes to one with well-defined pulse every round trip. The more longitudinal modes are available in the summation, the narrower and more well-defined the pulses are. To estimate the pulse width of the pulse, assume the phase of the center mode to be zero, $\phi_n = 0$. We also assume that all of the modes have the same magnitudes $E_n = E_0$.

Total electric field can then be written as

$$E(t) = E_0 \sum_{n=-M}^M e^{i(\omega_o + n \cdot \omega_{FSR})t} \quad (1.1.2)$$

This summation is a series with a known solution for a finite sum. Substituting the solution yields

$$E(t) = E_0 e^{i\omega_o t} \left(\frac{\sin \frac{N}{2} \omega_{FSR} t}{\sin \frac{1}{2} \omega_{FSR} t} \right) \quad (1.1.3)$$

The intensity of the laser is then given as

$$I(t) = E(t)E^*(t) = E_0^2 \left(\frac{\sin \frac{N}{2} \omega_{FSR} t}{\sin \frac{1}{2} \omega_{FSR} t} \right)^2 \quad (1.1.4)$$

Figure 1.1-3 demonstrates an example of the output intensity of a mode-locked laser in 6.18 cm optically long cavity for the case of $N = 3, 5,$ and 7 modes. The pulse train with a repetition rate 2.43 GHz and the pulse widths at the half power are 100 ps, 60 ps, and 33 ps respectively. In particular, the pulse width at the half power t_p is approximately

$$t_p \approx T_r / N \approx 1 / \Delta \nu \quad (1.1.5)$$

where $\Delta \nu$ is the gain bandwidth of the laser. Short mode-locked pulses require a large spectral bandwidth. This assumes a perfectly mode-locked laser that all longitudinal modes within the bandwidth are locked. The exact solution for the time/bandwidth product for phase locked modes of equal intensities has to be found numerically:

$$t_p \Delta \nu = 0.886 \quad (1.1.6)$$

If the intensities of the phase-locked modes have a Gaussian distribution, it has been shown that the results mode-locked pulse has also Gaussian distribution and the time/bandwidth product is given by

$$t_p \Delta \nu = 0.44 \quad (1.1.7)$$

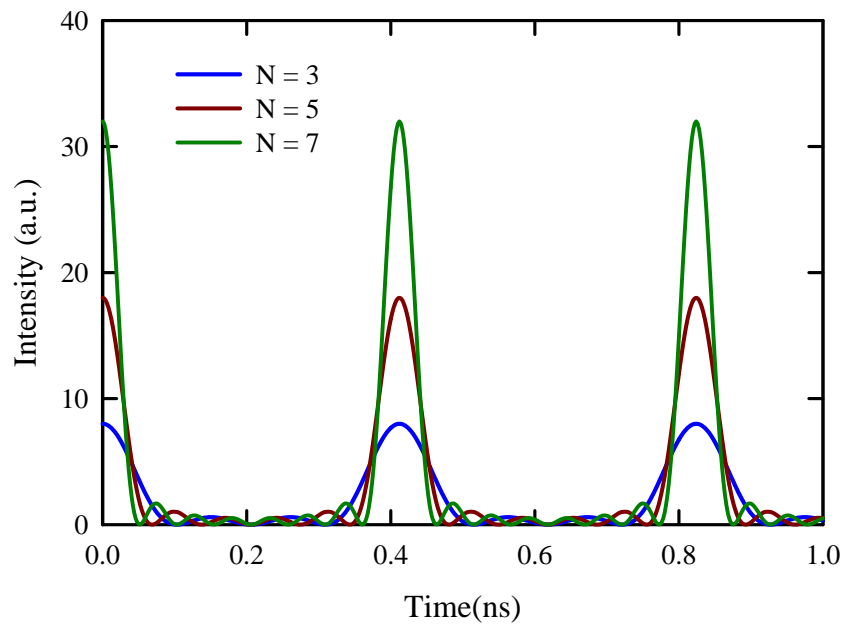


Fig. 1.1-3. The output intensity of a mode-locked laser pulse plotted as a function of time for the case of $N = 3, 5,$ and 7 modes.

From equation (1.1.5), it follows the interesting fact that the pulse width of the mode-locked laser associates with not only the number of locked modes but also the cavity round trip time.

In experimentally, Mode-locking was first observed in a maser by Gürs and Müller in 1963 [1]. The first mode-locking laser was demonstrated when Hargrove, Fork, and Pollack used an acousto-optical modulator to modulate the loss (AM mode-locking) inside the He-Ne laser cavity at a rate coincident with the cavity round trip in 1964 [2]. At the same year, Harris and Targ used frequency modulator to obtain FM mode-locking He-Ne laser [3]. In 1965, Mocker and Collins demonstrated the first passively mode-locking laser when they found that the saturable absorber dye cell could use to lock the laser [4]. In this work, they found that their Q-switched pulses were split into short pulses separate in time by cavity round-trip. For several years the techniques were developed for measurement of these pulses. But, the measurement accuracy was impaired by the somewhat unpredictable and transient in nature. Finally, seven years after the first experimental demonstration of passively mode-locking, this drawback was overcome. In 1972, Ippen, Shank, and Dienes were the first to demonstrate a passively mode-locked laser with a stable continuous pulse trains [5]. Shortly thereafter, this led to production of pulses of sub-picosecond [6]. The work on dye lasers continued unabated for the next decade producing shorter and shorter pulses. Finally, the 6-fs pulse was obtained by Fork et al. using external cavity pulse compression [7]. In 1991, Spence, and Kean, and Sibbett produced 60 femtosecond pulses by using a Titanium:sapphire ($\text{Ti:Al}_2\text{O}_3$) crystal both as gain medium and a mode locking element [8]. This technique, which provides an

extremely simple means for ultrashort pulse generation in lasers, has been termed Kerr lens mode locking (KLM). In Kerr lens mode-locking, strong self-focusing of the laser beam combined with either a hard aperture or a “soft” gain aperture is used to produce a self amplitude modulation that is the same as fast saturable absorber. In this type of laser, the modes locked partially or totally without any need for an external modulation (actively mode-locking) or a saturable absorber material. Therefore, it is also called self-mode-locked laser. The KLM mode-locking mechanism is an effective way to generating short powerful pulses. Despite the great success of KLM, there are some significant drawbacks for practical application of these ultrafast lasers. It requires a starting mechanism and a critical cavity alignment. Recently, most commercial passive cw mode-locking lasers incorporate an intracavity semiconductor saturable absorber mirror (SESAM) to start and sustain mode-locking [9-11].

In this thesis, the picosecond self-mode-locked lasers are investigated completely. The average output power is up to 5 W with repetition rates in the range of 1.0–6.0 GHz. Besides the fundamental mode-locking operation, the self-mode-locked lasers with high-order transverse intensity distribution are also demonstrated.

1.2 Transverse Modes of Laser Cavity

In laser cavity, there are two types of resonant modes. First type, the “longitudinal” modes differ from one another only in their oscillation frequency; second type, the “transverse” modes differ from one another not only in their oscillation frequency, but also in their field distribution in a plane perpendicular to the direction of propagation. The transverse mode structures of a wave inside the cavity are described for the Cartesian coordinates by the symbol TEM_{mn} . The integers m and n represent the order of transverse modes. For a given (m, n) , it also represents the number of nodes in vertical and horizontal direction to the beam axis. In Cylindrical coordinates, the symbols TEM_{mn} are used described, where the integers p and l are radial and azimuthal nodes. Thus, the TEM_{mn} is the lowest order transverse mode which has a Gaussian intensity distribution on the beam axis in laser cavity. For higher order modes, the Hermite polynomials (H) and Laguerre polynomials (L) are employed in Cartesian coordinate and Cylindrical coordinates respectively. Therefore, the TEM_{mn} are also called Hermite-Gaussian modes (HG_{mn}), the TEM_{pl} are called Laguerre-Gaussian modes (LG_{pl}). Figure 1.2-1 demonstrates the various HG_{mn} mode patterns as they would appear in the output beam of a laser. The LG_{pl} mode patterns also shows in Fig. 1.2-2. The wave functions will be described in Sec. 5.1. However, the laser beams with LG modes are also called optical vortex beams that possess orbital angular momentum because of a phase singularity.

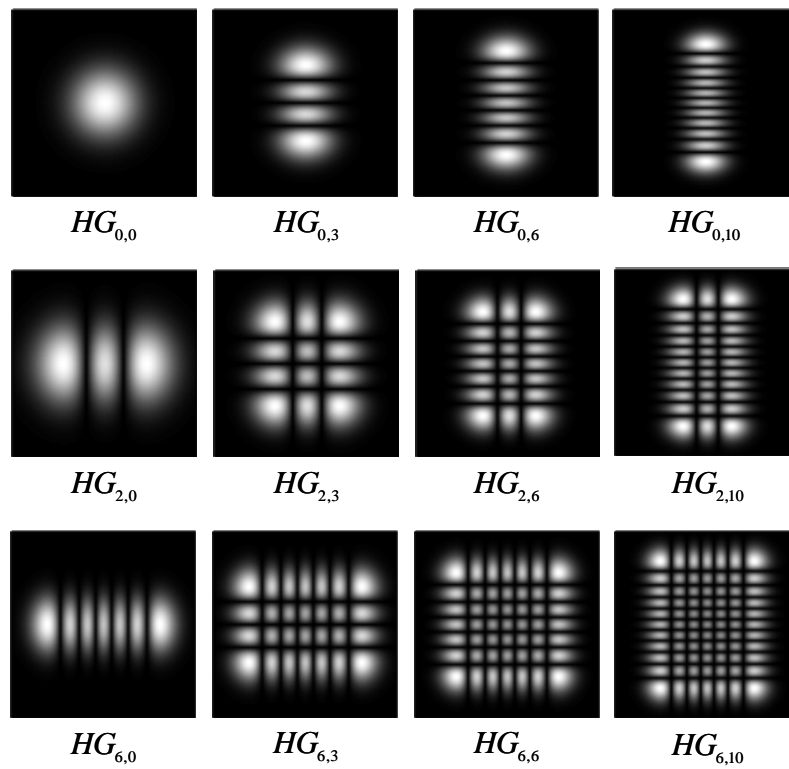


Fig. 1.2-1. The transverse mode patterns of Hermite-Gaussian modes with different orders.

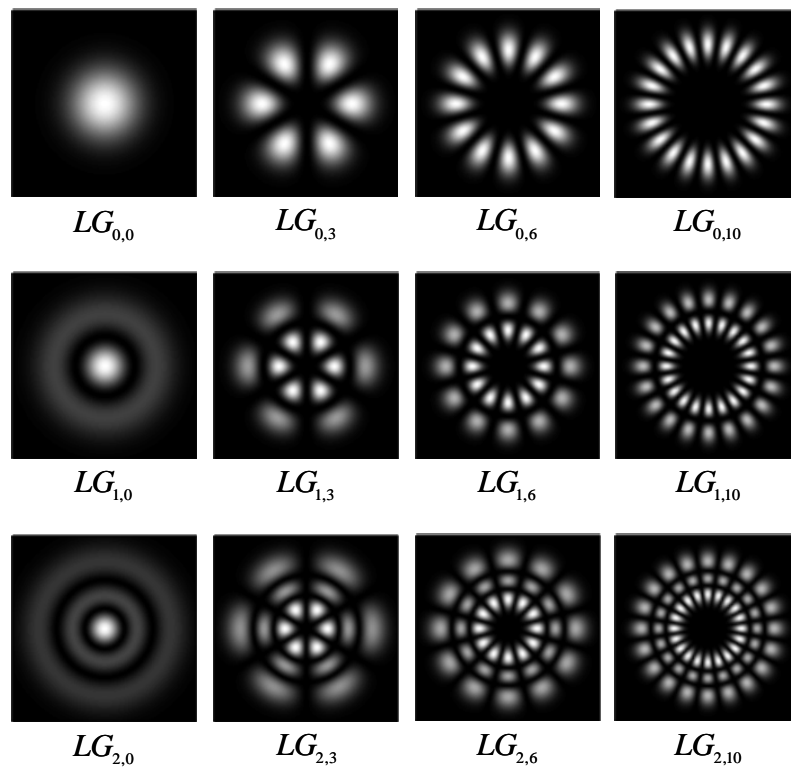


Fig. 1.2-2. The transverse mode patterns of Laguerre-Gaussian modes with different orders.

For example, the intensity distribution, phase diagram, and the vector field of the LG_{01} mode have been demonstrated in Fig. 1.2-3. It can be seen that at the center of the color wheel of phase diagram is a singularity which giving rise to a vortex.

In the frequency domain, the resonance frequencies of resonant modes in the cavity can express as

$$f = \frac{c}{2L} \left[q + (1 + m + n) \frac{\cos^{-1} \pm \sqrt{g_1 g_2}}{\pi} \right] \quad (1.2.1)$$

where g_i is the resonator g parameter ($g_i = 1 - L/R_i$), R_i is the radii of curvature for both mirrors, and L is the cavity length. From equation (1.2.1), it can see that the separation between each longitudinal mode is $\Delta f_L = c/2L$, only a function of cavity length; the separation between transverse modes is

$$\Delta f_T = \frac{c}{2L} \frac{\cos^{-1} \sqrt{g_1 g_2}}{\pi}, \quad (1.2.2)$$

not only a function of cavity length but also dependent on the curvature of the mirrors. It can be found that corresponding to a given transverse mode are a number of longitudinal modes which have the same field distribution as the given transverse mode but which differ in frequency.

In experimentally, Laabs and Ozygus demonstrated a method for the excitation of HG modes in end-pumped solid-state lasers by off-axis pumping in 1996 [12]. At the next year, a general model has been developed for the generation of HG modes in

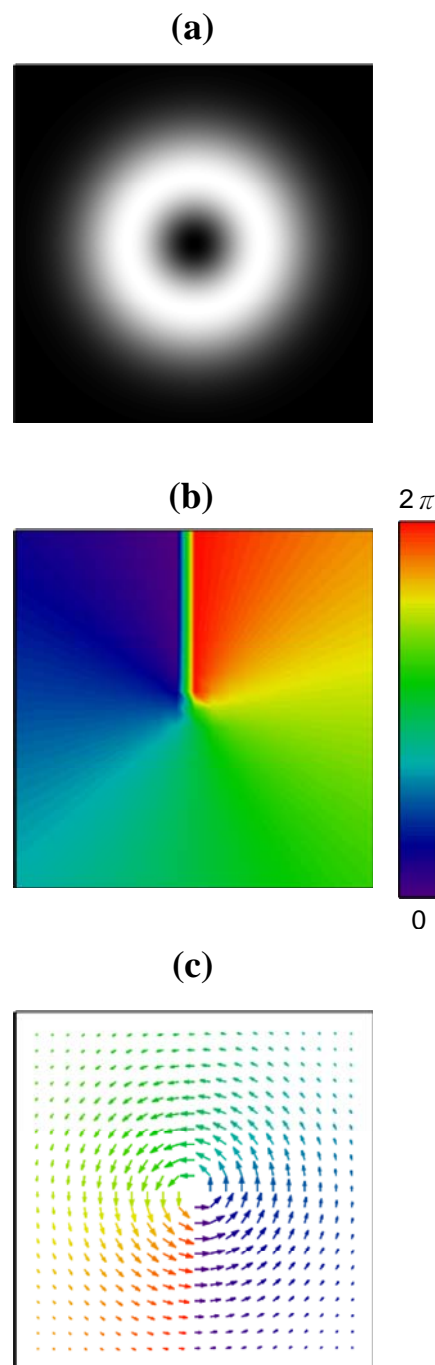


Fig. 1.2-3. The vortex beam of LG_{01} . (a) The intensity distribution. (b) The phase diagram. (c) The vector field structure.

fiber-coupled laser-diode end-pumped laser by Chen et al. [13,14]. They predict how the oscillation of HG modes is affected by the pump position, the pump size, and cavity mode size. For LG mode, it has been reported in electrically pumped [15,16] and optically pumped [17] vertical-cavity surface-emitting semiconductor lasers (VCSELs). Recently, a technique for the generation of LG modes with $p=0$ and specified value of l in a fiber-coupled diode end-pumped solid-state laser was reported [18]. The key point is to produce a doughnut-shaped pump profile by defocusing a standard fiber-coupled diode. In the paper, they also developed a theoretical model to predict the affection of pump position, pump size, and mode size. Besides the HG and LG modes, there is another complete basis, Ince-Gaussian (IG) modes, which may be consider continues transition modes between HG and LG modes. Recently, the IG modes were demonstrated theoretically and experimentally [19-21].

In this work, the efficient self-mode-locked HG lasers are investigated. The stable self-mode-locked laser for the $TEM_{0,0}$ mode was obtained firstly. Subsequently the high-order HG $TEM_{0,m}$ mode-locked laser can be generated with off-axis pumping which mentioned above. The larger the off-axis displacement is, the higher order of the HG $TEM_{0,m}$ modes are generated. With varying the off-axis displacement, the laser output can be found to display a stable mode-locking operation for single pure $TEM_{0,m}$ modes with $m=0$ to $m=9$. Besides the stable mode-locking operation with single HG mode, the modulation mode-locking with two HG modes coupling is also observed.

1.3 Beam Transformation

As mentioned above, HG modes and LG modes are the transverse intensity distribution of the spherical laser resonators. Rectangular geometry leads to Hermite-Gaussian modes. On the other hand, when cylinder coordinates are more appropriate for Laguerre-Gaussian modes. However, most lasers, in spite of having nearly cylindrical symmetry, still generate the HG modes. The reason is that pure, higher order LG modes are hard to generate because of more constraints. Although the LG modes are generated in fiber-coupled diode-pumped solid-state lasers by the technique that produce a doughnut-like pump profile [18]. The relations between HG modes and LG modes still need to derive because the recent work of translation from HG modes to LG modes was required. Since, both types of these modes form orthogonal and complete basis that one would be expressed the combination of the other. In 1993, Kimel and Elias established the relation between HG and LG modes [22]. With these, a LG mode is expressed as a sum of HG modes, and vice versa. The LG modes can be decomposed into HG modes as

$$\Phi_{n,m}^{(LG)}(x, y, z) = \sum_{u=0}^{2\tilde{n}+\tilde{m}} e^{iu\frac{\pi}{2}} \cdot B(\tilde{n}, \tilde{m}, u) \cdot \Phi_{2\tilde{n}+\tilde{m}-u,u}^{(HG)}(x, y, z) \quad (1.3.1)$$

where

$$B(\tilde{n}, \tilde{m}, u) = \frac{(-1)^u}{\sqrt{2^{2\tilde{n}+\tilde{m}}}} \sum_{\nu} \frac{(-1)^{\nu} \sqrt{(\tilde{n} + \tilde{m})!(2\tilde{n} + \tilde{m} - u)!} u!}{\nu!(u - \nu)!(\tilde{n} + \tilde{m} - \nu)!(\tilde{n} + \nu - u)!} \quad (1.3.2)$$

The relation of the indices between the HG modes and LG modes follows $n = \tilde{n}$ and $m = \tilde{n} + \tilde{m}$. Figure 1.3-1 demonstrates a numerical result of the LG mode described in Eq. (1.3.1) with $(\tilde{n}, \tilde{m}) = (0, 5)$. It can be seen that the LG mode was comprised several degenerated HG modes with different order.

In generally, the techniques using in experiment by externally converting the Hermite-Gaussian modes to Laguerre-Gaussian modes are called beam transformation. To data, several devices, including spiral phase plate [23,24], computer-generated holographic converters [25,26], and astigmatic mode converters (AMC) [27], have been successfully demonstrated to transform Hermite-Gaussian modes into Laguerre-Gaussian. A spiral phase plate in general is a transparent plate which its thickness increasing proportional to the azimuthal angle around a point in the center of the plate, as shown in Fig. 1.3-2(a). The surface looks like one turn of a staircase. When a beam is passed through the plate, the helical surface can give a helical character to the beam. Computer-generated hologram, as shown in Fig. 1.3-2(b), is another converter to influence the phase and amplitude distribution of a field. Dependent on the type of hologram, a large or small fraction of the incident beam is diffracted in to a helical wavefront beam. This technique not only can generate the circularly symmetric doughnut modes (LG modes), but also can be extended to produce patterns of more complexity. Both of them, spiral phase plate and computer-generated holographic converters, introduce an azimuthal phase dependence to a fundamental HG mode

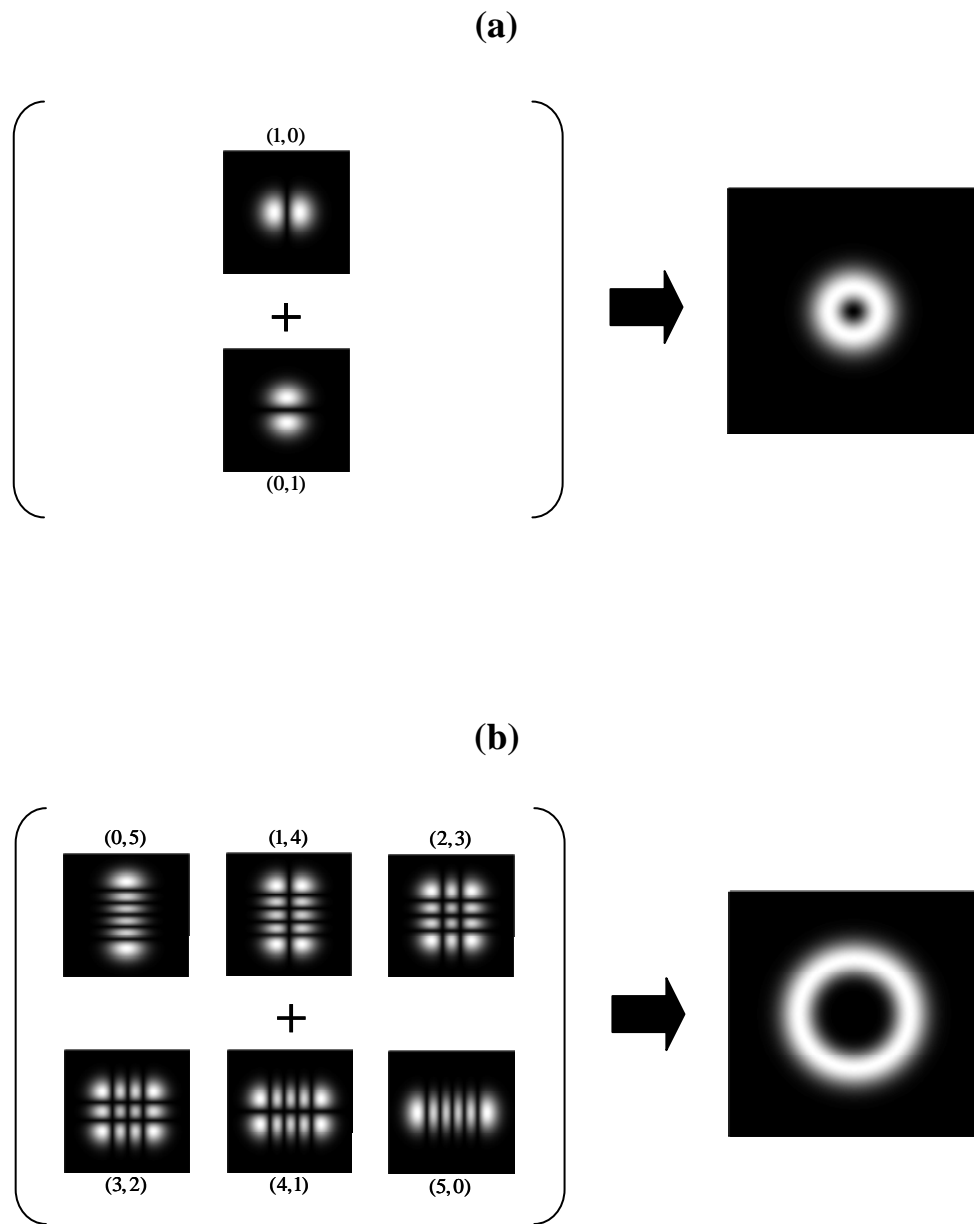
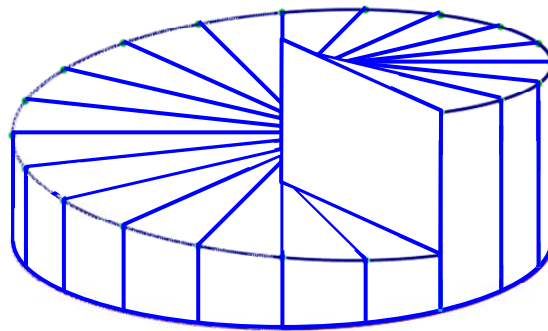


Fig. 1.3-1. Numerical result according to Eq. (1.3.1). (a) Numerical result of $LG_{0,1}$. (b) Numerical result of $LG_{0,5}$.

(a)



(b)



Fig. 1.3-2. Conventional mode converter. (a) The spiral phase plate. (b) The sketch of computer-generated hologram.

beam. Because of a screw-phase dislocation in the centre of the beam, the intensity patterns display destructive interference leading to the characteristic annular intensity distribution. However, the astigmatic mode converter is based on cylindrical lenses and converts HG modes of all order to correspond LG modes. The cylindrical lens mode converter is constructed by two identical cylindrical lenses are separated by $\sqrt{2}f$, where f is the focal length of lenses. In generally, the input HG modes are aligned at 45° to the principal axis of the lens and then produce the corresponding LG modes. This method, in principle, generates pure LG modes unlike the spiral phase plate and computer-generated holographic converter. Figure 1.3-3 demonstrates the illustration of transformation between HG modes and LG modes by use of cylindrical lenses. The left column represents the simulated High-order HG modes with transverse indices $(n, m) = (5, 0)$, $(5, 1)$, and $(2, 5)$. The right column represents the correspond simulated high-order LG modes transformed by cylindrical lenses with transverse indices $(n, m) = (0, 5)$, $(1, 4)$, and $(2, 3)$.

In this thesis, the picosecond optical vortex pulses are demonstrated by externally mode converting. With a simple cylindrical lens, the picosecond vortex pulses have been generated by converting the self-mode-locked high-order Hermite-Gaussian modes lasers for the $TEM_{0,m}$ modes from $m = 0$ to $m = 9$ into Laguerre-Gaussian modes. The mode-locked pulse width is in the range of 20 – 25 ps at the repetition rate 3.5GHz. The picosecond optical vortex pulses can be potential beneficial to a number of applications such as high-quality material processing [28], controllable specificity of chiral matter [29], and nonlinear frequency conversion [30].

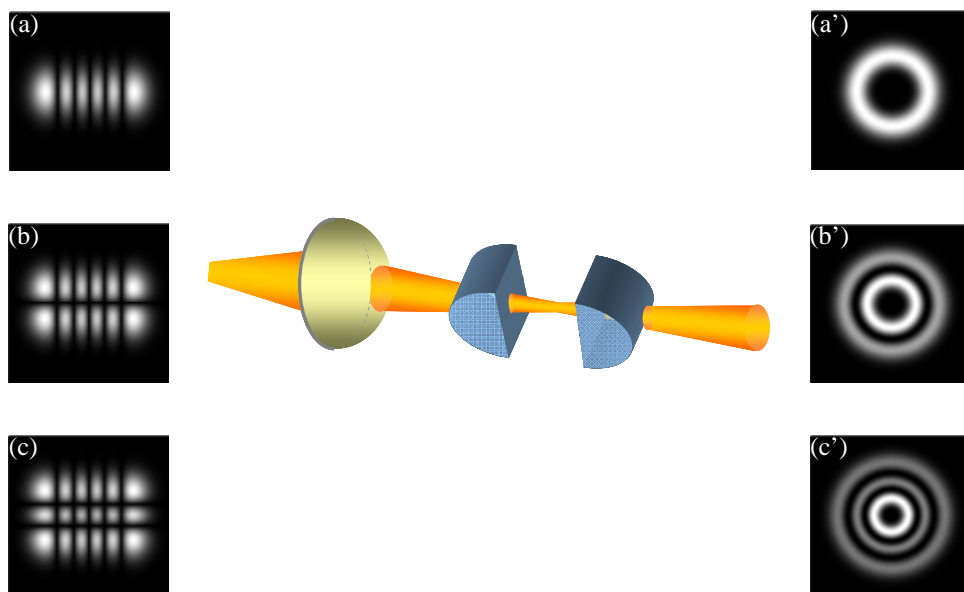


Fig. 1.3-3. Diagram of Hermite-Gaussian modes convert into Laguerre-Gaussian mode by use of cylindrical lenses. (a)-(c) Numerical results of Hermite-Gaussian modes before transformation. (a')-(c') Numerical results of Laguerre-Gaussian modes after transformation.

1.4 Overview of Thesis

The main text of this dissertation is structured as follow:

In chapter2, compact efficient high power diode-end-pumped self-mode-locked lasers are investigated. In Sec. 2.1 the phenomena of spontaneous mode-locking (SML) are discussed. It may be the concept that the mode-locked laser can be generated without the need for any additional components. In Sec. 2.2 the experimental results of high-power multi-gigahertz self-mode-locked Nd:YVO₄ and Nd:GdVO₄ lasers at 1064 nm are reported. Besides the self-mode-locked lasers operate at the wavelength 1064 nm, the 1342 nm mode-locked Nd:YVO₄ laser are also demonstrated in Sec. 2.3.

In chapter 3, the technique of mode control for self-mode-locked lasers is presented. The first section of this chapter introduces the influence of the number of longitudinal lasing modes on the self-mode-locked lasers. By controlling the amount of spatial hole burning, the pulse width in the mode-locked lasers can be adjusted and the stability can be improved. The experimental results will be discussed in Sec. 3.3, Finally, the theoretical model for estimating the maximum longitudinal lasing modes in self-mode-locked Nd:YVO₄ laser is established. The theoretical results are shown to be in good agreement with experimental observations.

In chapter4, we investigate theoretical and experimental the self-mode-locked laser with transverse intensity distribution high order transverse modes. In Sec. 4.1,

the paraxial approximation Maxwell's equations are used to find the wave functions of the spherical laser cavity. The solutions are the Hermite-Gaussian and Laguerre-Gaussian beams that well-known wave function of spherical laser cavity in rectangular and in cylindrical coordinate respectively. In Sec. 4.2, firstly, the theoretical analysis for mode-locked with high-order Hermite– Gaussian (HG) modes are reported. In experimentally, we also observed a stable self-mode-locked Nd:GdVO₄ laser with high-order HG modes. The experimental results are in good agreement with theoretical calculations. In the Sec. 4.3, we used the external mode converter to generate the optical vortex pulses which convert from self-mode-locked laser Hermite-Gaussian beams.

In previous chapters, we reported a number of investigations of self-mode-locked laser. Since there is increasing in self-mode-locked lasers for many applications. In chapter 5, we will give some application of the self-mode-locked. Firstly, we have reported the determination of the thermal lens in diode-pumped mode-locked laser. The method used here is to measure the transverse beat frequencies of mode-locked laser with two transverse mode coupling. When two transverse modes are coupling in mode-locked laser, a stable output pulses train will be modulation with the beat frequencies dependent on the pumped power. From these beat frequencies, the thermal lens coefficient can be calculated. In Sec. 5.2, we present novel method to find the refractive indices of Nd:YVO₄ crystals with different dopant concentrations. Because of the frequencies shift is as function of optical path length which is the product of refractive index and crystal length. To measure the frequencies shift, then the refractive indices of sample crystals will be obtained.

References

- [1] K. Gürs and R. Müller, “Breitband-modulation durch Steuerung der emission eines optischen masers,” *Phys. Lett.* 5, 179 (1963)
- [2] L. E. Hargrove, R. L. Fork, and M. A. Pollack, “Locking of He-Ne laser modes induced by synchronous intracavity modulation,” *Appl. Phys. Lett.* 5, 4 (1964).
- [3] S. E. Harris and R. Targ, “FM oscillation of the He-Ne laser,” *Appl. Phys. Lett.* 5, 202 (1964).
- [4] H. W. mocker, R. J. Collins, “Mode competition and self-locking effects in a Q-switched ruby laser,” *Appl. Phys. Lett.* 7, 270 (1965).
- [5] E. P. Ippen, C. V. Shank, and A. Dienes, “Passive mode locking of the cw dye laser,” *Appl. Phys. Lett.* 21, 348 (1972).
- [6] C. V. Shank and E. P. Ippen, “sub-picosecond kilowatt pulses from a mode-locked cw dye laser,” *Appl. Phys. Lett.* 24, 373 (1974).
- [7] R. L. Fork, C. H. B. Cruz, P. C. Becker, and C. V. Shank, “Compression of optical pulses to six femtoseconds by using cubic phase compensation ,” *Opt. Lett.* 12, 483 (1987).
- [8] D. E. Spence, P. N. Kean, and W. Sibbett, “60-fsec pulse generation from a self-mode-locked Ti:sapphire laser,” *Opt. Lett.* 16, 42 (1991).
- [9] U. C. Keller, D. A. B. Miller, G. D. Boyd, T. H. Chiu, J. F. Ferguson, M. T. Asom,

References

- “Solid-state low-loss intracavity saturable absorber for Nd:YLF lasers : an antiresonant semiconductor Fabry-Perot saturable absorber,” *Opt. Lett.* 17, 505 (1992).
- [10] U. Keller, K. J. Weingarten, F. X. Kärtner, D. Kopf, B. Braun, I. D. Jung, R. Fluck, C. Hönninger, N. Matuschek, and J. Aus der Au, “Semiconductor saturable absorber mirrors (SESAM’s) for femtosecond to nanosecond pulse generation in solid-state lasers,” *IEEE J. Sel. Top. Quantum Electron* 2, 435 (1996).
- [11] I. D. Jung, F. X. Kärtner, N. Matuschek, D. H. Sutter, F. Morier- Genoud, Z. Shi, V. Scheuer, M. Tilsch, T. Tschudi, and U. Keller, “Semiconductor saturable absorber mirrors supporting sub-10-fs pulses,” *Appl. Phys. B* 65, 137 (1997).
- [12] H. Laabs and B. Ozygus, “Excitation of Hermite Gaussian modes in end-pumped solid-state lasers via off-axis pumping,” *Opt. Laser Technol.* 28, 213 (1996).
- [13] Y. F. Chen, T. M. Huang, K. H. Lin, C. F. Kao, C. L. Wang, and S. C. Wang, “Analysis of the effect of pump position in transverse modes in fiber-coupled laser-diode end pumped lasers,” *Opt. Commun.* 133, 517 (1997).
- [14] Y. F. Chen, T. M. Huang, C. F. Kao, C. L. Wang, and S. C. Wang, “Generation of Hermite-Gaussian modes in fiber-coupled laser-diode end-pumped laser,” *IEEE J. Quantum Electron.* 33, 1025 (1997).
- [15] C. Degen, I. Fischer, and W. Elsässer, “Transverse modes in oxide confined VCSELs: Influence of pump profile, spatial hole burning, and thermal effects,” *Opt. Express* 5, 38 (1999).

References

- [16] Q. Deng, H. Deng, and D. G. Deppe, "Radiation fields from whispering-gallery modes of oxide-confined vertical-cavity surface-emitting lasers," *Opt. Lett.* 22, 463 (1997).
- [17] S. F. Pereira, M. B. Willemsen, M. P. van Exter, and J. P. Woerdman, "Pinning of daisy modes in optically pumped vertical-cavity surface-emitting lasers," *Appl. Phys. Lett.* 73, 2239 (1998).
- [18] Y. F. Chen, Y. P. Lan, and S. C. Wang, "Generation of Laguerre-Gaussian modes in fiber-coupled laser diode end-pumped laser," *Appl. Phys. B* 72, 167 (2001).
- [19] M. A. Bandres and J. C. Gutiérrez-Vega, "Ince-Gaussian beams," *Opt. Lett.* 29, 144 (2004).
- [20] M. A. Bandres and J. C. Gutiérrez-Vega, "Ince-Gaussian modes of the paraxial wave equation and stable resonators," *J. Opt. Soc. Am. A* 21, 873 (2004).
- [21] U. T. Schwarz, M. A. Bandres, and J. C. Gutiérrez-Vega, "Observation of Ince-Gaussian modes in stable resonators," *Opt. Lett.* 29, 1870 (2007).
- [22] I. Kimel and L. R. Elias, "Relations between Hermite and Laguerre Gaussian modes," *IEEE J. Quantum Electron.* 29, 2662 (1993).
- [23] M. W. Beijersbergen, R. P. C. Coerwinkel, M. Kristensen, and J. P. Woerdman, "Helical-wavefront laser beams produced with a spiral phase plate," *Opt. Commun.* 112, 321 (1994).
- [24] G. A. Turnbull, D. A. Robertson, G. M. Smith, L. Allen, and M. J. Padgett, "The generation of free-space Laguerre-Gaussian modes at millimeter-wave frequencies by use of a spiral phase plate," *Opt. Commun.* 127, 183 (1996).
- [25] N. R. Heckenberg, R. McDuff, C. P. Smith, H. Rubinsztein-Dunlop, and M. J.


References

- Wegener, “Laser beams with phase singularities,” *Opt. Quantum Electron.* 24, S591 (1992).
- [26] N. R. Heckenberg, R. McDuff, C. P. Smith, and A. G. White, “ Generation of optical phase singularities by computer-generated holograms ,” *Opt. Lett.* 17, 221 (1992).
- [27] M. W. beijsbergen, L. Allen, H. E. L. O. van der Veen, and J. P. Woerdman, “Astigmatic laser mode converters and transfer of orbital angular momentum,” *Opt. Commun.* 96, 123 (1993).
- [28] J. Hamazaki, R. Morita, K. Chujo, Y. Kobayashi, S. Tanda, and T. Omatsu, “optical-vortex laser ablation,” *Opt. Express* 18, 2144 (2010).
- [29] D. L. Andrews, L. C. Dávila, and M. Babiker, “On optical vortex interaction with chiral matter,” *Opt. Commun* 237, 133 (2004).
- [30] K. Dholakia, N. B. Simpson, and M. J. Padgett, “Second-harmonic generation and the orbital angular momentum of light,” *Phys. Rev. A* 54, R3742 (1996).

Chapter 2

Continue-Wave

Self-Mode-Locked Lasers

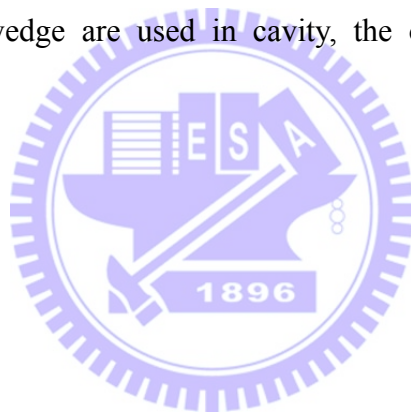


2.1 Phenomenon of Spontaneous Mode Locking

The appearance of spontaneous mode locking (SML) in laser cavity without using additional nonlinearity except gain medium is an intriguing phenomenon of laser emission. During the early research on mode locking, the SML phenomenon was observed on different types of lasers including He-Ne [1], ruby [2], Nd:glass [3], and argon ion [4] laser systems. In the mid-1960s, the SML was not considered to be a reliable approach for the generation of ultrashort pulses, partly because the mechanism for SML was not adequately understood. Recently, SML pulses have been obtained in the experiment of Q-switched ytterbium-doped fiber laser [5] and Er-Yb fiber laser [6]. Unless the SML in pulse lasers, a fairly stable continuous-wave SML pulses have been demonstrated by P. Glas et al. in Nd-doped double clad fiber laser [7]. They found self pulsations not only for cw-pumped Nd^{3+} -doped fiber laser with different host materials for example silicate glass, phosphate glass, silica glass but also Nd^{3+} -doped YAG and YAP lasers, Nd^{3+} -doped glass rod laser, and Cr:LISAF lasers using standard power supplies. Consequently, the SML typically occurs in a multimode laser without employing an extra nonlinearity except the gain medium. Nevertheless, the SML phenomenon is not very reliable and usually occurs in pulse lasers. Therefore, it needs further understanding for achieving a reliable SML pulses.

Before SML can be accomplished in lasers, all adjacent longitudinal modes need to have the same frequency separation. However, the dispersion associated with the

laser transition generally causes the slightly different frequency separations of longitudinal modes. Theoretical studies on the SML mechanism have confirmed that the combination tones of the third order nonlinear polarization terms can help in compensating the dispersion-induced phase shift [7-9]. Therefore, the laser gain medium have a large third-order nonlinearity are possible to be the promising host crystals for stable SML. Although a large nonlinearity is favorable for SML, it is worth noting that the wedge shape of the laser gain medium and output coupler are also important for obtaining a complete stable SML. When a laser gain medium and output coupler without wedge are used in cavity, the output pulse trains exhibit incomplete SML.



2.2 High Power Self-Mode-Locked Multi-GHz Nd:YVO₄ and Nd:GdVO₄ Lasers

In the past decade, neodymium-doped yttrium vanadate (Nd:YVO₄) and gadolinium vanadate (Nd:GdVO₄) have been the excellent laser gain mediums for the diode-pumped solid-state lasers. Recent studies manifest that GdVO₄ and YVO₄ crystals have attractive $\chi^{(3)}$ nonlinear properties [10]. Base on the result, diode-pumped self-stimulated Raman lasers with Nd:YVO₄ and Nd:GdVO₄ crystals have been successfully developed [11-16].

The magnitude of the third-order nonlinearity is not only related to the strength of stimulated Raman scattering but also related to the potential of spontaneous mode locking (SML). The SML is referred to as the self-mode-locking because no passive or active element is needed to be introduced in the cavity. Experimental measurement indicates that the nonlinear refractive index of YVO₄ crystals (1.9×10^{-15} cm²/W) [17,18] is approximately six times greater than that of sapphire crystal (3.1×10^{-16} cm²/W) [19]. As a consequence, the YVO₄ crystal is possible to be a promising host crystal for SML operation. Since Nd:GdVO₄ crystals have similar laser properties with Nd:YVO₄ crystals, it is also highly feasible to fulfill SML in a Nd:GdVO₄ laser.

In this section, we experimentally demonstrate that a CW self-mode locking with multi-gigahertz (GHz) oscillations can be straightforwardly achieved in a Nd:YVO₄

and Nd:GdVO₄ laser with a simple linear cavity without the need of any additional components.

2.2.1 Experimental Setup

A schematic of the laser experiment is shown in Figure 2.2-1. The cavity configuration is a simple concave-plano resonator. The active medium are a-cut 0.2 at.% Nd:YVO₄ crystal and 0.25 at.% Nd:GdVO₄ crystal with length of 10 mm. Both end surfaces of the crystals were antireflection coated at 1064 nm and wedged 2° to suppress the Fabry-Perot etalon effect. The laser crystal was wrapped with indium foil and mounted in a water-cooled copper holder. The water temperature was maintained around 20 °C to ensure stable laser output. The laser crystal was placed very near (2–3 mm) the input mirror, which was a 10-cm radius-of-curvature concave mirror with antireflection coating at 808 nm on the entrance face and with high-reflectance coating at 1064 nm (>99.8%) and high transmittance coating at 808 nm on the second surface. A flat wedged output coupler with 15% transmission at 1064 nm was used throughout the experiment. The pump source was a 3-W 808-nm fiber-coupled laser diode with a core diameter of 100 μm and a numerical aperture of 0.16. Focusing lens with 5 mm focal length and 85% coupling efficiency was used to re-image the pump beam into the laser crystal. The average pump size was approximately 70 μm. The optical cavity length was varied between 2.5 cm and 7.5 cm, the corresponding free spectral range (FSR) varying from 6.0 GHz to 2.0 GHz. The mode-locked pulses were detected by a high-speed InGaAs photodetector (Electro-optics Technology Inc. ET-3500 with rise time 35 ps), whose output signal was connected to a digital

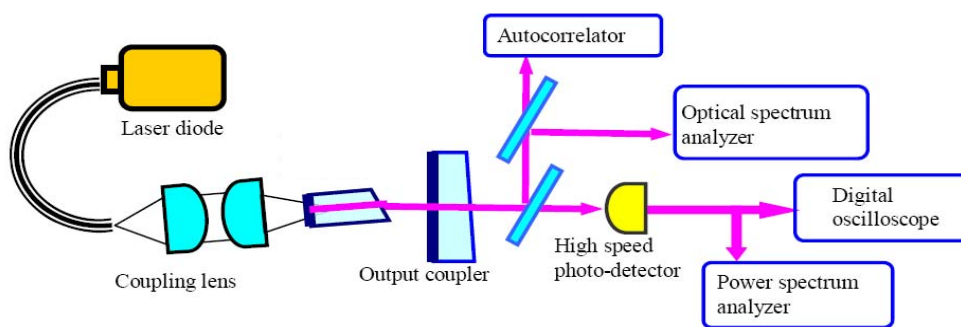


Fig. 2.2-1 Experimental setup for a diode-pumped self-mode-locked laser.

oscilloscope (Agilent DSO 80000) with 10 GHz electrical bandwidth and a sampling interval of 25 ps. The output signal of the photodetector was also analyzed by an RF spectrum analyzer (Advantest, R3265A) with a bandwidth of 8.0 GHz. The spectral information of the laser was monitored by a Fourier optical spectrum analyzer (Advantest, Q8347) that is constructed with a Michelson interferometer with resolution of 0.003 nm.

2.2.2 Experimental Results and Discussions

Because the third-order nonlinearity and optical properties of Nd:YVO₄ and Nd:GdVO₄ crystals are similar, the difference between Nd:YVO₄ and Nd:GdVO₄ crystals for the self-mode-locked operation was found to be negligible. Therefore, we just report the experimental results of Nd:YVO₄ laser. The optical cavity length was firstly set to be approximately 6.4 cm, corresponding to the FSR of 2.35 GHz. When the cavity alignment was optimized for generating the maximum average output power, the time trace of the output radiation revealed the laser to be in the spontaneous mode-locked state. Figures 2.2-2(a) and 2.2-2(b) show the pulse trains on two different timescales, one with time span of 5 μs, demonstrating the amplitude oscillation, the other with time span of 10 ns, demonstrating the mode-locked pulses. The corresponding power spectrum is shown in Fig. 2.2-2(c). Although some amplitude fluctuation exists under the circumstance of the optimum output power, it can be definitely improved with the fine-tuning of the cavity alignment by monitoring the temporal behavior of the pulse train profile and the width of the power spectrum. Figures 2.2-3(a)-(c) show the real-time traces and the power spectrum for the case of

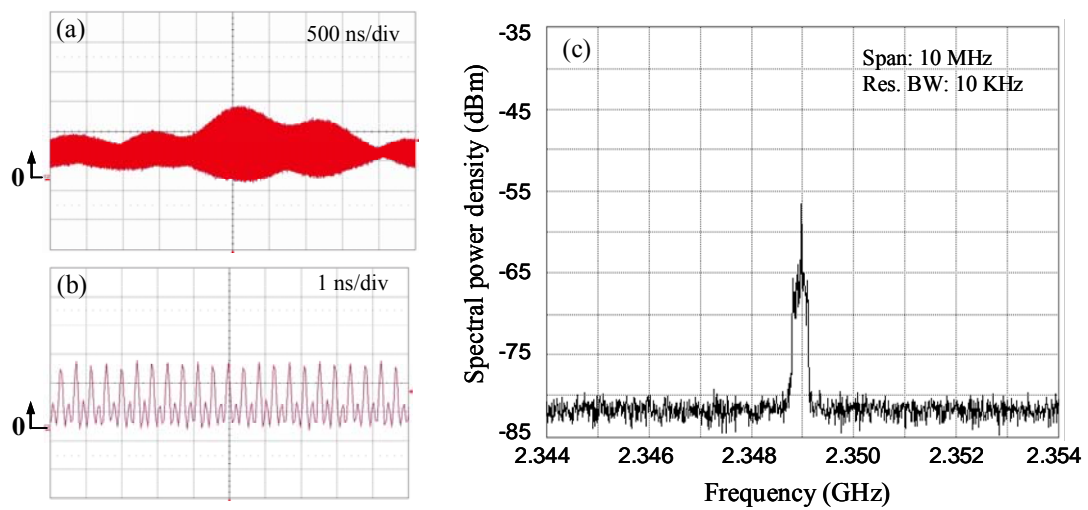


Fig. 2.2-2 Pulse trains on two different timescales. (a) Time span of 5 μ s, demonstrating the amplitude oscillation. (b) Time span of 10 ns, demonstrating mode-locked pulses. (c) Power spectrum.

minimizing amplitude fluctuation. As shown in Figs. 2.2-3(a) and 2.2-3(b), the full modulation of pulse trains without any CW background indicates the realization of complete mode locking. Excellent performance on self-mode locking indicates that the YVO_4 crystal is a promising host medium for efficient SML operation at GHz oscillations. Experimental results reveal that the relative frequency deviation of the power spectrum, $\Delta\nu/\nu$, is smaller than 5×10^{-5} over day-long operation, where ν is the center frequency of the power spectrum and $\Delta\nu$ is the frequency deviation of full width at half maximum. It is worthwhile to mention that the wedge shape of the laser crystal is vital for obtaining a complete stable mode-locked operation. When a laser crystal without a wedge is used in the flat-flat cavity, the pulse trains exhibit incomplete mode locking with CW background to a certain extent. On the other hand, when an oscilloscope with bandwidth less than 500 MHz is used to measure the present temporal characteristics, the result will display like a pure CW laser. Perhaps this is the reason why the phenomenon of self-mode locking in the range of GHz has not been discovered earlier.

Experimental results reveal that the average output power of the stable continuous-wave mode-locking is approximately 90% of the maximum average output power. Figure 2.2-4(a) shows the average output powers versus the incident pump power obtained at a mode-locked frequency of 5.32 GHz with the cavity alignments for maximum output and stable cw mode-locking, respectively. The slope efficiency for the stable mode-locked operation can be seen to be approximately up to 40% with respect to the incident pump power, corresponding to an optical-optical efficiency of 32%. As shown in Fig. 2.2-4(b), the FWHM width of the optical

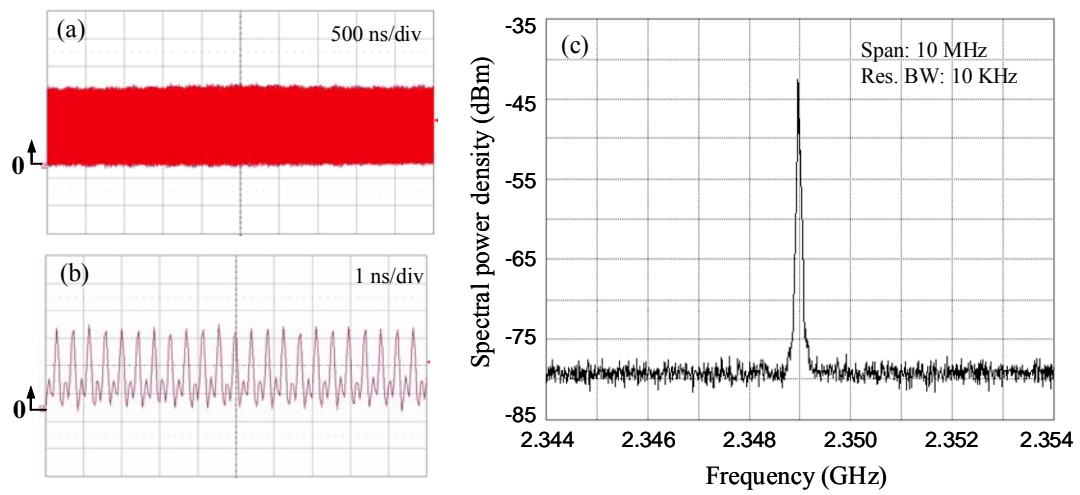


Fig. 2.2-3 Same as Fig. 2.2-2 for the stable CW mode-locked operation.

spectrum is approximately 0.21 nm around the central wavelength of 1064.3 nm. Figure 2.2-4(c) depicts the real-time traces with time span of 1 ns to measure the temporal duration of the mode-locked pulses. The pulse width can be clearly found to be approximately 50 ps (FWHM) from the real-time trace for the mode-locked frequency in the range of 2–6 GHz. However, the pulse duration was measured with a homemade autocorrelator and was found to be as short as 7.8 ps assuming a Gaussian-shaped temporal intensity profile, as shown in Fig. 2.2-4(d). The discrepancy comes from the condition that the impulse response of the present detector has a FWHM of 40 ps and the sampling interval of the present digital oscilloscope is 25 ps. Nevertheless, the real-time trace for the temporal behavior of the GHz mode-locked laser is vital for many practical applications such as high-speed electro-optic sampling and telecommunications.

We performed the same experimental procedure for different cavity lengths to investigate the influence of the intracavity power intensity on the performance of the mode locking. We found that the laser system can be easily operated in a stable single-pulse mode-locked regime when the cavity length is approximately shorter than 7.5 cm (the mode-locked repetition rate >2 GHz). For the cavity length longer than 8.5 cm, a single pulse per round trip was usually observed to split into several pulses. Figure 2.2-5 shows the experimental time traces for the cavity length at 11.3 cm. It is clear that the laser system generally turns to be in a stable multiple-pulse state when the mode-locked frequency is considerably lower than 2 GHz.

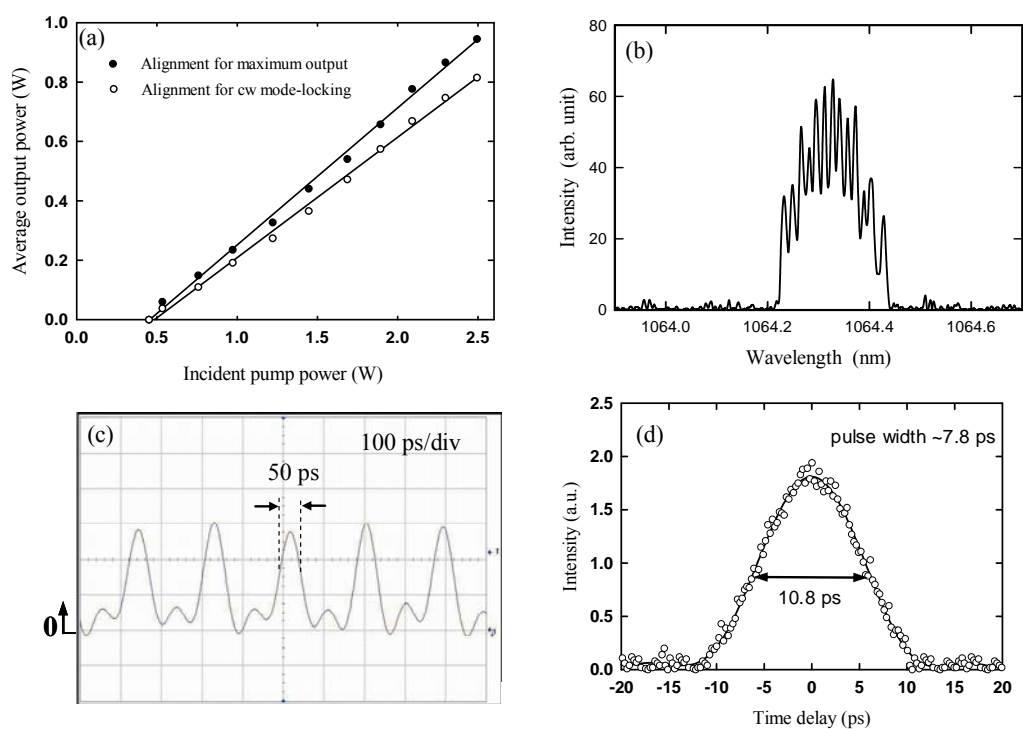


Fig. 2.2-4 (a) Average output powers versus incident pump power with the cavity alignments for maximum output and stable CW mode locking, respectively. (b) Corresponding optical spectrum of the mode locking. (c) Mode-locked pulse trains in time span of 1 ns. (d) Autocorrelation trace.

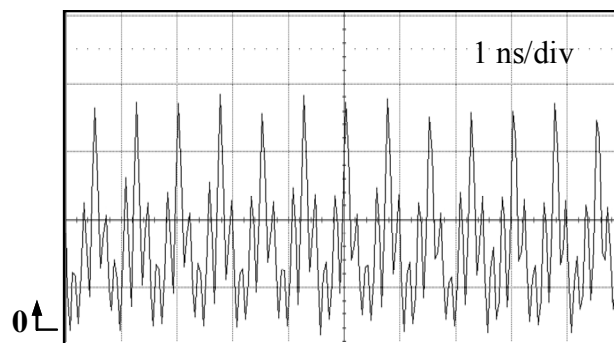


Fig. 2.2-5 Experimental time trace for the multiple-pulse mode-locked operation at the cavity length of 11.3 cm.

2.3 Diode-Pumped Self-Mode-Locked Laser at 1342 nm

Lasers at 1.3 μm have numerous applications such as the telecommunication, fiber sensing, range finder, and data storage etc. Progresses in diode-pumped solid-state lasers at 1.3 μm with Nd-doped crystals at continuous-wave (cw) and pulsed operations have been developed extensively in past years [20-25]. Meanwhile, cw mode-locked lasers generating pulse trains with high signal-to-noise ratio, low amplitude fluctuation, high average power, and high repetition rate were characterized as a desirable short-pulse source with good quality [26]. Although passive mode locking with GaAs-based semiconductor saturable absorbers mirrors (SESAMs) have been demonstrated successfully to generate ultra-short pulses in the wavelength of 0.8–1.1 μm , it is difficult to grow high-quality InGaAs SESAMs for 1.3 μm due to the required indium concentrations are beyond the critical strain-thickness limit leading to the larger lattice mismatch, higher insertion losses and reduced surface quality [20].

In the past, neodymium-doped yttrium vanadate (Nd:YVO₄) has been identified to be an excellent laser host material for the diode-pumped solid-state lasers. Recent studies have further proved that YVO₄ crystals have large magnitude of the third-order susceptibility [10] which thus can be exploited for efficient stimulated Raman scattering conversion [11-13]. More recently, it has also been demonstrated that the large third-order nonlinearity of Nd:YVO₄ crystals can be used to achieve an

efficient SML operation at frequency of multi-GHz [27]. This demonstration offers the promising prospect of developing a compact self-mode-locked Nd:YVO₄ laser at 1.34 μm .

2.3.1 Experimental Setup

An experimental setup is schematically shown in Fig. 2.3-1. The cavity configuration is a simple concave-plano resonator. The gain medium is a-cut 0.2 at. % Nd:YVO₄ crystal with dimensions of 3 mm \times 3 mm \times 10 mm. Both end surfaces of the Nd:YVO₄ crystal were anti-reflection coated at 1342 nm and wedged 2° to avoid the Fabry-Perot etalon effect. The laser crystal was wrapped with indium foil and mounted in a water-cooled copper holder. The water temperature was maintained at around 20 °C to ensure stable laser output. The laser crystal was initially placed very near (1-2 mm) the input mirror, which was a concave mirror with radius of curvature of 50 cm. The input mirror was anti-reflection at 808 nm on the entrance face and was high-reflection at 1342 nm (>99.8%) and high-transmission at 808 nm on the second surface. A flat wedged output coupler with 7% transmission at 1342 nm was used throughout the experiment. The pump source was a 18-W 808-nm fiber-coupled laser diode with core diameter of 200 μm and numerical aperture of 0.22. Focusing lens with 5 mm focal length and 85% coupling efficiency was used to reimage the pump beam into the laser crystal. The average pump size was approximately 130 μm . The optical cavity length was varied between 2.5 and 7.5 cm, corresponding free spectral range from 6 to 2 GHz. The mode-locked pulses were detected by a high-speed InGaAs photodetector (Electro-optics Technology Inc. ET-3500 with rise time 35 ps),

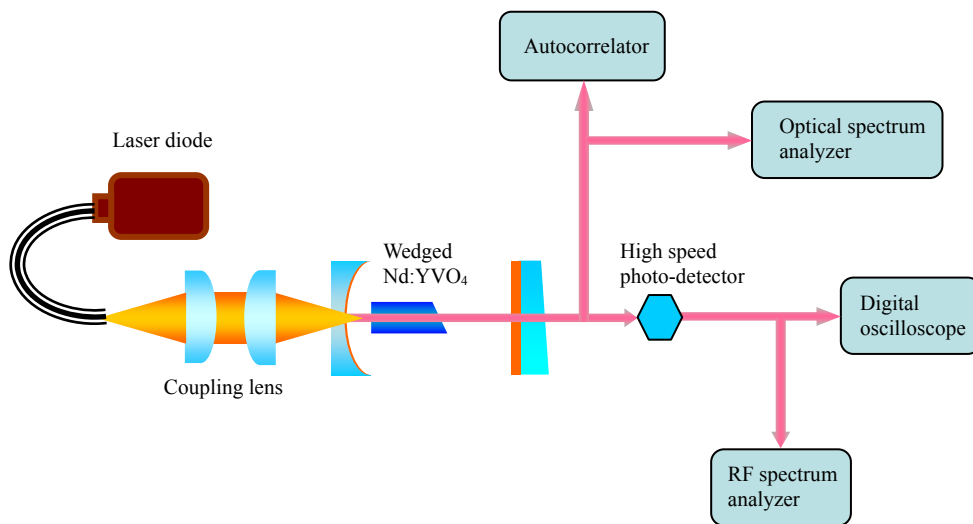


Fig. 2.3-1 Schematic of a diode-pumped self-mode-locked Nd:YVO₄ laser at 1342 nm.

whose output signal was connected to a digital oscilloscope (Agilent, DSO 80000) with 12 GHz electrical bandwidth and sampling interval of 25 ps. The output signal of the photodetector was also analyzed by an RF spectrum analyzer (Advantest, R3265A) with bandwidth of 8 GHz. The spectral information of the laser was monitored by a Fourier optical spectrum analyzer (Advantest, Q8347) that is constructed with a Michelson interferometer with resolution of 0.003 nm.

2.3.2 Experimental Results and Discussions

The optical cavity was first aligned to obtain the maximum average output power and the time trace showed the laser output was in the spontaneous mode-locked state with some amplitude fluctuations. With fine adjusting of the cavity, the amplitude instability was minimized to obtain a nearly perfect stable mode-locked operation. This property is similar to the results of Nd:YVO₄ laser at 1064 nm which mention in the section 2.2. The average output power of the stable cw mode locking was found to be approximately 65% of the maximum average output power. Figure 2.3-2 depicts the average output power at 1342 nm with respect to incident pump power in the optimum power-output operation and in the mode-locked operation with the frequency of 3.365 GHz. In the optimum power-output regime the laser had a slope efficiency of 20.1%; the output power reached 1.85 W at an incident pump power of 10.2 W. As shown in Fig. 2.3-2, in the mode-locked regime the laser had a slope efficiency of 13%; the output power reached 1.2 W at an incident pump power of 10.2 W. Note that once the pump power reaches the lasing threshold, the laser system instantaneously steps into a stable mode-locked operation, i.e., no threshold for the

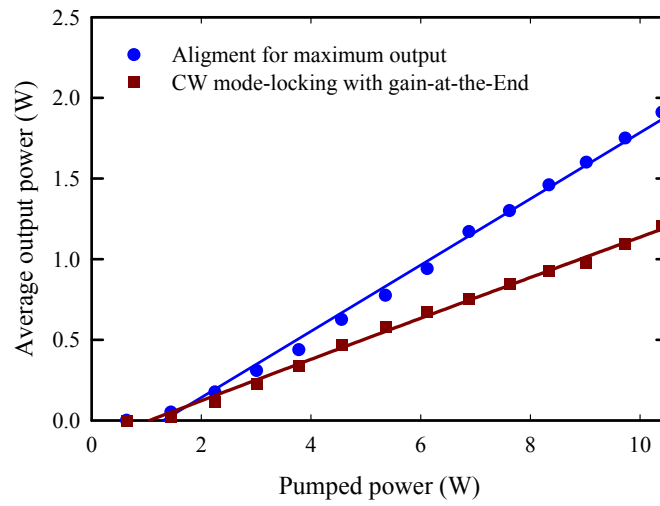


Fig. 2.3-2 Average output power at 1342 nm versus incident pump power in maximum output power operation and mode-locked operation.

self-mode-locking.

It is worth mentioning that the wedge shape of the output coupler is vital for obtaining a completely stable mode-locked operation. When an output coupler without a wedge is used in the laser cavity, the pulse trains exhibit incomplete mode-locking with cw background to a certain extent.

Figures 2.3-3 (a) and 2.3-3 (b) show the pulse trains on two different time scale, one with time span of 5 ns, demonstrating the mode-locked pulses, and the other with time span 5 μ s, demonstrating the amplitude stability. It can be seen that the pulse trains display full modulation and complete mode-locking is achieved. The corresponding power spectrum is depicted in Fig. 2.3-3 (c). The power spectrum reveals that the relative frequency deviation of the power spectra, $\Delta\nu/\nu$, is experimentally found to be significantly smaller than 10^{-4} over day-long operation, where ν is the center frequency of the power spectrum and $\Delta\nu$ is the frequency deviation of FWHM. Experimental results reveal that the laser system can be stably operated in a single-pulse mode-locked state as long as the cavity length is shorter than around 7.5 cm (mode-locked repetition rate > 2 GHz). For cavity length longer than 8.5 cm, a single pulse per round trip was usually observed to split into several pulses. This characteristic is the same as the result in self-mode-locked laser at 1.06 μ m [27].

With a commercial autocorrelator (APE, PulseCheck SM 250 IR), the full width at half maximum (FWHM) trace width of the mode-locked pulse was measured to be 17 ps, and the pulse width was thus estimated to be 11.5 ps assuming the sech^2 -shaped temporal profile, as shown in Fig. 2.3-4 (a). Fig. 2.3-4 (b) shows the

FWHM width of the optical spectrum was 0.22 nm at the central wavelength of 1342.21 nm, giving the time-bandwidth product of the mode-locked pulse of 0.43 indicating the pulses to be frequency chirped and narrow pulse duration to be possible under specific circumstance. To confirm the peak power of the pulses, an experiment of the extra-cavity second-harmonic generation (SHG) was performed. The conversion efficiency for the average power was found to be enhanced by approximately 10 times, quite consistent with the theoretical simulation. The ratio of the peak power to the background for the SHG power was found to be increased by up to 2 orders of magnitude.



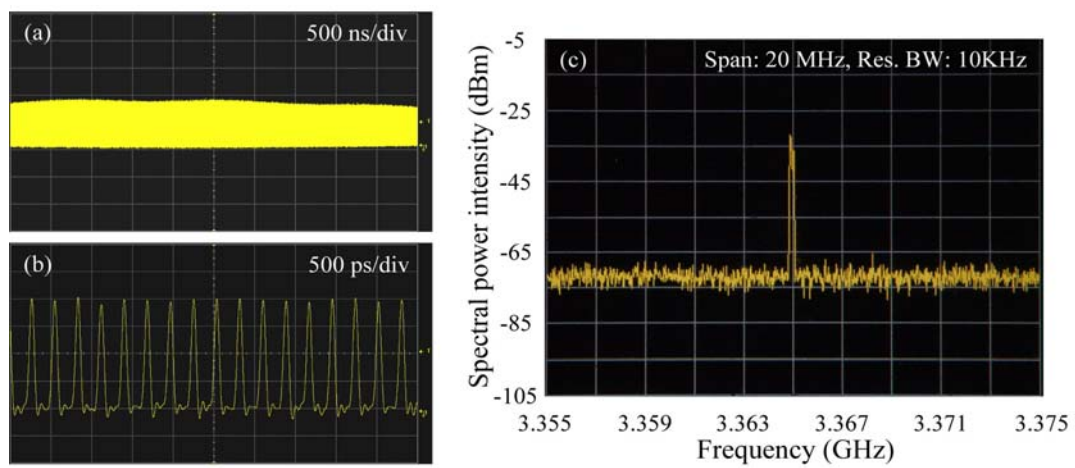


Fig. 2.3-3 Pulse trains on two different time scales. (a) Time span of $5\mu\text{s}$, demonstrating amplitude oscillation. (b) Time span of 5 ns, demonstrating mode-locked pulses. (c) Corresponding power spectrum.

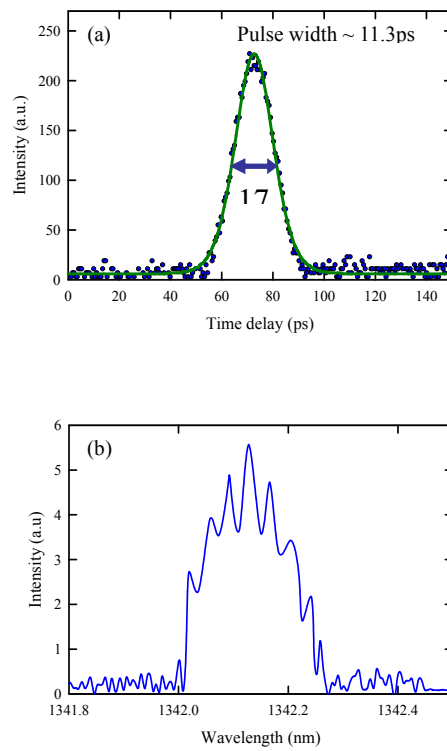


Fig. 2.3-4 (a) Autocorrelation trace of the output pulse from the cw mode-locked Nd:YVO₄ laser. (b) Corresponding optical spectrum of the laser.

2.4 Conclusion

In this chapter we have demonstrated the compact efficient multi-GHz continuous-wave self-mode-locking in the Nd:YVO₄ and Nd:GdVO₄ lasers at 1064nm and 1342 nm. The large third-order nonlinearity of YVO₄ and GdVO₄ are suitable for the generation of nearly stable cw SML. The cavity structure is a simple concave-plano resonator without the need of any additional elements. Since the Nd:GdVO₄ crystal has similar laser properties with Nd:YVO₄ crystal, the experimental results of Nd:GdVO₄ laser are similar to the experimental results of Nd:YVO₄ laser. At 1064 nm operation, with a pump power of 2.5 W, a maximum average output power of 0.7 W and 0.8 W are obtained respectively. Both of these two kinds of laser systems can be obtained in stable single-pulse regime for the cavity length shorter than 7.5 cm. The pulse width of Nd:GdVO₄ laser is 23 ps and is 7.8 ps of Nd:YVO₄ laser for the mode-locked frequency of 2-6 GHz.

When the Nd:YVO₄ laser operates at 1342nm, the average output power was up to 1.2 W at an incident pump power of 10.2 W, which give an optical conversion efficiency of 11.7%. The pulse width was experimentally found as short as 11.5 ps and pulse repetition rate in the range of 2-6 GHz. It is worth mentioning that for the cavity length longer than 8.5 cm, the compact self-mode-locked laser from the single-pulse operation steps into multi-pulse operation. This characteristic is the same as the result in self-mode-locked lasers at 1064 nm. In order to achieve more reliable

SML lasers, it needs further understanding to improve the SML pulse stability. In the next chapter, we have reported the experimental and theoretical results of controlling the number of longitudinal modes for designing more reliable self-mode-locked lasers.



References

- [1] M. H. Crowell, "Characteristics of mode-coupled lasers," *IEEE J. Quantum Electron.* 1, 12 (1965).
- [2] H. Statz and C. L. Tang, "Phase locking of modes in lasers," *J. Appl. Phys.* 36, 3923 (1965).
- [3] M. A. Duguay, S. L. Shapiro, and P. M. Rentzepis, "Spontaneous appearance of picosecond pulses in ruby and Nd:glass lasers," *Phys. Rev. Lett.* 19, 1014 (1967).
- [4] O. L. Gaddy and E. M. Schaefer, "Self locking of modes in the argon ion laser," *Appl. Phys. Lett.* 9, 281 (1966).
- [5] J. Y. Huang, H. C. Liang, k. W. Su, and Y. F. Chen, "High power passively Q-switched ytterbium fiber laser with Cr⁴⁺:YAG as a saturable absorber," *Opt. Express* 15, 473 (2007).
- [6] J. Y. Huang, S. C. Huang, H. L. Chang, K. W. Su, Y. F. Chen, and K. F. Huang, "Passive Q switching of Er-Yb fiber laser with semiconductor saturable absorber," *Opt. Express* 16, 3002 (2008).
- [7] P. Glas, M. Naumann, A. Schirmacher, L. Däweritz, and R. Hey, "Self pulsing versus self locking in a cw pumped neodymium doped double clad fiber laser," *Opt. Commun.* 161, 345 (1999).

References

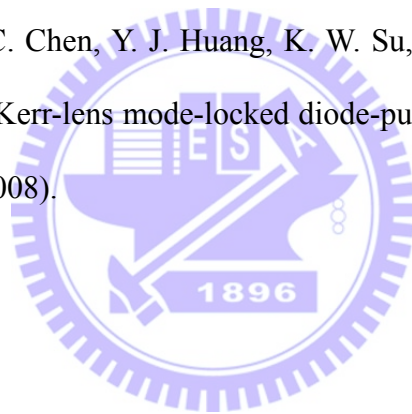
- [8] H. Statz, "On the condition for self-locking of modes in lasers," *J. Appl. Phys.* 38, 4648 (1967).
- [9] H. Statz and M. Bass, "Locking in multimode solid-state lasers," *J. Appl. Phys.* 40, 337 (1969).
- [10] A. A. Kaminskii, K. Ueda, H. J. Eichler, Y. Kuwano, H. Kouta, S. N. Bagaev, T. H. Chyba, J. C. Barnes, G. M. A. Gad, T. Murai, and J. Lu, "Tetragonal vanadates YVO_4 and GdVO_4 – new efficient $\chi^{(3)}$ – materials for Raman lasers," *Opt. Commun.* 194, 201 (2001).
- [11] Y. F. Chen, "High-power diode-pumped active Q-switched Nd:YVO₄ self-Raman laser: Influence of dopant concentration," *Opt. Lett.* 29, 1915 (2004).
- [12] F. Su, X. Y. Zhang, Q. Wang, S. Ding, P. Jia, S. Li, S. Fan, C. Zhang, and B. Liu, "Diode pumped actively Q-switched Nd:YVO₄ self-Raman laser," *J. Phys. D: Appl. Phys.* 39, 2090 (2006).
- [13] X. H. Chen, X. Y. Zhang, Q. P. Wang, P. Li, and Z. H. Cong, "Diode-pumped actively Q-switched c-cut Nd:YVO₄ self-Raman laser," *Laser Phys. Lett.* 6, 26 (2009).
- [14] T. T. Basiev, S. V. Vassiliev, V. A. Konjushkin, V. V. Osiko, A. I. Zagumennyi, Y. D. Zavartsev, S. A. Kutovoi, and I. A. Shcherbakov, "Diode pumped 500-picosecond Nd:GdVO₄ Raman laser," *Laser Phys. Lett.* 1, 237 (2004).
- [15] Y. F. Chen, "Efficient 1521-nm Nd:GdVO₄ Raman laser," *Opt. Lett.* 29, 2632 (2004).
- [16] P. Dekker, H. M. Pask, D. J. Spence, and J. A. Piper, "Continuous-wave, intracavity doubled, self-Raman laser operation in Nd:GdVO₄ at 586.5 nm," *Opt.*

References

- Express 15, 7038 (2007).
- [17] N. Minkovski, G. I. Petrov, and S. M. Saltiel, "Nonlinear polarization rotation and orthogonal polarization generation experienced in a single-beam configuration," *J. Opt. Soc. Am. B* **21**, 1659 (2004).
- [18] A. G Selivanov, I. A. Denisov, N. V. Kuleshov, and K. V. Yumashev, "Nonlinear refractive properties of Yb³⁺-doped KY(WO₄)₂ and YVO₄ laser crystals," *Appl. Phys. B* **83**, 61 (2006).
- [19] A. Major, F. Yoshino, I. Nikolakakos, J. S. Aitchison, and P. W. E. Smith, "Dispersion of nonlinear refractive index in sapphire," *Opt. Lett.* **29**, 602 (2004).
- [20] R. Fluck, G. Zhang, U. Keller, K. J. Weingarten, and M. Moser, "Diode-pumped passively mode-locked 1.3- μm Nd:YVO₄ and Nd:YLF lasers by use of semiconductor saturable absorbers," *Opt. Lett.* **21**, 1378 (1996).
- [21] O. Musset and J. P. Boquillon, "Comparative laser study of Nd:KGW and Nd:YAG near 1.3 μm ," *Appl. Phys. B* **64**, 503 (1997).
- [22] H. J. Zhang, J. H. Liu, J. Y. Wang, X. G. Xu, and M. H. Jiang, "Continuous-wave laser performance of Nd:LuVO₄ crystal operating at 1,34 μm ," *Appl. Opt.* **44**, 7439 (2005).
- [23] H. T. Huang, J. L. He, C. H. Zuo, H. J. Zhang, J. Y. Wang, and H. T. Wang, "Co²⁺:LMA crystal as saturable absorber for a diode-pumped passively Q-switched Nd:YVO₄ laser at 1342 nm," *Appl. Phys. B* **89**, 319 (2007).
- [24] Y. F. Chen, L. J. Lee, T. M. Huang, and C. L. Wang, "Study of high-power diode-end-pumped Nd:YVO₄ laser at 1.34 μm : influence of Auger

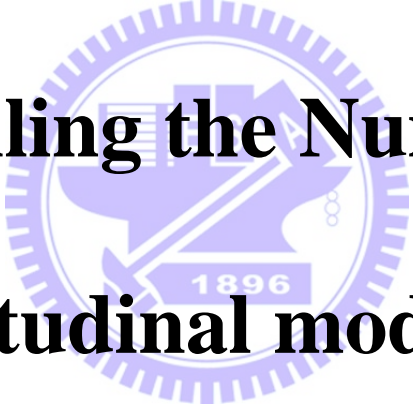
References

- upconversion,” *Opt. Commun.* **163**, 198 (1999).
- [25] R. Zhou, S. C. Ruan, C. L. Du and J. Q. Yao, “High-power continuous-wave diode-end-pumped intracavity-frequency-doubled Nd:GdVO₄/LBO red laser,” *Opt. Commun.* **282**, 605 (2009).
- [26] R. Paschotta, L. Krainer, S. Lecomte, G. J. Spühler, S. C. Zeller, A. Aschwanden, D. Lorensen, H. J. Unold, K. J. Weingarten, and U. Keller, “Picosecond pulse sources with multi-GHz repetition rates and high output power,” *New J. Phys.* **6**, 174 (2004).
- [27] H. C. Liang, R. C. C. Chen, Y. J. Huang, K. W. Su, and Y. F. Chen, “Compact efficient multi-GHz Kerr-lens mode-locked diode-pumped Nd:YVO₄ laser,” *Opt. Express* **16**, 21149 (2008).



Chapter 3

**Controlling the Number of
Longitudinal modes for
Designing Reliable
Self-Mode-Locked Lasers**



3.1 Influence of Number of Longitudinal Modes on Self-Mode-Locked Lasers

Although the spontaneous mode locking (SML) typically occurs in a multimode laser without employing an extra nonlinearity except the gain medium, the SML phenomenon is still not very reliable and usually occurs in pulse lasers. Recently, nevertheless the continuous-wave SML pluses have been demonstrated in Nd:YVO₄ and Nd:GdVO₄ Lasers [1-3]; the fairly stable self-mode-locked laser only can be operated with the pulse repetition rate in the range of 2-6 GHz. When the cavity length is longer than 7.5 cm, the single output pulse split into several pulses. Besides the disgusted characteristic of multi-pulse, several authors independently have found the experimental results which are not in agreement with the ideal mode-locking [4-6]. The measured pulse widths were longer and an additional background intensity was observed. These deviations from ideal mode locking may have several causes. One such possibility is systematic phase deviations [7,8] and another is the number of the longitudinal modes.

Although a systematic phase fluctuation is usually caused by dispersion effects, theoretical studies on the SML mechanism have confirmed that the combination tones of the third order nonlinear polarization terms can help in compensating the dispersion-induced phase. Nevertheless, the locking strength due to the presence of the nonlinear polarization terms is not rather substantial. Figure 3.1-1 shows the

numerical calculation of the output pulse with different number of modes at the systematic phase of $\pi/10$. It can be seen in Fig. 3.1-1, when the number of longitudinal modes are fewer, the small systematic phase deviation can not destroy the output pulses. The different between ideal mode-locked pulses and nonideal mode-locked pulses is found to be negligible. Numerical results reveal that the output pulses become incomplete with increasing the number of longitudinal modes, as shown in Fig. 3.1-1(c). Therefore, the precise control of the number of longitudinal lasing modes is crucial for achieving more reliable SML lasers.

Spatial hole burning (SHB) in the gain medium has been confirmed to advantageously utilized for lasing mode selection [9-14]. In this chapter we experimentally confirm that the separation between the gain medium and the end mirror in a standing-wave SML laser cavity can be employed to precisely control the number of longitudinal lasing modes via the SHB effect, leading to a stability improvement of the mode-locked pulses. For the purpose of developing design guideline, we also derive a practical formula that gives an analytical estimate for the maximum number of longitudinal modes.

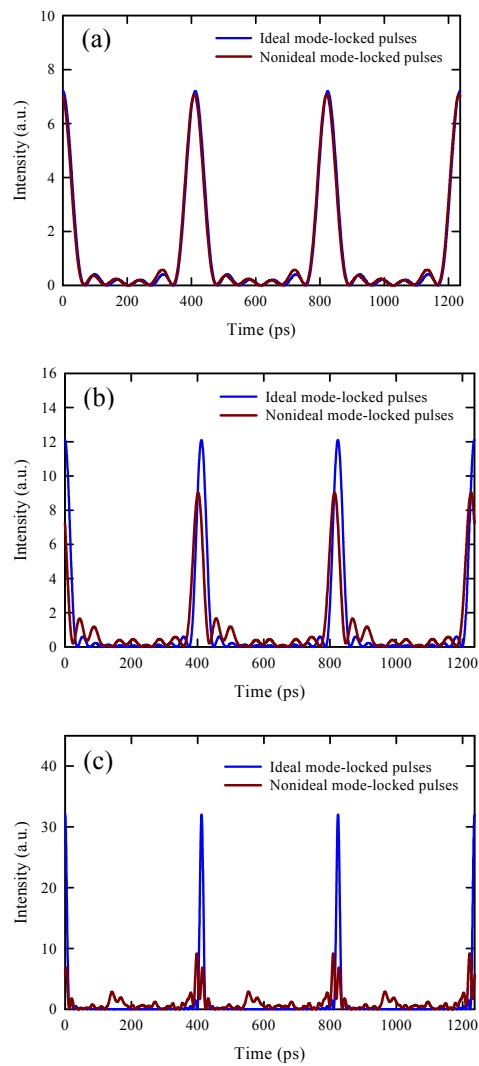


Fig. 3.1-1. Output pulses in the ideal mode-locked operation and nonideal mode-locked operation with different longitudinal modes. (a) 5 longitudinal modes. (b) 10 longitudinal modes. (c) 30 longitudinal modes.

3.2 Experimental Setup

We have demonstrated that the large third-order nonlinearity of Nd:YVO₄ crystal could be used to achieve a short-cavity SML operation [1]. Here we employ the Nd:YVO₄ crystal to explore the influence of the number of longitudinal lasing modes on the stability of SML performance. An experimental setup is shown schematically in Figure 3.2-1. The cavity configuration is a simple concave-plano resonator. The separation between the laser gain medium and the input mirror, d , is freely adjusted in the range of 1-11 mm to control the number of longitudinal lasing modes via the SHB effect. The gain medium is a-cut 0.5 at.% Nd:YVO₄ crystal with dimensions 3 mm × 3 mm × 10 mm. Both end surfaces of the Nd:YVO₄ crystal were anti-reflection coated at 1064 nm and wedged 2° to avoid the Fabry-Perot etalon effect. The laser crystal was wrapped with indium foil and mounted in a water-cooled copper holder. The water temperature was maintained at around 20 °C to ensure stable laser output. The input mirror was a 20-cm radius-of-curvature mirror with anti-reflection at 808 nm on the entrance face and was high-reflection at 1064 nm (>99.8%) and high-transmission at 808 nm on the second surface. A flat wedged output coupler with 15% transmission at 1064 nm was used throughout the experiment. The pump source was a 3-W 808-nm fiber-coupled laser diode with core diameter of 100 μm and numerical aperture of 0.20. Focusing lens with 25 mm focal length and 85% coupling efficiency was used to reimaging the pump beam into the laser crystal. The average pump size was

Ch3 Controlling the Number of Longitudinal Modes for Designing Reliable Self-Mode-locked Lasers

approximately 60 μm . The optical cavity length was set to be approximately 2.92 cm, corresponding to a free spectral range of 5.14 GHz. The mode-locked pulses were detected by a high-speed InGaAs photodetector (Electro-optics Technology Inc. ET-3500 with rise time 35 ps), whose output signal was connected to a digital oscilloscope (Agilent, DSO 80000) with 12 GHz electrical bandwidth and sampling interval of 25 ps. The output signal of the photodetector was also analyzed by an RF spectrum analyzer (Advantest, R3265A) with bandwidth of 8 GHz. The spectral information of the laser was monitored by a Fourier optical spectrum analyzer (Advantest, Q8347) that is constructed with a Michelson interferometer with resolution of 0.003 nm



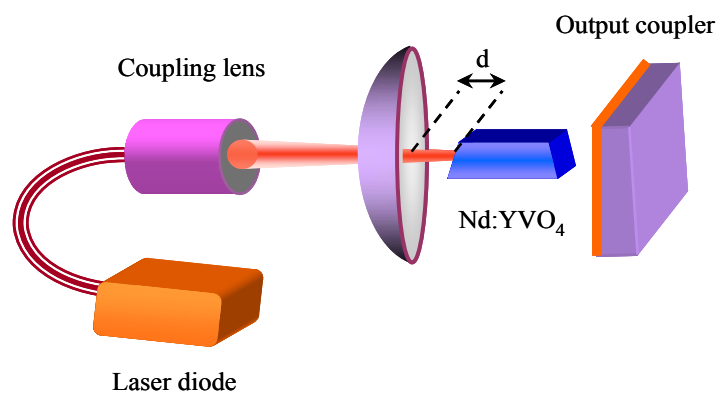


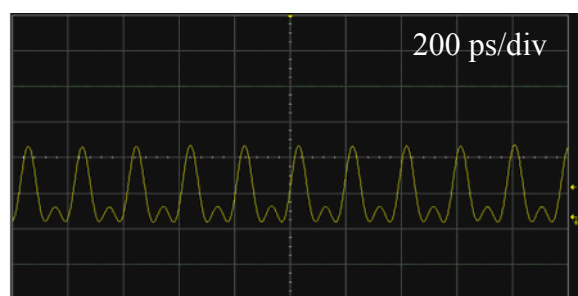
Fig. 3.2-1. Schematic of a diode-pumped self-mode-locked Nd:YVO₄ laser.

3.3 Stability Improvement and Pulse Width Control for Short-Cavity Self-Mode-locked Nd:YVO₄ Lasers

Firstly, the laser cavity was aligned with the optical cavity length of 2.92 cm. With the real-time dynamical temporal trace, the laser cavity can easily adjusted to be in a SML operation with pulse repetition rate of 5.14 GHz, as shown in Fig. 3.3-1. We also found that the average output power is nearly independent of the crystal/mirror separation d in the range of 1-11 mm. Even so, the number of longitudinal lasing modes was found to be decreased with increasing the separation d . Therefore, the pulse width can be adjusted by changing the crystal/mirror separation to control the amount of spatial hole burning. With the high resolution (0.003 nm) optical spectrum analyzer, the optical spectrums have measured, as shown in Fig. 3.3-2. It can be clearly seen that the number of longitudinal lasing modes decrease from 14 to 4 modes as the separation d change from 1 mm to 9 mm. As the consequently, with increasing crystal/mirror spacing up to 11 mm, the mode-locked pulse width varies smoothly from 9 to 39 ps, and the spectral bandwidth varies from 77 to 15.4 GHz, as shown in Fig. 3.3-3. This result confirms the speculation that the spatial hole burning is also effective in passively mode-locked lasers [10].

Besides the pulse width can be varied by controlling the number of longitudinal lasing modes in self-mode-locked laser with SHB effect. Experimental results revealed that the stability of the mode-locked pulse train also could be significantly

(a)



(b)

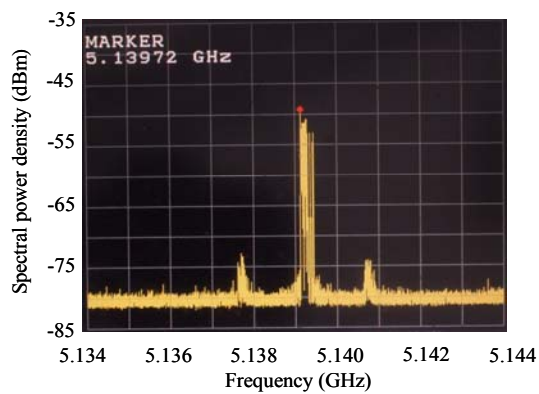


Fig. 3.3-1. (a) Pulse trains for time span 2 ns, demonstrating the mode-locked pulses. (b) Corresponding power spectrum.

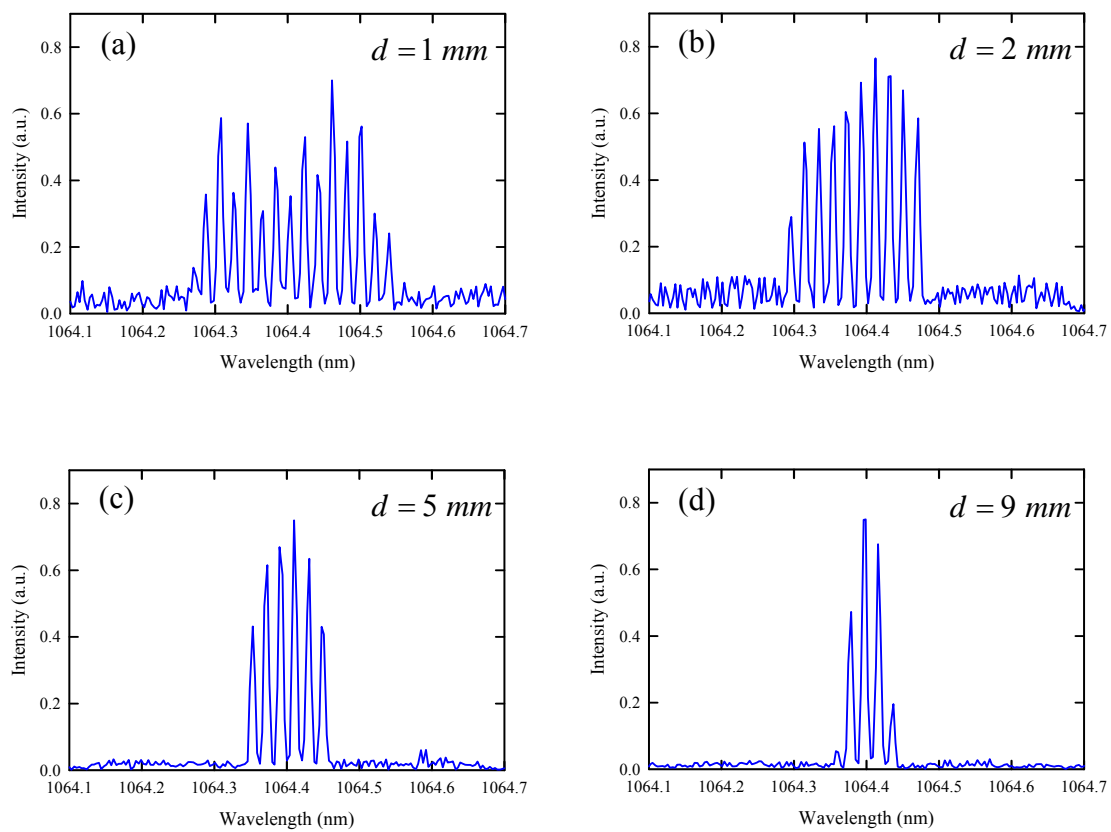


Fig. 3.3-2. Optical spectrum for different crystal/mirror separations d . (a) $d = 1$ mm. (b) $d = 2$ mm. (c) $d = 5$ mm. (d) $d = 9$ mm.

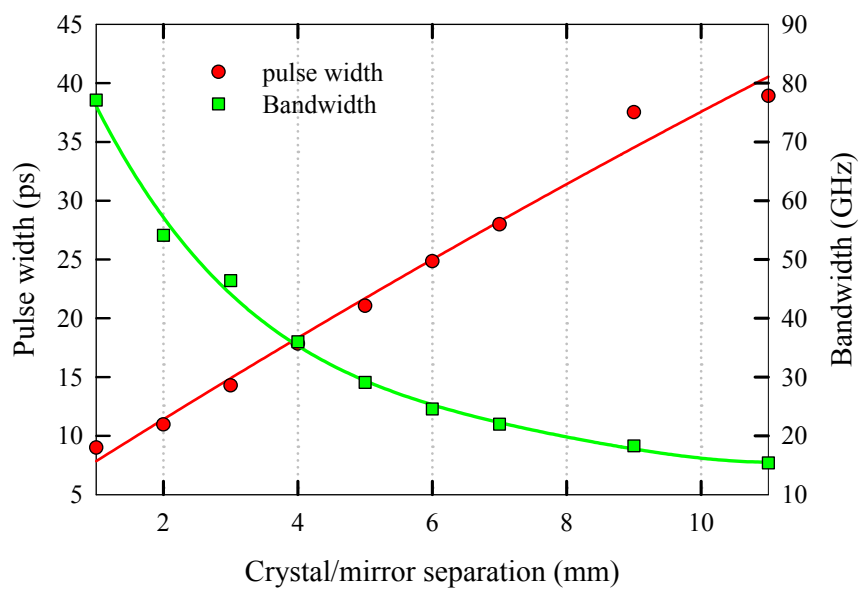


Fig. 3.3-3. Mode-locked pulse width and bandwidth as function of crystal/mirror separation.

improved with decreasing the number of longitudinal lasing modes. With the optimal alignment for $d = 1 \text{ mm}$, the laser oscillates with 16 longitudinal modes and the pulse trains have some amplitude fluctuation, as shown in Fig. 3.3-4(a). The corresponding power spectrum is shown in Fig. 3.3-4(b). It can be seen that the relative frequency deviation of the power spectrum, $\Delta\nu/\nu$, is 3×10^{-4} , where ν is the center frequency of the power spectrum and $\Delta\nu$ is the frequency deviation of full width at half maximum. On the other hand, when the cavity is aligned for the crystal/mirror separation $d = 11 \text{ mm}$, the laser output pulses exhibit more stable with lower amplitude fluctuation and the relative frequency deviation of the power spectrum is smaller than 7.8×10^{-5} , as seen in Fig. 3.3-4(c) and 3.3-4(d). Therefore, the more amplitude fluctuation the mode-locked lasers exhibit, the bigger the relative frequency deviation of the power spectrum is. Figure 3.3-5 depicts that the relative frequency deviation of the power spectrum versus the number of longitudinal lasing modes. As shown in Fig. 3.3-5, reducing the number of longitudinal lasing modes can diminish the amplitude fluctuation to effectively improve the SML pulse stability.

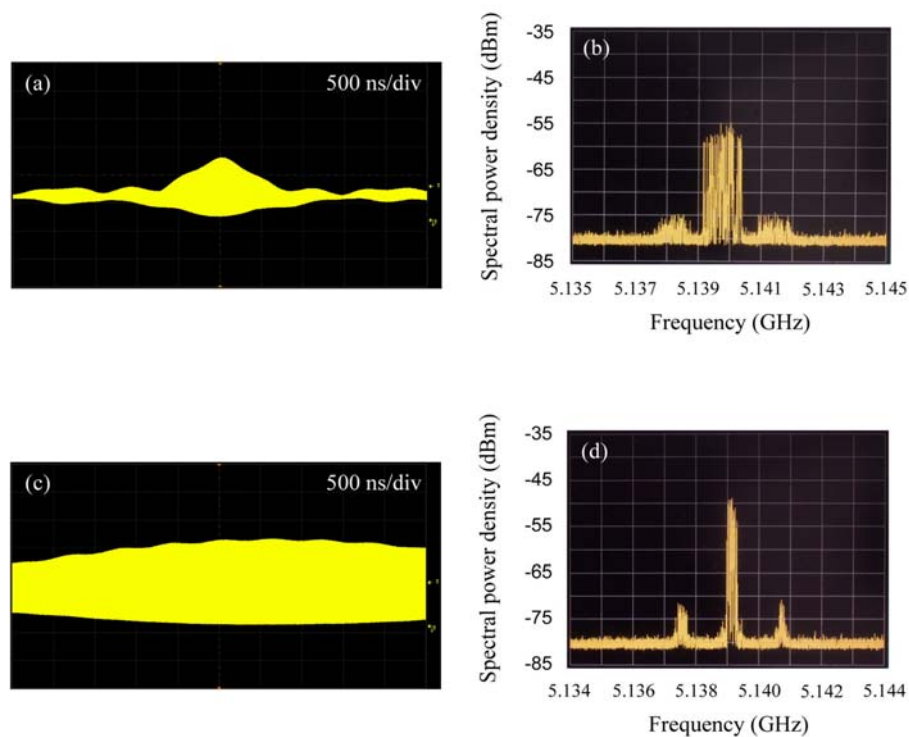


Fig. 3.3-4. Mode-locked pulse trains and power spectrum for two different crystal/mirror separation d . (a) Pulse trains of time span $5 \mu\text{s}$ for $d = 1 \text{ mm}$. (b) Corresponding power spectrum. (c) $d = 11 \text{ mm}$. (d) Corresponding power spectrum.

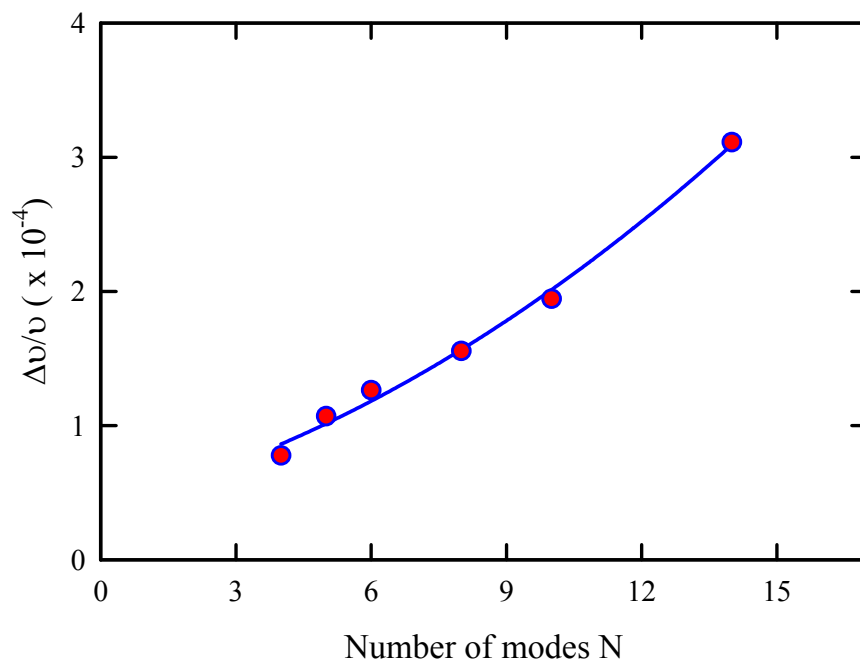


Fig. 3.3-5. Relative frequency deviation of the power spectrum $\Delta\nu/\nu$.

3.4 Theoretical Model for Estimating Maximum Longitudinal Lasing Modes in Self-Mode-Locked Lasers

Since the number of longitudinal modes play a critical role for the stability of SML operation, it is useful to develop a method for estimating the number of lasing modes. In this section, we extend the early work of Zayhowski [14] to derive an analytical formula for estimating the maximum number of longitudinal modes in term of the cavity geometry and well-know material parameters.

For a standing-wave laser consisting of N oscillating modes all with equal amplitudes and with the phases identically zero, the electric field is given by

$$E_N(x, y, z, t) = \left[\frac{1}{\sqrt{N}} \sum_{m=0}^{N-1} e^{i\omega_m t} \sin(k_m z) \right] \psi(x, y, z) \quad (3.4.1)$$

where $\omega_m = (\omega_0 + m)\pi c/l_{cav}$, $k_m = \omega_m/c$, m_0 is the resonant mode index, and l_{cav} is the effective cavity length. The transverse wave function $\psi(x, y, z)$ is given by

$$\psi(x, y, z) = \sqrt{2/\pi w_l^2} \exp\left[-(x^2 + y^2)/w_l^2\right]. \quad (3.4.2)$$

where w_l is the beam radius. Since the cavity length is much longer than the laser wavelength, the typical value of m_0 is greater than 10^3 . Thus it always holds

$N \ll m_0$. After some algebra, the intensity $I_N(x, y, z, t) = |E_N(x, y, z, t)|^2$ can be expressed as

$$I_N(x, y, z, t) = N/2l_{cav} \left\{ \left[S_N(\pi(ct+z)/2l_{cav}) \right]^2 + \left[S_N(\pi(ct-z)/2l_{cav}) \right]^2 - 2S_N(\pi(ct+z)/2l_{cav})S_N(\pi(ct-z)/2l_{cav})\cos 2kz \right\} |\psi(x, y, z)|^2, \quad (3.4.3)$$

where $S_N(\theta) = \sin(N\theta)/N\sin(\theta)$ and $k = [m_0 + (N-1)/2]\pi/l_{cav} \approx \omega_0/l$. The intensity $I_N(x, y, z, t)$, average over a round trip time $T = 2l_{cav}/c$, becomes

$$\langle I_N(x, y, z) \rangle = (1/l_{cav}) [1 - S_N(\pi z/l_{cav})\cos(2kz)] |\psi(x, y, z)|^2. \quad (3.4.4)$$

The function represents a standing-wave pattern which is fully modulated for the position near the reflecting mirrors and continuously loses contrast for the position away from the mirror. Due to the standing-wave nature, superposition of the light fields of modes results in an envelope function for the total light intensity. The spatial variation of the envelope $S_N(\pi z/l_{cav})$ occurs on the cavity-length scale to be much slower compared to rapid undulations of the intensities of individual modes. As N get larger, $S_N(\pi z/l_{cav})$ becomes narrower such that it only has weight very close to the end mirror, i.e., $z=0$ and $z=l_{cav}$. For a convenient numerical evaluation we use a Gaussian function

$$g_N(z) = e^{-[N\pi z/2l_{cav}]^2} + e^{-[N\pi(l_{cav}-z)/2l_{cav}]^2}, \quad (3.4.5)$$

to replace the envelope function $S_N(\pi z/l_{cav})$. In term of $g_N(z)$, the average intensity in Eq. (3.4.4) can be written as

$$\langle I_N(x, y, z) \rangle = |\psi(x, y, z)|^2 [1 + g_N(z)] / l_{cav} - G_{res}(x, y, z, N), \quad (3.4.6)$$

with

$$G_{res}(x, y, z, N) = (2/l_{cav}) \cos^2(kz) g_N(z) |\psi(x, y, z)|^2, \quad (3.4.7)$$

where $G_{res}(x, y, z, N)$ represents the intensity distribution of the residual gain for a standing-wave laser consisting N oscillating modes. Figure 3.4-1 depicts the calculated results for $G_{res}(x, y, z, N)$ and $\langle I_N(x, y, z) \rangle$ as a function of z , where we take $N = 11$, $x = y = 0$, and $m_0 = 200$ for the convenience of presentation.

The maximum number of modes N_{max} that can oscillate in a standing-wave cavity is determined from the condition that the maximum value of N in $G_{res}(x, y, z, N)$ leads to the effective round-trip gain not less than the round-trip loss, i.e.,

$$2\sigma l_g (P_{abs} \tau / h\nu_p) \int \int G_{res}(x, y, z, N) r_p(x, y, z) dV \Big|_{N=N_{max}} \geq \ln(1/R) + L, \quad (3.4.8)$$

where σ is the stimulated emission cross section, l_g is the length of the gain medium, P_{abs} is the absorbed pumped power, ν_p is the pump frequency, τ is the emission lifetime, L is the round-trip loss, R is the reflectivity of the output

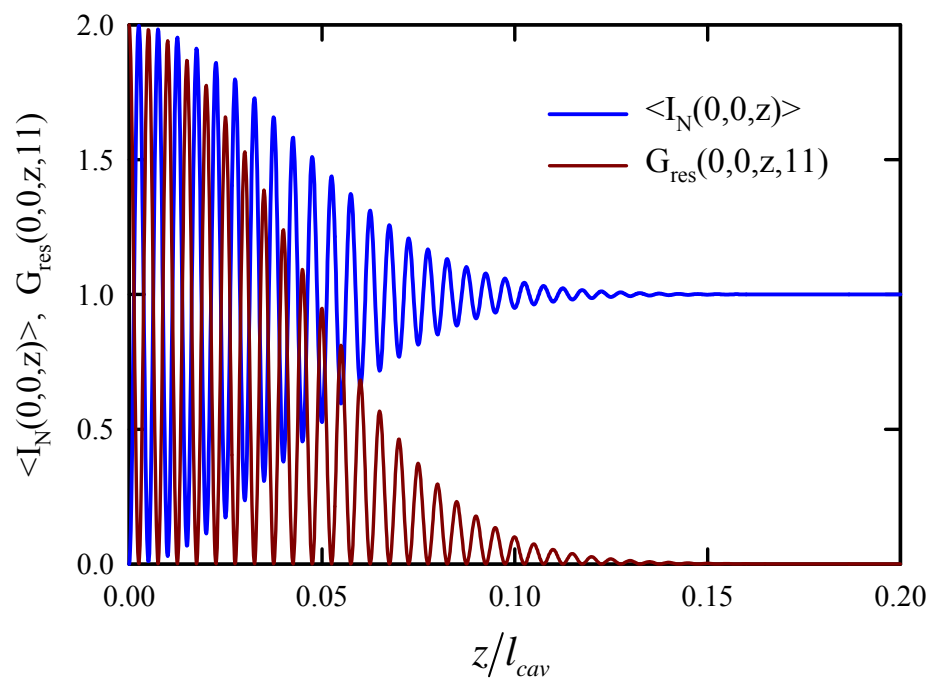


Fig. 3.4-1. Calculated results for $G_{res}(x, y, z, N)$ (darkred line) and $\langle I_N(x, y, z) \rangle$ (bule line) as function of z with $N=11$, $x=y=0$, and $m_0=200$.

coupler, and $r_p(x, y, z)$ is the normalized pump intensity distribution. For a gain medium located between $z = d$ and $z = d + l_g$ and using a circular Gaussian beam to express the pump distribution, $r_p(x, y, z)$ is given by

$$r_p(x, y, z) = (2/\pi w_p^2) \left[\alpha e^{-\alpha(z-d)} / 1 - e^{-\alpha l_g} \right] e^{-2(x^2+y^2)/w_p^2} \Theta(z-d) \Theta(d+l_g-z), \quad (3.4.9)$$

where α is the absorption coefficient at the pump wavelength, w_p is the pump radius, and $\Theta()$ is the Heaviside step function. Substituting Eq. (3.4.7) and Eq. (3.4.9) into Eq. (3.4.8) and carrying out the integration in the transverse directions, we can obtain the relationship of $\eta_{res}(N, d) \Big|_{N=N_{max}} \geq \zeta$, where the residual gain overlap parameter $\eta_{res}(N, d)$ is defined as

$$\eta_{res}(N, d) = (2/l_{cav}) \left[\alpha l_g / 1 - e^{-\alpha l_g} \right] \int_d^{d+l_g} \cos^2(kz) g_N(z) e^{-\alpha(z-d)} dz, \quad (3.4.10)$$

and the effective loss-to-pump factor ζ is defined as

$$\zeta = [\ln(1/R) + L] \left[\pi(w_l^2 + w_p^2) / 2\sigma \right] \left[h\nu_p / P_{abs}\tau \right], \quad (3.4.11)$$

As a result, the maximum number of modes N_{max} can be determined with the criterion $\eta_{res}(N, d) \Big|_{N=N_{max}} \geq \zeta$ and Eq. (3.4.10) and Eq. (3.4.11). Figure 3.4-2 shows the calculated results for $\eta_{res}(N, d)$ as a function of N for several different values of d for the case of the Nd:YVO₄ laser: $l_{cav} = 29 \text{ mm}$, $l_g = 6 \text{ mm}$, and $\alpha = 0.5 \text{ mm}^{-1}$.

From Fig. 3.4-2, it is clear that the maximum number of modes N_{\max} is decreased with increasing d . For the experimental condition which reported above, the effective loss-to-pump factor ζ can be found to be 6.19×10^{-3} , where the values of the parameters are as follows: $\sigma = 2.5 \times 10^{-18} \text{ cm}^2$, $P_{\text{abs}} = 1.5 \text{ W}$, $\tau = 100 \mu\text{s}$, $R = 0.85$, $L = 0.005$, $h\nu_p = 2.45 \times 10^{-19} \text{ J}$, $w_l = 0.06 \text{ mm}$, and $w_p = 0.06 \text{ mm}$. Applying $\zeta = 6.19 \times 10^{-3}$ into Fig. 3, the maximum number of modes N_{\max} can be determined as a function of d , depicted in Fig. 3.4-3. The good agreement between the theoretical estimations and the experimental data validates the usefulness of the present model.



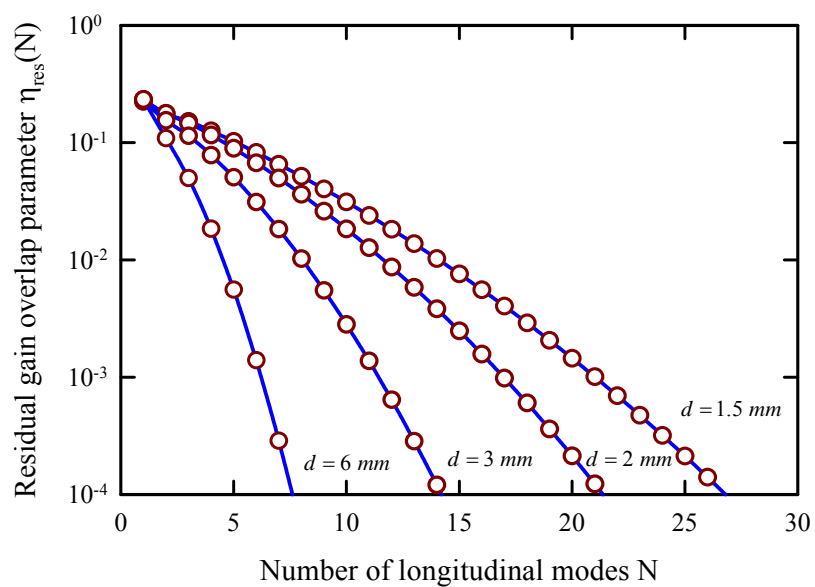


Fig. 3.4-2. Calculated results for $\eta_{res}(N, d)$ as a function of N for several different value of d for the case of the Nd:YVO₄ laser: $l_{cav} = 29 \text{ mm}$, $l_g = 6 \text{ mm}$, and $\alpha = 0.5 \text{ mm}^{-1}$.

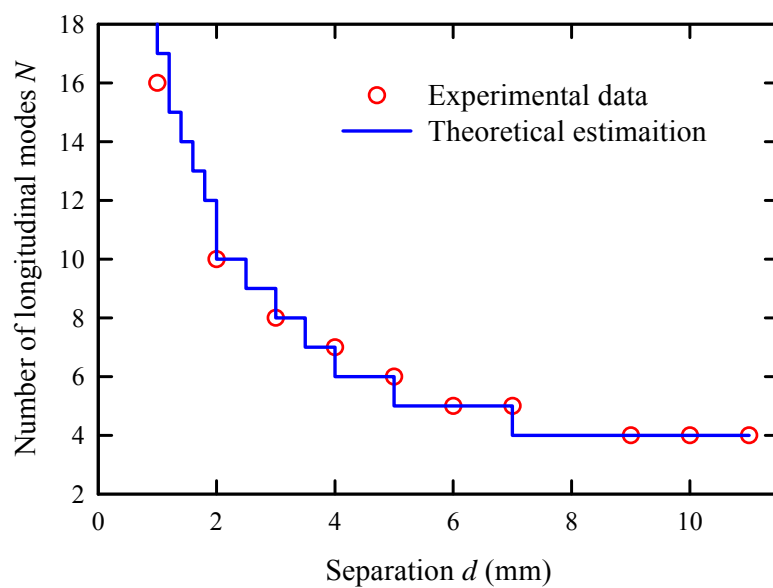
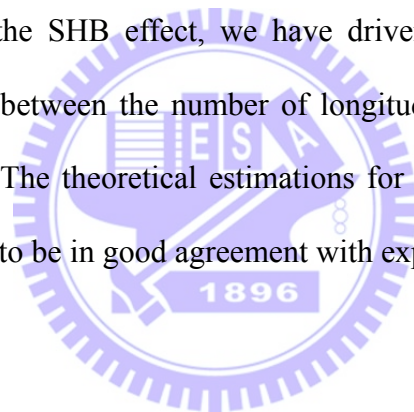


Fig. 3.4-3. Theoretical estimations and experimental data for the maximum number of modes N_{\max} as function of d .

3.5 Conclusion

We have experimentally confirmed that a reliable spontaneous mode-locked (SML) can occur in short-cavity Nd:YVO₄ lasers without employing an extra nonlinearity. We further found that the stability of SML pulses could be significantly improved by reducing the number of longitudinal lasing modes to diminish the phase fluctuation. Considering the SHB effect, we have driven an analytical formula to establish the relationship between the number of longitudinal lasing modes and the crystal/mirror separation. The theoretical estimations for the number of longitudinal lasing modes were shown to be in good agreement with experimental observations.



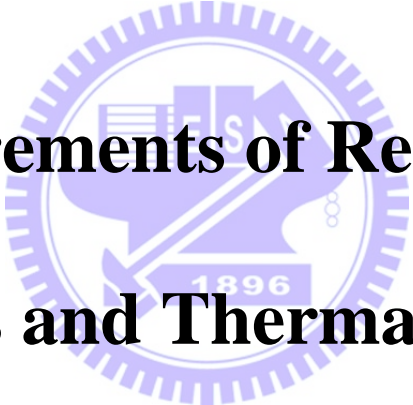
References

- [1] H. C. Liang, R. C. C. Chen, Y. J. Huang, K. W. Su, and Y. F. Chen, "Compact efficient multi-GHz Kerr-lens mode-locked diode-pumped Nd:YVO₄ laser," *Opt. Express* 16, 21149 (2008).
- [2] H. C. Liang, H. L. Chang, W. C. Huang, K. W. Su, Y. F. Chen, and Y. T. Chen, "Self-mode-locked Nd:GdVO₄ laser with multi-GHz oscillations: manifestation of third-order nonlinearity," *Appl. Phys. B* 97, 451 (2009).
- [3] H. C. Liang, Y. J. Huang, W. C. Huang, K. W. Su, and Y. F. Chen, "High-power, diode-end-pumped, multigigahertz self-mode-locked Nd:YVO₄ laser at 1342 nm," *Opt. Lett.* 35, 4 (2010).
- [4] J. A. Armstrong, "Measurement of picosecond laser pulse widths," *Appl. Phys. Lett* 10, 16 (1967).
- [5] J. A. Giordmaine, P. M. Rentzepis, S. L. Shapiro, and K. W. Wecht, "Two photon excitation of fluorescence by picosecond light pulses," *Appl. Phys. Lett.* 11, 216 (1967).
- [6] H. P. weber, "Generation and measurement of ultrashort light pulses," *J. Appl. Phys.* 39, 6041 (1968).
- [7] R. Dändliker, H. P. Weber, and A. A. Grütter, "Influence of systematic phase deviations on the output of mode-locked lasers," *J. Appl. Math. Phys.* 20, 572

References

- (1969).
- [8] A. A. Grütter, R. Dändliker, H. P. Weber, “The output intensity of a non-ideally mode-locked laser,” *J. Appl. Math. Phys.* 20, 574 (1969).
- [9] R. Paschotta, J. Aus der Au, G. J. Spühler, S. Erhard, A. Giesen, and U. Keller, “Passive mode locking pg this-disk laser: effect of spatial hole burning,” *Appl. Phys. B* 72, 267 (2001).
- [10] C. J. Flood, D. R. Walker, and H. M. van Driel, “Effect of spatial hole burning in a mode-locked diode end-pumped Nd:YAG laser,” *Opt. Lett.* 20, 58 (1995).
- [11] H. S. Kim, S. K. Kim, and B. Y. Kim, “Longitudinal mode control in few-mode erbium-doped fiber lasers,” *Opt. Lett.* 21, 1144 (1996).
- [12] L. Jiang and L. V. Asryan, “How many longitudinal modes can oscillate in a quantum-dot laser: an analytical estimate,” *IEEE Photon. Technol. Lett.* 20, 1661 (2008).
- [13] G. J. Kintz and T. Baer, “Single frequency operation in solid-state laser materials with short absorption depths,” *IEEE Quantum Electron.* 26, 1457 (1990).
- [14] J. J. Zayhowski, “Limits imposed by spatial hole burning on the single-mode operation of standing-wave laser cavities,” *Opt. Lett.* 15, 431 (1990).

Chapter 4



Measurements of Refractive Indexes and Thermal Optical Coefficient: Application of Self-Mode-Locked Lasers

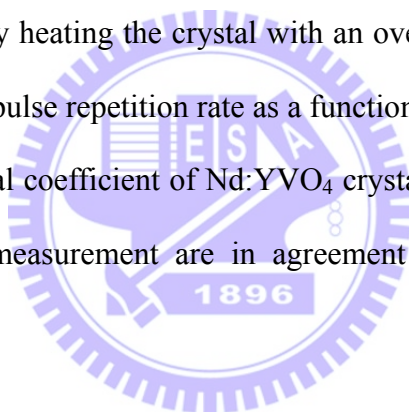
4.1 Refractive Indexes and Thermal Optical Coefficient

The refractive index of the material medium is an important optical parameter since it exhibits the optical properties of the material. Its values are usually required to interpret various types of spectroscopic data. The common method for measuring the refractive index is using the ellipsometer. In generally, this method only can measure the thin film materials but not the bulk materials. Besides the refractive indexes of crystals, thermal optical coefficient is another important parameter of crystals, since it directly influences the pumped-power-induced thermal lensing that expressed by [1]

$$f_{th} = \frac{\pi K \omega_p^2}{\xi P_{in} (dn/dT)} \left[\frac{1}{1 - \exp(-\alpha l_c)} \right], \quad (4.1.1)$$

In solid-state lasers, this pumped induced thermal lens is of primary importance because of its significant influence on laser stability, oscillation mode size, maximum achievable average power, efficiency, and output beam quality [2-4]. Therefore, a knowledge of the thermal optical coefficient in the direction parallel and perpendicular to the c-axis of the anisotropic crystals like Nd:YVO₄ and Nd:GdVO₄ are necessary. Recently, several researchers have measured the thermal optical coefficient of a Nd:GdVO₄ crystal by measuring the focal length of thermal lens as a function of the pumped power [5,6]. More recently, the stable self-mode-locked Nd:YVO₄ lasers are successful developing at the lasing wave length of 1064 nm and

1342 nm [7,8]. The mode-locked pulse repetition rate is sensitive to the variation of optical path length. It is possible to utilize the sensitive properties of self-mode-locked for measuring the refractive index of crystals. Here, we have demonstrated a novel method to measure the ordinary and extraordinary refractive indexes of Nd:YVO₄ with different doped concentration by measuring the repetition rate shifts of the mode-locked Nd:YVO₄ laser as a crystal is placed inside the laser cavity. We also have measured several crystals such as Nd:GdVO₄, Nd:YGdVO₄, and KTP in the same laser configuration. On the other hand, the thermal optical coefficients were experimentally obtained by heating the crystal with an oven. In this method, with the measured variation of the pulse repetition rate as a function of the temperature, we can estimate the thermal optical coefficient of Nd:YVO₄ crystal. The experimental results reveal that both of the measurement are in agreement with that reported in the literature [9-15].



4.2 Experimental Setup

Figure 4.2-1 depicts the configuration the experimental setup. Firstly, the stable self-mode-locked lasers are achieved for operating at 1064 nm and 1342 nm. The mode-locked cavity is a simple concave-plano resonator. The gain medium is a-cut 0.2 at. % Nd:YVO₄ crystal with a length of 10 mm. Both end surface of the Nd:YVO₄ crystal were wedge 2° to suppress the Fabry-Perot etalon effect. The laser crystal was wrapped with indium foil and mounted in a water-cooled copper holder. The water temperature was maintained around 20 °C to ensure stable laser output. The input mirror was a 504 mm radius-of-curvature concave mirror with antireflection coating at 808 nm on the entrance face and high transmittance coating at 808 nm on the second surface. Two kinds of output coupler are used for different operation at 1064 nm and 1342 nm. The pump source was a 3-W 808-nm fiber-coupled laser diode with a core diameter of 100 μm and a numerical aperture of 0.16. Focusing lens with 25 mm focal length and 85% coupling efficiency was used to re-image the pump beam into the laser crystal. The average pump size was approximately 70 μm. The samples are placed behind of the laser gain medium near the output coupler.

The optical cavity length was set to be approximately 5.4 cm with the corresponding free spectral range (FSR) of 2.75 GHz. The mode-locked pulses were detected by a high-speed InGaAs photodetector (Electro-optics Technology Inc. ET-3500 with rise time 35 ps), whose output signal was connected to a digital

Ch4 Measurements of Refractive Indexes and Thermal Optical Coefficient: Application of Self-Mode-Locked Lasers

oscilloscope (Agilent, DSO 80000) with 12 GHz electrical bandwidth and sampling interval of 25 ps. At the same time, the output signal of the photodetector was also analyzed by an RF spectrum analyzer (Advantest, R3265A) with bandwidth of 8.0 GHz.



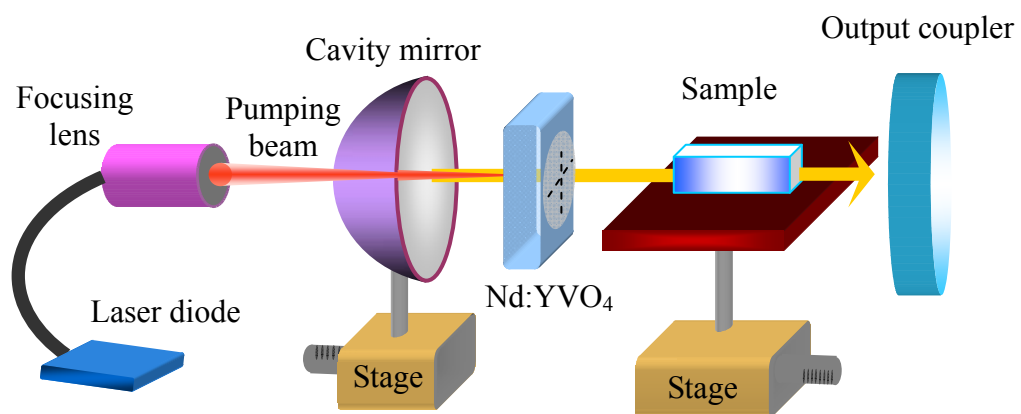


Fig. 4.2-1. The configuration of the refractive indexes measuring system.

4.3 Experimental Results and Analysis

First of all, the stable self-mode-locked are established for operating at 1064 nm and 1342 nm. The pulse repetition rates are measured at the frequency of 2.748 GHz. The relative frequency deviation of the power spectrum, $\Delta\nu/\nu$, is smaller than 6×10^{-5} , where ν is the center frequency of the power spectrum and ν is the frequency deviation of full width at half maximum. After the sample inserts into the optical resonator, the pulse repetition rates are observed a finite shift corresponding the change of optical path length and can be expressed as:

$$\Delta f = f' - f = \frac{c}{2L'_{opt}} - \frac{c}{2L_{opt}}, \quad (4.3.1)$$

where L_{opt} is the optical path length with a sample inside. By measuring the shift of pulse repetition rate, the change of optical path length $\Delta L_{opt} = L'_{opt} - L_{opt}$ can be estimate. However, the difference of the optical path length is associated with the length and refractive index of crystal. Therefore, the refractive index will be obtained with a given crystal length. However the refractive index which estimated by a mode-locked pulse is called group index n_g [16], a convenient way for determining the refractive index n_p according to

$$n_g = n_p - \lambda \frac{dn_p}{d\lambda} \quad (4.3.2)$$

Here, we have measured three kinds of Nd³⁺-doped crystals with different host materials including Nd:YVO₄, Nd:GdVO₄, and Nd:YGdVO₄ and the self-mode-locked lasers are not only operating at 1064 nm but also operating at 1342 nm. Table 4.3.1 shows the experimental results for the measurement of ordinary refractive indexes and extraordinary refractive indexes at 1064 nm and 1342 nm. The refractive indexes measuring in this method are found to be agreement with the values that reported in the literatures [9-15]. Figure 4.3-1 demonstrates the experimental results for measuring the ordinary refractive index (n_o) and extraordinary refractive index (n_e) of Nd:YVO₄ with different doped concentration in the range of 0.2 - 0.8 at. %. There are three samples for each doped concentration. The ordinary refractive indexes are found in the range of 1.9997 - 2.0002 and the extraordinary refractive indexes are found in the range of 2.2232 - 2.2240 as a function of doped concentration. It can be seen that the crystals exhibit higher refractive index with the higher doped concentration and the variation are observed in the order of 10^{-4} ..

In the second part, we have measured the thermal optical coefficient of 0.1 at. % Nd:YVO₄ crystal with a length of 12 mm. In the experimental system, an oven is used for heating the crystal inside the optical cavity. By heating the crystal from 30 °C to 200 °C, the pulse repetition rate of the mode-locked laser was found to decrease gradually. The frequency shifts are resulted from the increase of the optical path

length caused by not only the thermal expansion of the crystal but also the refractive index variation. In generally, the optical path length of a resonator can be expressed by:

$$L_{opt} = L_{cav} + (n-1) \cdot l_c \quad (4.3.3)$$

where L_{cav} is the cavity length and n is the refractive index of the crystal. As the crystal is heated, the optical length path has changed and can be written as

$$L'_{opt} = L_{cav} + \left(n + \frac{dn}{dT} \Delta T - 1 \right) \cdot \left(1 + \frac{\alpha}{3} \cdot \Delta T \right) \cdot l_c, \quad (4.3.4)$$

where dn/dT is the thermal optical coefficient, α is the thermal expansion coefficient, and ΔT is the increase of temperature. Thus, the difference of the optical path length is obtained by

$$\Delta L_{opt} = \left(\frac{dn}{dt} + (n-1) \cdot \alpha \right) \cdot l_c \cdot \Delta T + \frac{dn}{dt} \cdot \alpha \cdot l_c \cdot \Delta T^2. \quad (4.3.5)$$

However, the last term in Eq. (4.3.4) is quite small usually and can be neglect. With the frequency shifts which were obtained experimentally, the difference of optical path length would be carrying out. Therefore, with the parameters $l_c = 12 \text{ mm}$, $n_o = 1.996$, $n_e = 2.223$, and $\alpha = 4.43 \times 10^{-6}/K$, the thermal optical coefficient can be found to be $7.6 \times 10^{-6}/K$ and $4.2 \times 10^{-6}/K$ for the direction perpendicular and parallel to the c-axis of crystal respectively. The experimental results are in good

Ch4 Measurements of Refractive Indexes and Thermal Optical Coefficient:
Application of Self-Mode-Locked Lasers

agreement with that reported in the literature (the value of thermal optical coefficient are $8.5 \times 10^{-6}/K$ and $3 \times 10^{-6}/K$, respectively, for a-axis and c-axis of Nd:YVO₄ crystal) [12].



Table. 4.3.1. The experimentally measuring refractive indexes for different material at operating wavelength of 1064 nm and 1342 nm.

Materials		$\lambda = 1064 \text{ nm}$		$\lambda = 1342 \text{ nm}$	
		n_o	n_e	n_o	n_e
Nd:YVO ₄	In this work	1.9508	2.1674	1.9423	2.1459
	Previous work	1.958	2.168 [12]	1.948	2.154 [14]
Nd:GdVO ₄	In this work	1.9770	2.1888	1.9583	2.1687
	Previous work	1.972	2.192 [13]	1.9640	2.1808 [11]
Nd:GdYVO ₄	In this work	2.0055	2.2342	1.9789	2.1968
	Previous work				
		n_y	n_z	n_y	n_z
KTP	In this work	1.7761	1.8705	1.7655	1.8554
	Previous work	1.7958	1.8872 [15]	1.7685	1.8536 [15]

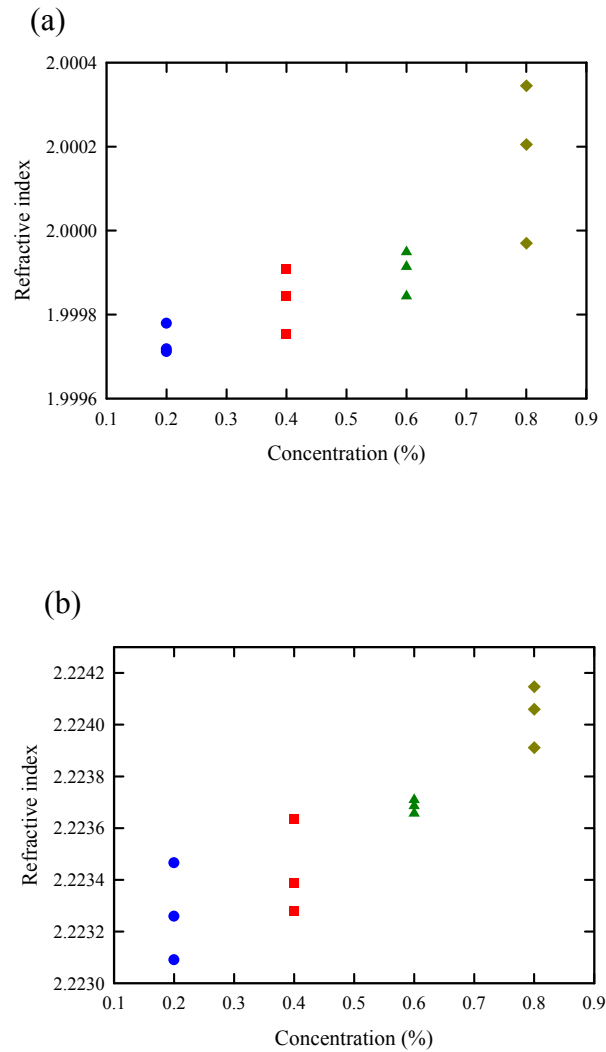


Fig. 4.3-1. The experimental results for measuring refractive indexes of Nd:YVO₄ with different doped concentrations. (a) For ordinary refractive indexes. (b) For extraordinary refractive indexes.

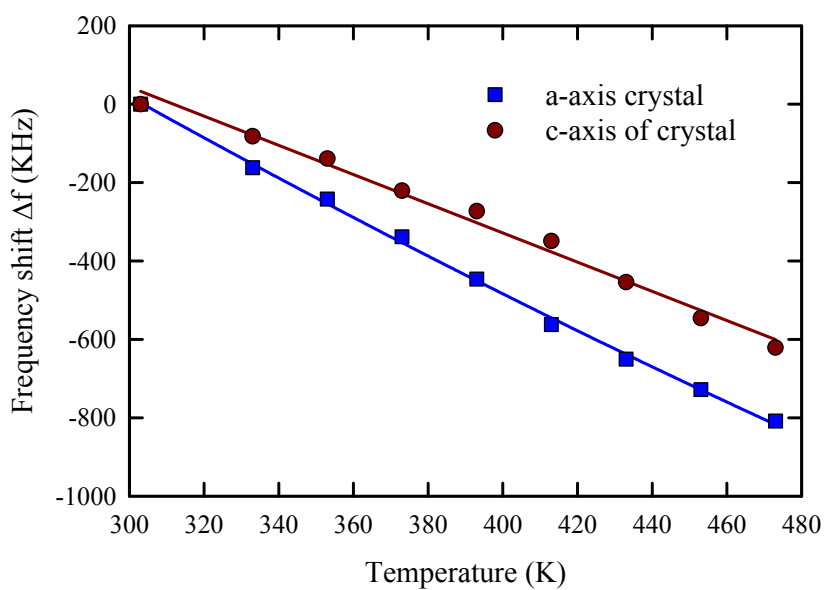


Fig. 4.3-2. Frequency shift versus the temperature of oven.

4.4 Conclusion

In summary, we have demonstrated a novel method to estimate the refractive indexes of several crystals. The idea is based on the shift of pulse repetition rate as a crystal is placed inside the optical cavity. The ordinary and extraordinary refractive indexes of Nd:YVO₄ crystals with different doped concentration are experimentally found that the refractive indexes increasing as the doped concentration increasing in the range from 0.2 at.% to 0.8 at.%. Besides, the Nd:YVO₄ crystal, we also measuring the Nd:GdVO₄ and Nd:GdYVO₄ crystals. The experimental results are consist with the value which have reported. By heating the crystal, the thermal optical coefficient of Nd:YVO₄ crystal are experimentally observed. The thermal optical coefficients are $7.6 \times 10^{-6}/K$ and $4.2 \times 10^{-6}/K$ at different axis of Nd:YVO₄ crystal and are in good agreement with the results in other reports.

References

- [1] M. E. Innocenzi, H. T. Yura, C. L. Fincher, and R. A. Fields, "Thermal modeling of continuous-wave end-pumped solid-state lasers," *Appl. Phys. Lett.* 56, 1831 (1990).
- [2] Y. F. Chen, T. M. Huang, C. F. Kao, C. L. Wang, and S. C. Wang, "Optimization in scaling fiber-coupled laser-diode end-pumped lasers to higher power: influence of thermal effect," *IEEE J. Quantum Electron.* 33, 1424 (1997).
- [3] Y. F. Chen, C. F. kao, T. M. Huang, C. L. Wang, and S. C. Wang, "Influence of thermal effect on output power optimization in fiber-coupled laser-diode end-pumped lasers," *IEEE J. Sel. Top. Quantum Electron.* 3, 29 (1997).
- [4] W. A. Clarkson, "Thermal effects and their mitigation in end-pumped solid-state lasers," *J. Phys. D* 34, 2381 (2001).
- [5] H. Zhang, J. Liu, J. Wang, C. Wang, L. Zhu, Z. Shao, X. Meng, X. Hu, M. Jiang, and Y. T. Chow, "Characterization of the laser crystal Nd:GdVO₄," *J. Opt. Soc. Am. B* 19, 18 (2002).
- [6] P. K. Mukhopadhyay, A. Nautiyal, P. K. Gupta, K. Ranganathan, J. George, S. K. Sharma, and T. P. S. Nathan, "Experimental determination of the thermo-optic coefficient (dn/dT) and the effective stimulated emission cross-section (σ_e) of an a-axis cut 1.-at.% doped Nd:GdVO₄ crystal at 1.06 μm wavelength," *Appl.*

References

- Phys. B 77, 81 (2003).
- [7] H. C. Liang, Ross C. C. Chen, Y. J. Huang, K. W. Su, and Y. F. Chen, "Compact efficient multi-GHz Kerr-lens mode-locked diode-pumped Nd:YVO₄ laser," *Opt. Express* 16, 21149 (2008).
- [8] H. C. Liang, Y. J. Huang, W. C. Huang, K. W. Su, and Y. F. Chen, "High-power, diode-end-pumped, multigigahertz self-mode-locked Nd:YVO₄ laser at 1342 nm," *Opt. Lett.* 35, 4 (2010).
- [9] B. H. T. Chai, G. Loutts, J. Lefaucheur, X. X. Zhang, P. Hong, and M. Bass, "Comparison of laser performance of Nd-doped YVO₄, GdVO₄, Ca₅(PO₄)₃F, Sr₅(PO₄)₃F and Ca₅(VO₄)₃F," in *Advanced Solid-State Lasers*, T. Y. Fan and B. H. T. Chai, eds., Vol. 20 of OSA Trends in Optics and Photonics Series (Optical Society of America, Washington, D. C., 1994), 41.
- [10] A. Sennaroglu, "Efficient continuous-wave operation of a diode-pumped Nd:YVO₄ laser at 1342 nm," *Opt. Commun.* 164, 191 (1999).
- [11] L. J. Qin, X. L. Meng, H. Y. Shen, L. Zhu, B. C. Xu, L. X. Huang, H. R. Xia, P. Zhao, and G. Zheng, "Thermal conductivity and refractive indices of Nd:GdVO₄ crystals," *Cryst. Res. Technol.* 38, 793 (2003).
- [12] J. C. Bermudez G., V. J. Pinto-Robledo, A. V. Kir'yanov, and M. J. Damzen, "The thermo-lensing effect in a grazing incidence, diode-side-pumped Nd:YVO₄ laser," *Opt. Commun.* 210, 75 (2002).
- [13] A. I. Zagumennyi, T. D. Zavartsev, P. A. Studenikin, I. A. Shcherbakov, F. Umyskov, P. A. Popov, and V. B. Ufimtsec, "Diode-pumped lasers based on GdVO₄ crystal," *Proc. SPIE* 2698, 182 (1996).

References

- [14] R. S. Conroy, A. J. Kemp, G. J. Friel, and B. D. Sinclair, "Microchip Nd :vanadate lasers at 1342 and 671 nm," *Opt. Lett.* 22, 1791 (1997).
- [15] H. Vanherzeele, J.D. Bierlein, and F. C. Zumsteg, "Index of refraction measurements and parametric generation in hydrothermally grown KTiOPO_4 ," *Appl. Opt.* 27, 3314 (1988).
- [16] H. G. Danielmeyer and H. P. Weber, "Direct measurement of the group velocity of light," *Phys. Rev. A* 3, 1708 (1971).




Chapter 5

Self-Mode-Locked

Lasers for High-Order

Transverse Modes

The logo of the University of South Florida is a circular seal. It features a central shield with a book and a torch. The year '1896' is inscribed on a banner at the bottom of the shield. The entire seal is surrounded by a decorative border.

5.1 Paraxial Approximation Maxwell's Equation : Wave Functions of Spherical Laser Cavity

It is well-known that the wave propagation in a source-free medium follows the Maxwell's equation which can be expressed as [1,2]

$$\begin{aligned}
 \nabla \cdot E &= 0 \\
 \nabla \cdot H &= 0 \\
 \nabla \times E &= -\mu \frac{\partial H}{\partial t} \\
 \nabla \times H &= \varepsilon \frac{\partial E}{\partial t}
 \end{aligned}
 \tag{5.1.1}$$


Thus, the electric field can be represented as

$$\nabla^2 E - \varepsilon \mu \frac{\partial^2 E}{\partial t^2} = 0.
 \tag{5.1.2}$$

Assume the electric field to be a monochromatic wave $E = E(x, y, z)e^{i\omega t}$, then the Eq.

(5.1.2) can be written as

$$(\nabla^2 + k^2)E(x, y, z) = 0,
 \tag{5.1.3}$$

this is the well-know Helmholtz equation, where k is the wave vector. For a wave which propagates primarily along the z direction, $E(x, y, z)$ can be written as

$$E(x, y, z) = u(x, y, z)e^{-ik_z z}, \quad (5.1.4)$$

where $\psi(x, y, z)$ is the transverse variation and k_z is the component of wave vector in z -direction. Substituting Eq. (5.1.4) into Eq. (5.1.3) and carrying out the result as

$$\left[\nabla_t^2 + \frac{\partial^2}{\partial z^2} - 2ik_z \frac{\partial}{\partial z} + (k^2 - k_z^2) \right] u(x, y, z) = 0, \quad (5.1.5)$$

where ∇_t^2 is transverse component of ∇^2 . In the paraxial condition, the term

$\frac{\partial^2}{\partial z^2} u(x, y, z)$ is quite small. Thus it is neglected to yield

$$\left[\nabla_t^2 - 2ik_z \frac{\partial}{\partial z} + k_t^2 \right] u(x, y, z) = 0, \quad (5.1.6)$$

where $k_t^2 = k^2 - k_z^2$ is the transverse component of wave vector. We assume that

$u(x, y, z) = \Psi(x, y)G(x, y, z)$, where $\Psi(x, y)$ is a scalar wave function which

describes the transverse variation of beam, $G(x, y, z)$ is a Gaussian spherical wave

function and can be expressed as

$$G(x, y, z) = \frac{z_R}{\sqrt{z^2 + z_R^2}} e^{-ikz \left[\frac{x^2 + y^2}{2(z^2 + z_R^2)} \right]}, \quad (5.1.7)$$

where z_R is the Rayleigh range which can be determined by the cavity. Substituting $u(x, y, z) = \Psi(x, y)G(x, y, z)$ into Eq. (5.1.6) and carrying out that

$$G(x, y, z)(\nabla_t^2 + k_t^2)\Psi(x, y) + \Psi(x, y)(\nabla_t^2 - 2ik_z \frac{\partial}{\partial z})G(x, y, z) + \nabla_t \Psi(x, y) \cdot \nabla_t G(x, y, z) = 0 \quad (5.1.8)$$

The third term in the Eq. (5.1.8) can considered approximately as

$$\nabla_t \Psi(x, y) \cdot \nabla_t G(x, y, z) \propto z \left[\frac{x}{2(z^2 + z_R^2)} \right], z \left[\frac{y}{2(z^2 + z_R^2)} \right], \quad (5.1.9)$$

and can be neglected. Thus after some algebra, the paraxial wave equation can be written as

$$G(x, y, z) \left[\nabla_t^2 + k_t^2 - \frac{(k_z z_R)^2 (x^2 + y^2)}{(z^2 + z_R^2)^2} \right] \Psi(x, y) = 0, \quad (5.1.10)$$

the $G(x, y, z)$ is a non-zero wave function, thus the Eq. (5.1.10) carrying out that

$$\left[\nabla_t^2 + k_t^2 - \frac{(k_z z_R)^2 (x^2 + y^2)}{(z^2 + z_R^2)^2} \right] \Psi(x, y) = 0, \quad (5.1.11)$$

and we simplify the Eq. (5.1.11) by using the functions $\omega(z) = \omega_0 \sqrt{1 + (z/z_R)^2}$ and $R(z) = z \left[1 + (z_R/z)^2 \right]$, where ω_0 is the minimum spot size at $z=0$, $\omega(z)$ is the spot size at arbitrary position, and $R(z)$ is the radius of the curvature. Therefore, we

carry out the general transverse wave equation of transverse variation and is show as

$$\left[\nabla_t^2 + k_t^2 - \frac{4(x^2 + y^2)}{\omega^2(z)} \right] \Psi(x, y) = 0. \quad (5.1.12)$$

In the following, we solve the Eq. (5.1.12) in the Cartesian coordinate and we can

express ∇_t^2 in term of two independent parts $\frac{\partial^2}{\partial x^2} + \frac{\partial^2}{\partial y^2}$. Thus we also can divide

the wave function into two different parts as $\Psi(x, y) = f(x)g(y)$, substituting into

Eq. (5.1.12) to obtain two independent equation as

$$\begin{aligned} \left[\frac{d^2}{dx^2} + k_x^2 - \frac{4x^2}{\omega^4(z)} \right] f(x) &= 0 \\ \left[\frac{d^2}{dy^2} + k_y^2 - \frac{4y^2}{\omega^4(z)} \right] g(y) &= 0 \end{aligned} \quad \text{, where } k_x^2 + k_y^2 = k_t^2 \quad (5.1.13)$$

Because these two differential equation are similar, we only need to analyze one of

them. Assume that $f(x) = s(x)e^{-\frac{x^2}{\omega^2(z)}}$ and $\xi = \frac{\sqrt{2}x}{\omega(z)}$, the differential equation can be

written as

$$\frac{d^2 s}{d\xi^2} - 2\xi \frac{ds}{d\xi} + \left[\frac{k_x^2 \omega^2(z)}{2} - 1 \right] s = 0. \quad (5.1.14)$$

This differential equation has the same form of Hermite function, thus the solution of

$f(x)$ is represented as $H_m\left(\frac{\sqrt{2}x}{\omega(z)}\right)e^{-\frac{x^2}{\omega^2(z)}}$, and the normalized transverse variation wave function in the Cartesian coordinate can be written as

$$\Psi_{m,n}(x, y) = \frac{1}{\sqrt{2^{m+n} \pi m! n!}} H_m\left(\frac{\sqrt{2}x}{\omega(z)}\right) H_n\left(\frac{\sqrt{2}y}{\omega(z)}\right) e^{-\frac{(x^2+y^2)}{\omega^2(z)}}, \quad (5.1.15)$$

and the wave vectors are $k_x^2 = \frac{2}{\omega^2(z)}(2m+1)$ and $k_y^2 = \frac{2}{\omega^2(z)}(2n+1)$, where $m, n = 0, 1, 2, \dots$. Here $H_m()$ is the m th order Hermite polynomial. Combine the wave vector of x-component and y-component and the approximation, the wave vector in z-direction (k_z) can be obtained by

$$k_z = \sqrt{k^2 - k_t^2} \doteq k\left(1 - \frac{k_t^2}{2k^2}\right) = k - \frac{2}{k\omega^2(z)}(1+m+n). \quad (5.1.16)$$

Using the relation of $\omega(z) = \omega_0 \sqrt{1 + (z/z_R)^2}$ and the integrate formula, the phase term $k_z z$ become

$$k_z z = kz - (1+m+n) \tan^{-1}\left(\frac{z}{z_R}\right), \quad (5.1.17)$$

where $-(1+m+n) \tan^{-1}\left(\frac{z}{z_R}\right)$ is the Gouy phase shift. In summary, the wave function in the Cartesian coordinate can be expressed as

$$E(x, y, z) = \Psi_{m,n}(x, y) \frac{\omega_0}{\omega(z)} e^{-ik \frac{(x^2+y^2)}{2R(z)}} e^{-i \left[kz - (1+m+n) \tan^{-1} \left(\frac{z}{z_R} \right) \right]} \quad (5.1.18)$$

This is the well-known Hermite-Gaussian (HG) modes.

Besides the Cartesian coordinate, the cylindrical coordinate is usually considered in the cylindrical symmetry system. Thus the Eq. (5.1.12) is written as

$$\left[\frac{\partial^2}{\partial r^2} + \frac{1}{r} \frac{\partial}{\partial r} + \frac{1}{r^2} \frac{\partial^2}{\partial \theta^2} + k_i^2 - \frac{4r^2}{\omega^4(z)} \right] \Psi(r, \theta) = 0, \quad (5.1.19)$$

where $r = \sqrt{x^2 + y^2}$, $\nabla_i^2 = \frac{\partial^2}{\partial r^2} + \frac{1}{r} \frac{\partial}{\partial r} + \frac{1}{r^2} \frac{\partial^2}{\partial \theta^2}$. We also divide the wave function into two independent function as $\Psi(r, \theta) = R(r)e^{i l \theta}$, then the Eq. (5.1.19) can carry out the result as

$$\left[\frac{\partial^2}{\partial r^2} + \frac{1}{r} \frac{\partial}{\partial r} - \frac{l^2}{r^2} + k_i^2 - \frac{4r^2}{\omega^4(z)} \right] R(r) = 0. \quad (5.1.20)$$

In order to solve the differential equation, we let $R(r) = r^{|l|} e^{-\frac{r^2}{\omega^2(z)}} F(r)$, and substitute into Eq. (5.1.20) to obtain

$$\frac{d^2 F}{dr^2} + \left[\frac{2|l|+1}{r} - 4 \frac{r}{\omega^2(z)} \right] \frac{dF}{dr} + \left[k_i^2 - 4 \frac{|l|+1}{\omega^2(z)} \right] F = 0. \quad (5.1.21)$$

Using the condition $\zeta = \frac{2r^2}{\omega^2(z)}$, the differential equation can be written as

$$\zeta \frac{d^2 F}{dt^2} + (|l|+1-t) \frac{dF}{dt} + \frac{1}{2} \left[\frac{\omega^2(z)}{4} k_t^2 - (|l|+1) \right] F = 0, \quad (5.1.22)$$

which is similar to the differential equation of Laguerre polynomial. As a result,

$k_t^2 = \frac{4}{\omega^2(z)} (2p + |l| + 1)$, where $p = 0, 1, 2, \dots$ and $l = 0, 1, 2, \dots$. Compare with the

results in Cartesian coordinate, the relation is $2p + |l| + 1 = 1 + m + n$. Therefore, the

normalized transverse variation wave function is shown as

$$\Psi_{p,l}(r, \theta) = \sqrt{\frac{2p!}{(1 + \delta_{0,l}) \pi (p+l)!}} \left[\frac{\sqrt{2}r}{\omega(z)} \right]^l L_p^l \left[\frac{2r^2}{\omega^2(z)} \right] e^{-\frac{r^2}{\omega^2(z)}} e^{il\theta}, \quad (5.1.23)$$

where $\delta_{0,l}$ is the delta function. In summary, the electric field in a cylindrical coordinate is expressed as

$$E(r, \theta, z) = \Psi_{p,l}(r, \theta) \frac{\omega_0}{\omega(z)} e^{-ik \frac{(x^2+y^2)}{2R(z)}} e^{-i \left[kz - (2p+|l|+1) \tan^{-1} \left(\frac{z}{z_R} \right) \right]} \quad (5.1.24)$$

This is the well-known Laguerre-Gaussian (LG) modes. Figure 5.1-1 demonstrates the numerical results of HG modes and LG modes.

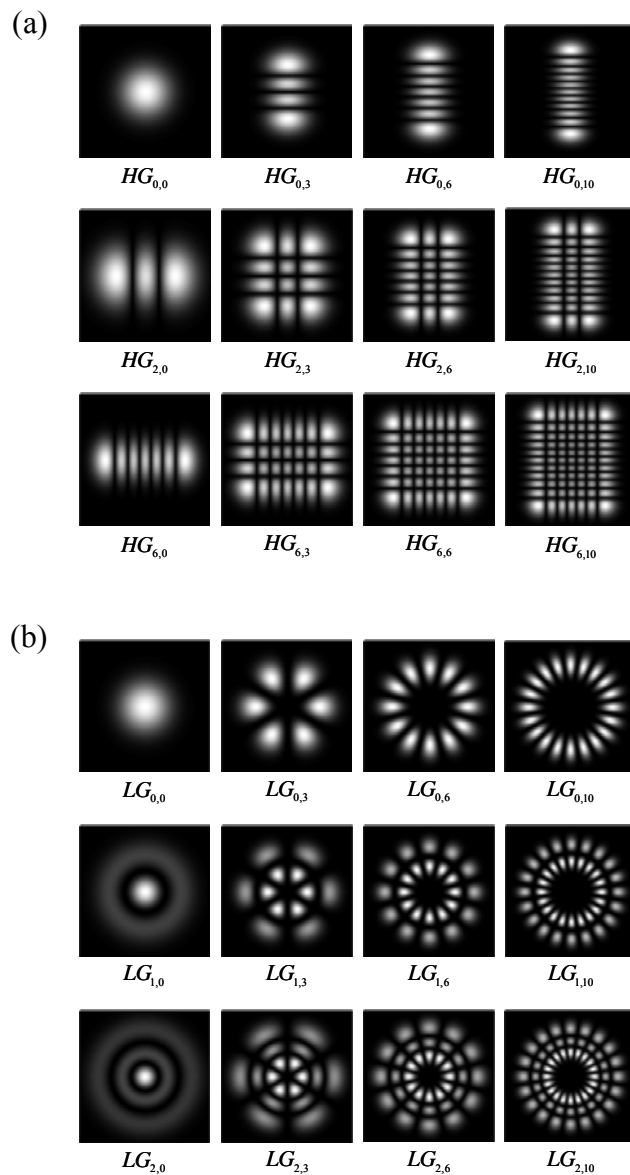


Fig. 5.1-1. (a) Hermite-Gaussian modes with different order (m,n) . (b) Standing wave of Laguerre-Gaussian modes with different order (p,l) .

5.2 Self-Mode-Locked High-Order Hermite-Gaussian

Nd:GdVO₄ Lasers

The stable self-mode-locked lasers have demonstrated in Chap. 2 with the laser gain medium of Nd:YVO₄ and Nd:GdVO₄ operated at either 1064 nm or 1342nm [3-5]. These self-mode-locked are all operated of the fundamental transverse mode (TEM_{0,m}). Because of the further understanding of self-mode-locked lasers by controlling the number of longitudinal lasing modes, it is possible to realize a self-mode-locked for high-order transverse modes. In this section, we have successful demonstrated the self-mode-locked high-order Hermite-Gaussian (HG) Nd:GdVO₄ lasers. With a pump power of 2.2 W, average output power for the TEM_{0,m} modes from $m = 0$ to $m = 9$ are among 780-350 mW at a repetition rate of 3.5 GHz. The mode-locked pulse width is in the range of 20-25 ps for various HG TEM_{0,m} modes. In addition to stable cw mode-locked pulses, we also observe the modulated mode-locked pulses with two adjacent transverse modes coupling.

5.2.1 Theoretical Simulation of Mode-Locked Lasers for High-Order Hermite-Gaussian Modes

Firstly, we have demonstrated the theoretical simulations of mode-locked lasers for high-order HG modes. The wave function for a high-order mode with index (m, n)

in a spherical cavity which mentioned above can be expressed as

$$E_{q,m,n}(x, y, z) = \frac{1}{\sqrt{2^{m+n} \pi m! n!}} \frac{\omega_0}{\omega(z)} e^{\frac{-(x^2+y^2)}{\omega^2(z)}} H_m\left(\frac{\sqrt{2}x}{\omega(z)}\right) H_n\left(\frac{\sqrt{2}y}{\omega(z)}\right) \times e^{-ik_{q,m,n} \frac{(x^2+y^2)}{2R(z)}} e^{-i\left[k_{q,m,n}z - (1+m+n)\tan^{-1}\left(\frac{z}{z_R}\right)\right]} \quad (5.2.1)$$

$$\text{with } k_{q,m,n} = \frac{\omega_{q,m,n}}{c} = \frac{\pi}{l_{cav}} \left[(q_0 + q) + \frac{1+m+n}{\pi} \cos^{-1} \sqrt{1 - \frac{l_{cav}}{R}} \right], \quad (5.2.2)$$

q_0 is the longitudinal resonant mode index, l_{cav} is the effective cavity length, and R is the radius of curvature. It can be seen that for a given transverse mode index (m, n) , there are a number of longitudinal modes which have the same transverse pattern. However, if the temporal dimension is considered, Eq. (5.2.1) will be written as

$$E_{q,m,n}(x, y, z) = \frac{1}{\sqrt{2^{m+n} \pi m! n!}} \frac{\omega_0}{\omega(z)} e^{\frac{-(x^2+y^2)}{\omega^2(z)}} H_m\left(\frac{\sqrt{2}x}{\omega(z)}\right) H_n\left(\frac{\sqrt{2}y}{\omega(z)}\right) \times e^{-ik_{q,m,n} \frac{(x^2+y^2)}{2R(z)}} e^{-ik_{q,m,n}(z-ct)} e^{i(1+m+n)\tan^{-1}\left(\frac{z}{z_R}\right)} \quad (5.2.3)$$

Figure 5.2-1 demonstrates the theoretical simulated results for the intensity $I_{q,m,n}(x, y, z) = |E_{q,m,n}(x, y, z)|^2$ where the value of parameters are as following: $q_0 = 10^3$, $q = 0$, $m = 0$, $n = 5$, $l_{cav} = 7.18 \text{ cm}$, $R = 10 \text{ cm}$, $t = 0$. It can be seen that the electric field in the cavity depicts a cw operation. However, when the M

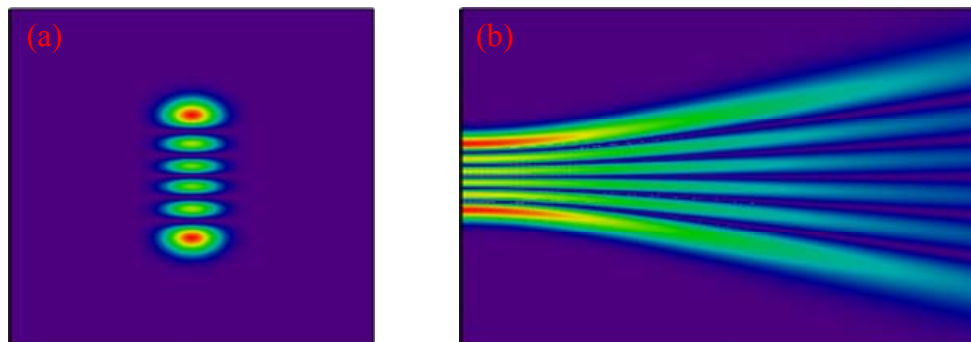


Fig. 5.2-1. The numerical results of the intensity $I_{0,0,5}(x, y, z)$. (a) In x-y plane. (b) In z-y plane.

longitudinal modes which have the same transverse distribution and with the phases identically zero, then the electric field will be considered the superposition of M longitudinal modes and is expressed as

$$E_{m,n}^M(x, y, z) = \sum_{q=0}^{M-1} E_{q,m,n}(x, y, z). \quad (5.2.4)$$

In frequency domain, the figure 5.2-2 describes the resonator frequencies for the mode-locking of fundamental mode and high-order transverse mode. Thus, for a non-zero (m, n) , Eq. (5.2.4) depicts the electric field for the mode-locking of high-order modes. As the result, the numerical simulation for a given $(m, n) = (0, 5)$ and $M = 20$ is describe in Fig. 5.2-3. It can be seen that, the output beam remains the transverse pattern in x-y plane at different time but in the y-z it demonstrates pulse distribution rather than continuous distribution.

5.2.2 Experimental Setup

Figure 5.2-4 depicts the experimental setup for the self-mode-locked high-order Hermite-Gaussian TEM_{0,m} laser with off-axis pumping scheme [6,7]. The cavity configuration is a simple concave-plano resonator. The active medium is a -cut 0.25 at.% Nd:GdVO₄ crystal with a length of 10 mm. Both end surfaces of the Nd:GdVO₄ crystal were antireflection coated at 1064 nm and wedged 2° to suppress the Fabry-Perot etalon effect. The laser crystal was wrapped with indium foil and mounted in a water-cooled copper holder. The water temperature was maintained

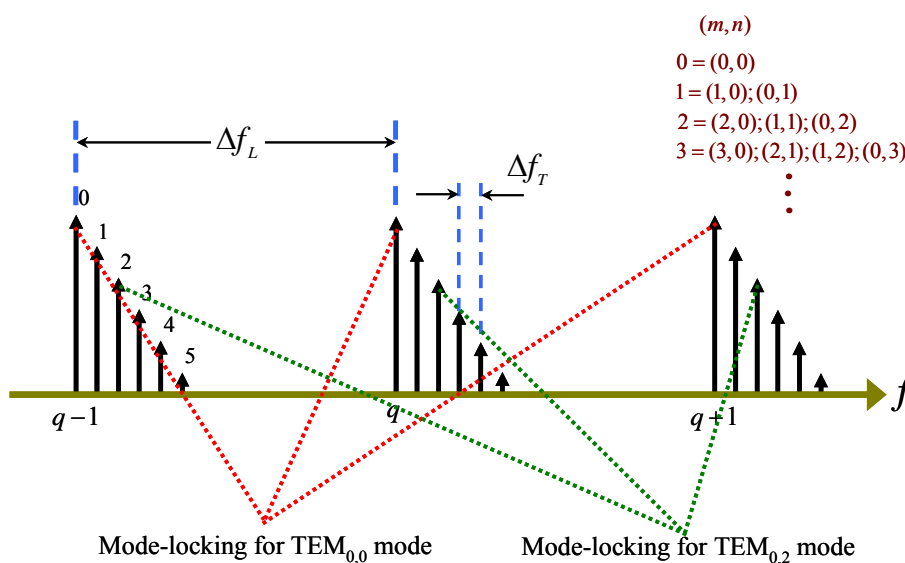


Fig. 5.2-2. Resonator frequencies, demonstrating the mode-locking for fundamental mode and high-order transverse mode.

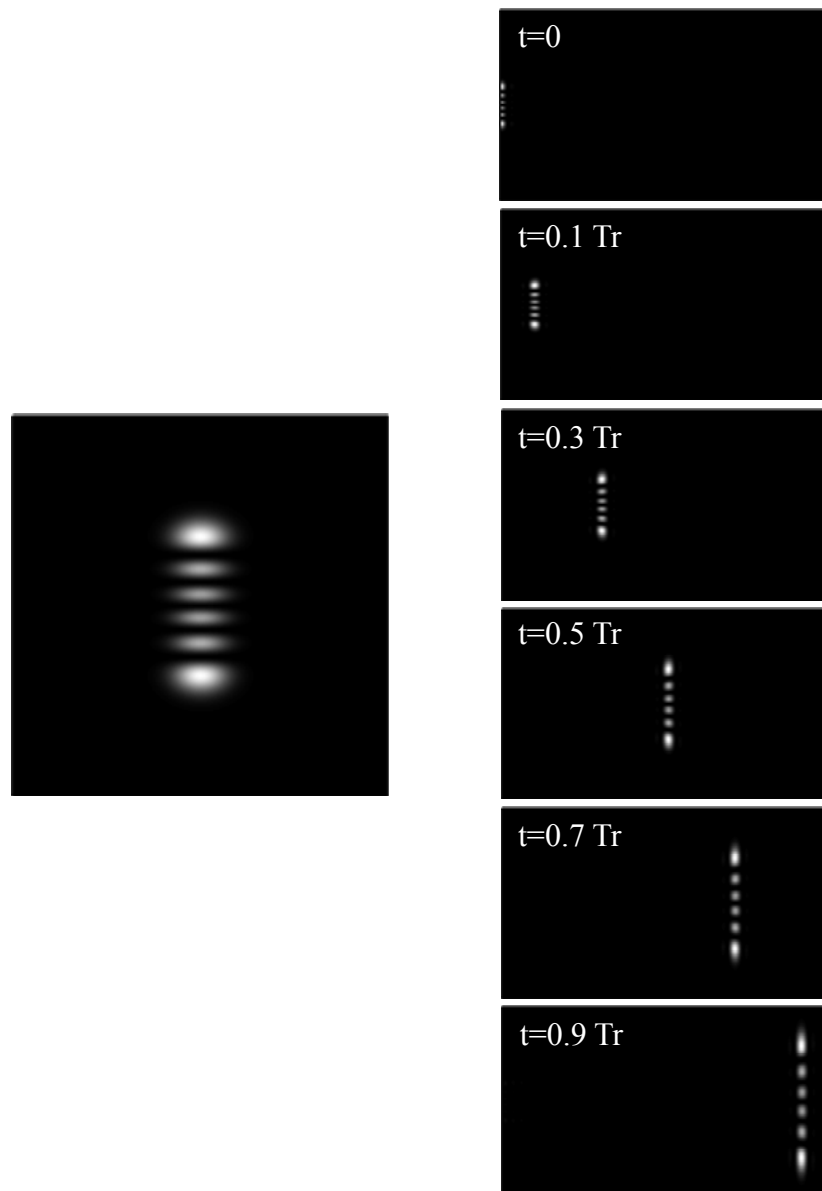


Fig. 5.2-3. The numerical results of the intensity of mode-locked laser for HG $TEM_{0,5}$. (a) In x-y plane. (b) In z-y plane at different time, where Tr is the round-trip time.

around 20 °C to ensure stable laser output. The laser crystal was placed very near (2–3 mm) the input mirror, which was a 50-cm radius-of-curvature concave mirror with antireflection coating at 808 nm on the entrance face and with high-reflectance coating at 1064 nm (>99.8%) and high transmittance coating at 808 nm on the second surface. A flat wedged output coupler with 15% transmission at 1064 nm was used throughout the experiment. The pump source was a 2.5-W 808-nm fiber-coupled laser diode with a core diameter of 100 μm and a numerical aperture of 0.16. Focusing lens with 25 mm focal length and 85% coupling efficiency was used to re-image the pump beam into the laser crystal. The average pump size was approximately 70 μm . The optical cavity length was set to be approximately 4.3 cm with the corresponding free spectral range (FSR) of 3.5 GHz.

5.2.3 Experimental Results and Discussions

First of all, the pumping beam was focused right on the optical axis of the laser cavity to obtain the maximum output power for the $\text{TEM}_{0,0}$ mode. After finely adjusting the cavity alignment, the laser output can be found to display a stable self-mode-locking operation. Subsequently the high-order HG $\text{TEM}_{0,m}$ mode-locked lasers can be generated with off-axis pumping [6,7]. The larger the off-axis displacement Δx is, the higher the HG $\text{TEM}_{0,m}$ order is. With varying Δx from 0 to 0.5 mm, the average output power was found to decrease gradually from 780 to 350 mW at a pump power of 2.2 W, as shown in Fig. 5.2-5. Ten HG $\text{TEM}_{0,m}$ modes were generated during the variation of off-axis displacement. The inset of Fig. 5.2-5 shows

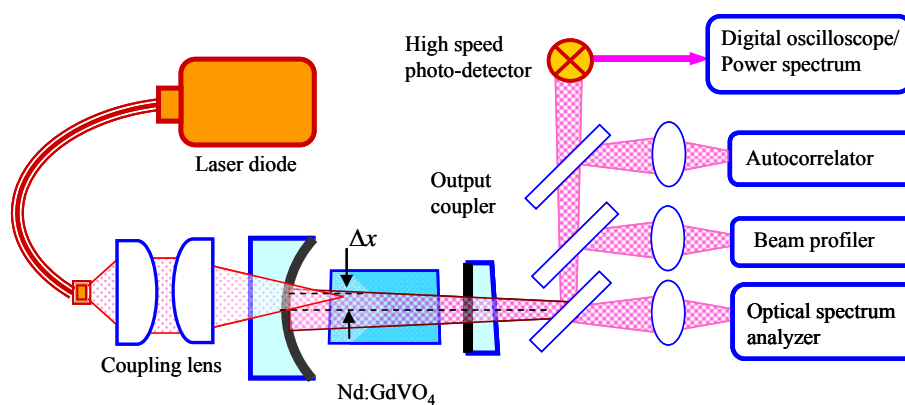


Fig. 5.2-4. Schematic of a self-mode-locked high-order HG TEM_{0,m} laser with an off-axis pumping scheme.

the experimental patterns that were measured using a camera of charged-coupled device (CCD). All observed HG TEM_{0,m} modes are found to be in the pure longitudinal mode-locking regime. Note that once the pump power reaches the lasing threshold, the laser system instantaneously steps into a stable mode-locked operation.

The mode-locked pulses were detected by a high-speed InGaAs photodetector (Electro-optics Technology Inc. ET-3500 with rise time 35 ps), whose output signal was connected to a digital oscilloscope (Agilent DSO 80000) with 10 GHz electrical bandwidth and a sampling interval of 25 ps. Figures 5.2-6(a) and 5.2-6(b) show the pulse trains for the TEM_{0,5} mode on two different timescales, one with time span of 5 ns, demonstrating mode-locked pulses, the other with time span of 5 μs, demonstrating the amplitude stability. It can be seen that the pulse trains display full modulation and the complete mode locking is achieved. The overall characteristics are almost the same as the results observed for the self-mode-locked fundamental TEM_{0,0} mode [3]. The pulse width at the cw mode-locked operation was measured with an autocorrelator (APE pulse check, Angewandte physik & Elektronik GmbH). Assuming the sech²-shaped temporal profile, the full width at half maximum (FWHM) was measured to be in the range of 20–25 ps for HG TEM_{0,m} modes with $m = 0 - 9$. The result for the TEM_{0,5} mode is shown in Fig. 5.2-6(c). The spectral information of the laser was monitored by a Fourier optical spectrum analyzer (Advantest, Q8347) that is constructed with a Michelson interferometer with resolution of 0.003 nm. Figure 5.2-6(d) shows the optical spectrum for the TEM_{0,5} mode. It can be seen that the longitudinal mode with 3.5 GHz is clearly resolved and

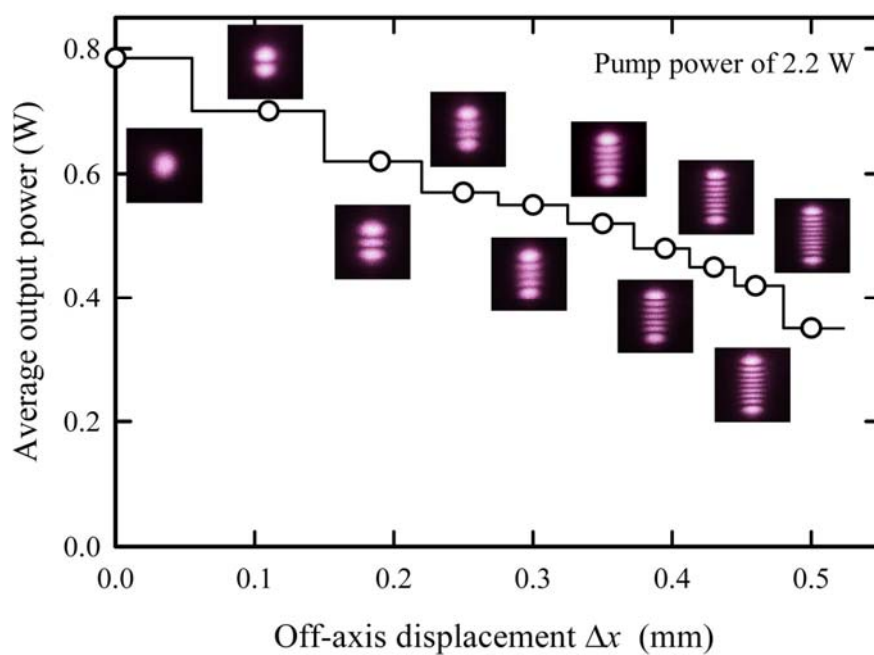


Fig. 5.2-5. Dependence of the average output power on the variation off-axis displacement. Insert, transverse patterns observed in the mode-locked operation.

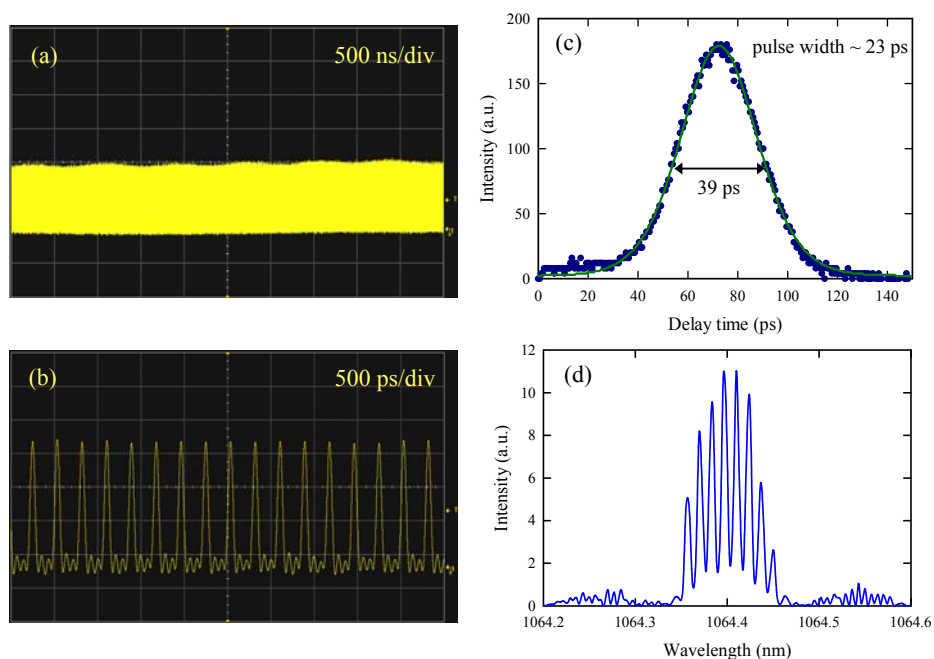


Fig. 5.2-6. Pulse trains on two different time scales. (a) time span of 5 μ s, demonstrating the amplitude oscillation. (b) Time span of 5 ns, demonstrating the mode-locked pulses. (c) Autocorrelation trace of the output pulses. (d) Corresponding optical spectrum. All results are for HG TEM_{0,5} mode.

the FWHM of the spectrum is approximately 0.1 nm. Consequently, the time-bandwidth product of the mode-locked pulse is approximately 0.4, indicating the pulses to be frequency chirped. On the whole, there are no significant difference for the mode-locked performances of the HG TEM_{0,m} modes with $m = 0 - 9$.

It is worth mentioned that once two adjacent modes are excited, the laser output was found to display a modulated pulse train with the modulated frequency was checked to come from the beat of the two adjacent modes. Fig. 5.2-7 reports the experimental result of the modulated mode-locked laser. In Fig. 5.2-7(a), the output transverse mode was not a fundamental mode but a superposition of the TEM₀₀ as well as TEM₁₀ modes. Although the laser output was found to display a modulated pulse train, the pulse repetition rate corresponded to the longitudinal frequency spacing was confirmed, as shown in Fig. 5.2-7(b) and Fig. 5.2-7(c). By measuring the transverse beat frequencies, it is observed that the beat frequencies are different at different pumped power. This phenomenon give rise to an interesting application for measuring the thermal lens using the transverse beat frequency method and will discuss in detail in the Chap. 6.

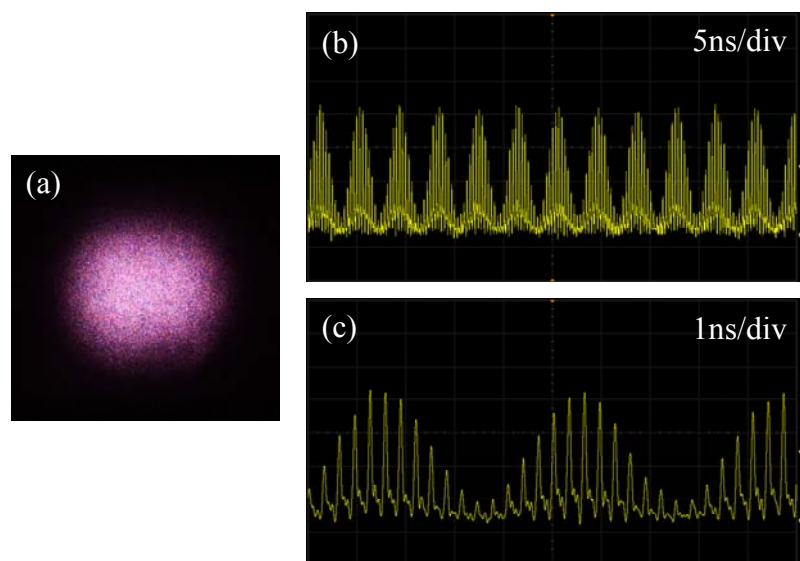


Fig. 5.2-7. Transverse patterns and pulse trains observed in the modulated mode-locked operation. (a) Transverse pattern of coupling TEM₀₀ and TEM₁₀ modes. (b) Time span of 50 ns, demonstrating, demonstrating the modulated amplitude oscillation. (c) Time span of 10 ns, demonstrating the mode-locked pulses.

5.3 Beam Transformation of Self-Mode-Locked Lasers : Picosecond Vortex Pulses

Optical vortex beams [8,9] that possess orbital angular momentum due to a phase singularity have been extensively used in the study of optical tweezers [10-14], trapping and guiding of cold atoms [15-17], rotational frequency shift [18,19], and entanglement states of photons [20]. Several devices that include spiral phase-plates [21], computer-generated holographic converters [22], and astigmatic mode converters (AMC) [23], have been successfully demonstrated to transform high-order Hermite-Gaussian (HG) modes into optical vortex beams.

Optical vortex pulses have recently been attracting great interest because they can open up various fields including high quality material processing [24], controllable specificity of chiral matter [25], and nonlinear frequency conversion [26]. Furthermore, optical vortex pulses in picosecond or femtosecond laser fields can be potentially utilized to investigate high field laser physics [27-30]. However, AMC cannot be used directly, since conventional mode-locked lasers are usually designed to emit the fundamental TEM_{00} mode. In the Sec. 5.2, we have successfully achieved self-mode-locked laser of high-order Hermite-Gaussian (HG) modes, it is possible to generate picosecond vortex pulses by converting the mode-locked HG beams. Here a cylindrical lens pair is used as a mode converter.

5.3.1 Experimental Setup

The input light sources are the self-mode-locked Hermite-Gaussian Nd:GdVO₄ lasers which demonstrated above. The average output power for the TEM_{0,m} modes from $m = 9$ to $m = 0$ were among 350-780 mW at a pump power of 2.2 W. Figure 5.3-1 depicts the experimental setup of a cylindrical-lens mode converter. The focal length of the cylindrical lenses was $f = 25 \text{ mm}$, and the distance was precisely adjusted to be $\sqrt{2}f$ for the operation of the $\pi/2$ converter. A HG beam must be aligned an angle 45° with the principal axes of the cylindrical lens pair, as shown in Fig. 5.3-1.

5.3.2 Experimental Results and Analysis

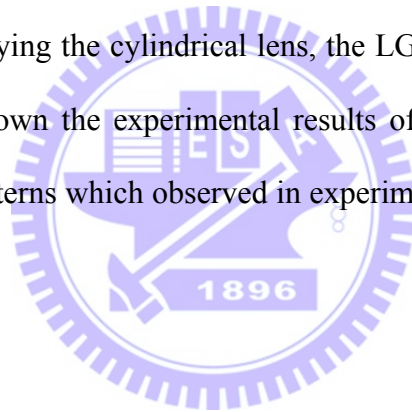
When a HG TEM_{0,m} modes have aligned at an angle of 45° with the principal axes of the cylindrical lens pair, the HG beams can be decomposed, using the relation between products of Hermite polynomials. The equation of this relation can be expressed

$$\Phi_{n,m}^{(HG)}\left(\frac{x+y}{\sqrt{2}}, \frac{x-y}{\sqrt{2}}, z\right) = \sum_{u=0}^{2\tilde{n}+\tilde{m}} B(\tilde{n}, \tilde{m}, u) \cdot \Phi_{2\tilde{n}+\tilde{m}-u,u}^{(HG)}(x, y, z) \quad (5.3.1)$$

where

$$B(\tilde{n}, \tilde{m}, u) = \frac{(-1)^u}{\sqrt{2^{2\tilde{n}+\tilde{m}}}} \sum_{\nu=0}^u \frac{(-1)^\nu \sqrt{(\tilde{n}+\tilde{m})!(2\tilde{n}+\tilde{m}-u)!u!}}{\nu!(u-\nu)!(\tilde{n}+\tilde{m}-\nu)!(\tilde{n}+\nu-u)!} \quad (5.3.2)$$

The relation of the indices between the HG modes and LG modes follows $n = \tilde{n}$ and $m = \tilde{n} + \tilde{m}$. Figure 5.3-2 demonstrates the numerical results of the decomposition of HG beams with transverse indices $(n, m) = (0, 1), (0, 2), (0, 3)$. Therefore, when a cylindrical lens pair is used to convert the HG modes to LG modes, it can rephase the terms in the decomposition. This can be done by exploiting the Gouy phase shift of a Gaussian mode. The cylindrical lens pair will give the $\pi/2$ phase shift as the separation of two cylindrical lenses. Thus, the HG beam can be reconstructed to LG beams. Fig. 5.3-3 depicts the numerical results of reconstruction of HG modes to generate LG modes. Applying the cylindrical lens, the LG modes are converted from HG modes. Fig. 5.3-4 shown the experimental results of the transformation of HG modes. The transverse patterns which observed in experimentally are in good with the theoretical estimation.



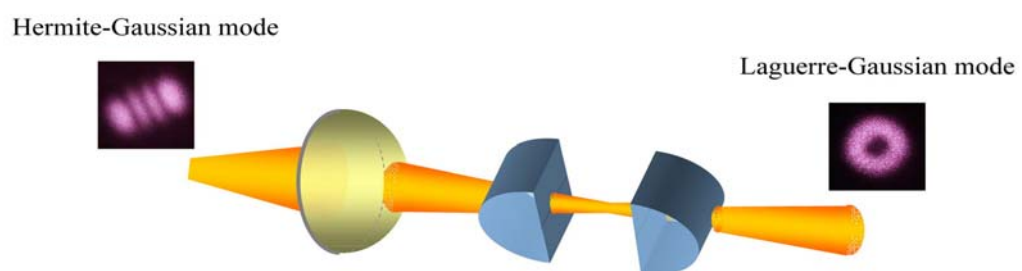


Fig. 5.3-1. Schematic of a cylindrical-lens mode converter.

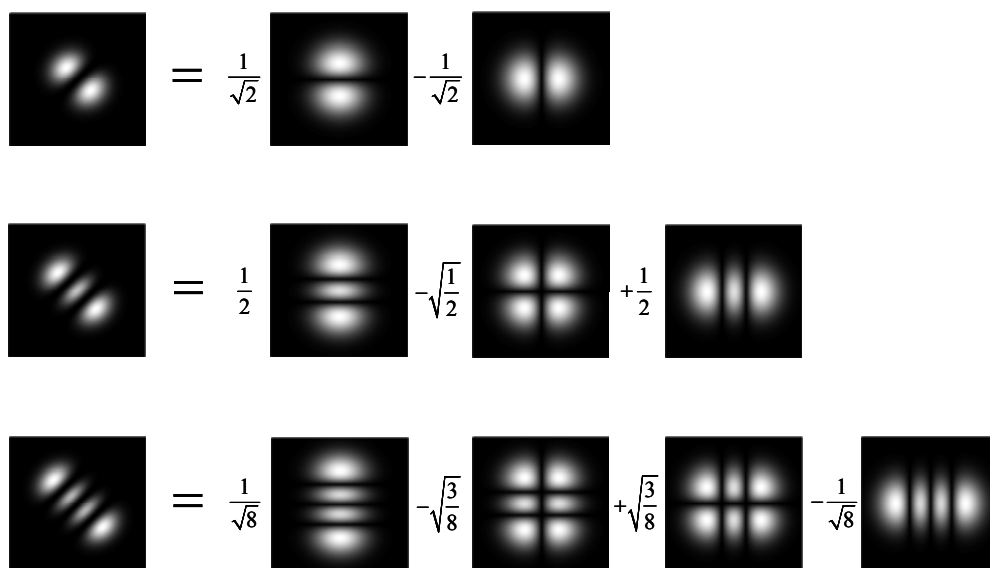


Fig. 5.3-2. Examples of the decomposition of HG beam with different transverse index $(n, m) = (0, 1), (0, 2), (0, 3)$.

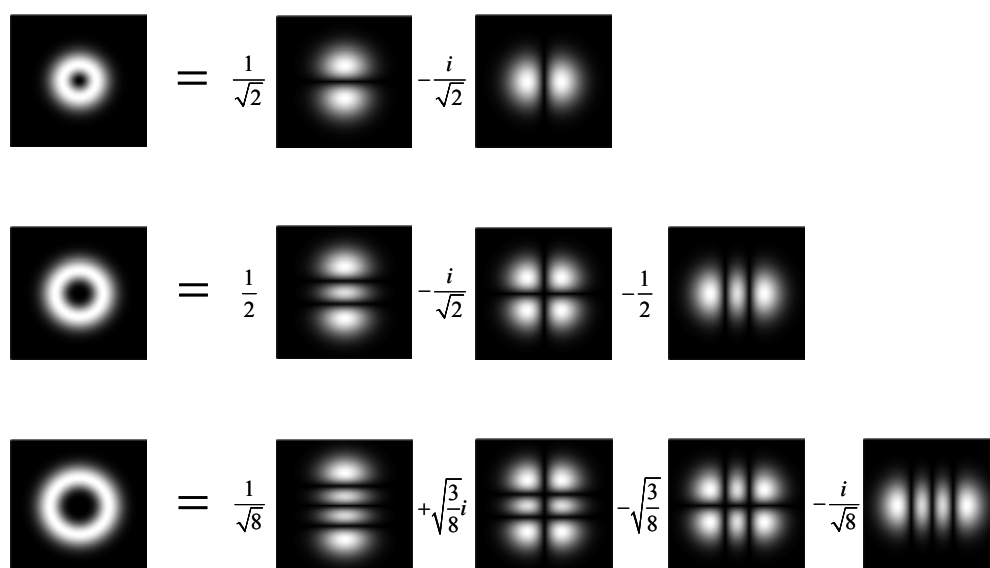


Fig. 5.3-3. The numerical simulations of the LG modes are reconstructed from HG modes.

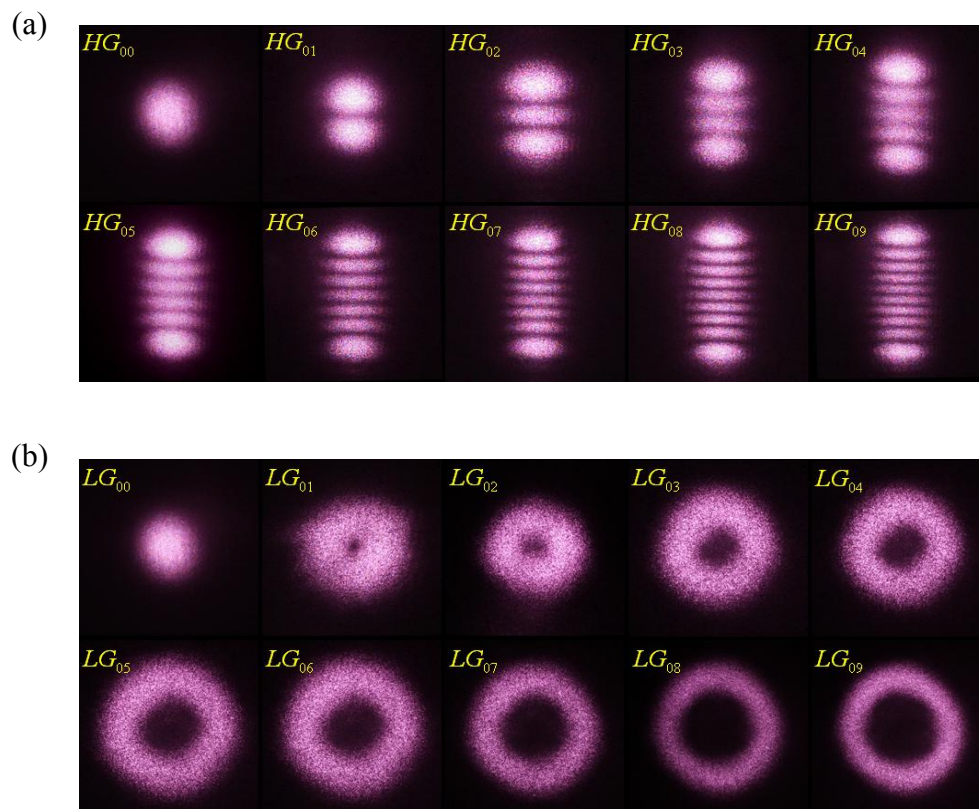
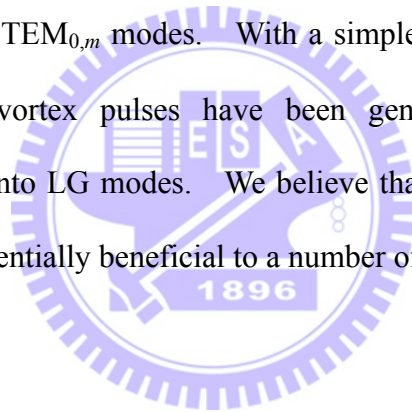


Fig. 5.3-4. The transformation of HG modes to LG modes. (a) The transverse patterns observed in mode-locked operation. (b) Corresponding transverse patterns after converting.

5.4 Conclusion

In this chapter, we have realized an efficient 3.5 GHz self-mode-locked Nd:GdVO₄ laser for HG TEM_{0,m} modes with $m = 0 - 9$. The average output powers for the TEM_{0,m} modes from $m = 0$ to $m = 9$ were between 780 and 350 mW at a pump power of 2.2 W. The mode-locked pulse width was found to be in the range of 20–25 ps for various HG TEM_{0,m} modes. With a simple cylindrical-lens converter, the picosecond optical vortex pulses have been generated by converting the mode-locked HG beams into LG modes. We believe that the generated picosecond optical vortices can be potentially beneficial to a number of applications.



References

- [1] D. J. Griffiths, *Introduction to Electrodynamics*, 3rd ed. (Prentice Hall, New Jersey, 1999).
- [2] J. D. Jackson, *Classical Electrodynamics*, 3rd ed. (Wiley, California, 1998).
- [3] H. C. Liang, R. C. C. Chen, Y. J. Huang, K. W. Su, and Y. F. Chen, "Compact efficient multi-GHz Kerr-lens mode-locked diode-pumped Nd:YVO₄ laser," *Opt. Express* 16, 21149 (2008).
- [4] H. C. Liang, H. L. Chang, W. C. Huang, K. W. Su, Y. F. Chen, and Y. T. Chen, "Self-mode-locked Nd:GdVO₄ laser with multi-GHz oscillations: manifestation of third-order nonlinearity," *Appl. Phys. B* 97, 451 (2009).
- [5] H. C. Liang, Y. J. Huang, W. C. Huang, K. W. Su, and Y. F. Chen, "High-power, diode-end-pumped, multigigahertz self-mode-locked Nd:YVO₄ laser at 1342 nm," *Opt. Lett.* 35, 4 (2010).
- [6] Y. F. Chen, T. M. Huang, C. F. Kao, C. L. Wang, and S. C. Wang, "Generation of Hermite-Gaussian modes in fiber-coupled laser-diode end-pumped lasers," *IEEE J. Quantum Electron.* 33, 1025 (1997).
- [7] H. Laabs and B. Ozygus, "Excitation of Hermite Gaussian modes in end-pumped solid-state lasers via off-axis pumping," *Opt. Laser Technol.* 28, 213 (1996).

References

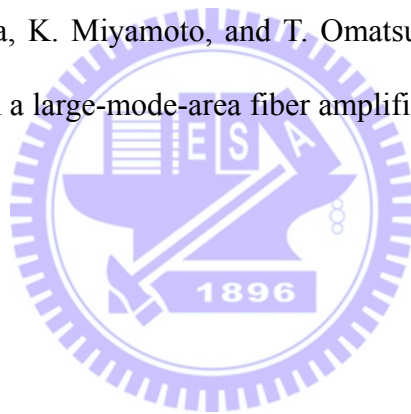
- [8] L. Allen, M. W. Beijersbergen, R. J. C. Spreeuw, and J. P. Woerdman, "Orbital angular momentum of light and the transformation of Laguerre-Gaussian laser modes," *Phys. Rev. A* 45, 8185 (1992).
- [9] G. Indebetouw, "Optical vortices and their propagation," *J. Mod. Opt.* 40, 73 (1993).
- [10] N. B. Simpson, K. Dholakia, L. Allen, and M. J. Padgett, "Mechanical equivalence of spin and orbital angular momentum of light: an optical spanner," *Opt. Lett.* 22, 52 (1997).
- [11] E. Santamato, A. Sasso, B. piccirillo, and A. Vella, "Optical angular momentum transfer to transparent isotropic particles using laser beam carrying zero average angular momentum," *Opt. Express* 10, 871 (2002).
- [12] K. T. Gahagan and G. A. Swartzlander, Jr., "Optical vortex trapping of particles," *Opt. Lett.* 21, 827 (1996).
- [13] L. Paterson, M. P. MacDonald, J. Arlt, W. Sibbett, P. E. Bryant, and K. Dholakia, "Controlled rotation of optically trapped microscopic particles," *Science* 292, 912 (2001).
- [14] M. P. MacDonald, K. Volke-Sepulveda, L. Paterson, J. Arlt, W. Sibbett, and K. Dholakia, "Revolving interference pattern for the rotation of optically trapped particles," *Opt. Commun.* 201, 21 (2002).
- [15] Y. Song, D. Milam, and W. T. Hill, "Long, narrow all-light atom guide," *Opt. Lett.* 24, 1805 (1999).
- [16] X. Xu, K. Kim, W. Jhe, and N. Kwon, "Efficient optical guiding of trapped cold atoms by a hollow laser beam," *Phy. Rev. A* 63, 063401 (2001).

References


- [17] T. Kuga, Y. Torii, N. Shiokawa, T. Hirano, Y. Shimizu, and H. Sasada, “Novel optical trap of atoms with a doughnut beam,” *Phys. Rev. Lett.* 78, 4713 (1997).
- [18] J. Courtial, D. A. Robertson, K. Dholakia, L. Allen, and M. J. Padgett, “Rotational frequency shift of a light beam,” *Phys. Rev. Lett.* 81, 4828 (1998).
- [19] J. Courtial, K. Dholakia, D. A. Robertson, L. Allen, and M. J. Padgett, “Measurement of the rotational frequency shift imparted to a rotating light beam possessing orbital angular momentum,” *Phys. Rev. Lett.* 80, 3217 (1998).
- [20] A. Mair, A. Vaziri, G. Weihs, and A. Zeilinger, “Entanglement of the orbital angular momentum states of photons,” *Nature* 412, 313 (2001).
- [21] M. W. Beijersbergen, R. P. C. Coerwinkel, M. Kristensen, and J. P. Woerdman, “Helical-wavefront laser beams produced with a spiral phase plate,” *Optics Commun.* 112, 321 (1994).
- [22] N. R. Heckenberg, R. McDuff, C. P. Smith, A. G. White, “Generation of optical phase singularities by computer-generated holograms,” *Opt. Lett.* 17, 221 (1992).
- [23] M. W. Beijersbergen, L. Allen, H. E. L. O. van der Veen, and J. P. Woerdman, “Astigmatic laser mode converters and transfer of orbital angular momentum,” *Opt. Commun.* 96, 123 (1993).
- [24] J. Hamazaki, R. Morita, K. Chujo, Y. Kobayashi, S. Tanda, and T. Omatsu, “Optical-vortex laser ablation,” *Opt. Express* 18, 2144 (2010).
- [25] D. L. Andrews, L. C. Dávila Romero, and M. Babiker, “On optical vortex interactions with chiral matter,” *Opt. Commun.* 237, 133 (2004).
- [26] K. Dholakia, N. B. Simpson, M. J. Padgett, and L. Allen, “Second-harmonic

References

- generation and the orbital angular momentum of light,” *Phys. Rev. A* 54, R3742 (1996).
- [27] I. G. Mariyenko, J. Strohaber, and C. J. G. J. Uiterwaal, “Creation of optical vortices in femtosecond pulses,” *Opt. Express* 13, 7599 (2005).
- [28] K. Bezuhanov, A. Dreischuh, G. G. Paulus, M. G. Schatzel and H. Walther, “Vortices in femtosecond laser fields,” *Opt. Lett.* 15, 1942 (2004).
- [29] G. B. Jung, K. Kanaya, and T. Omatsu, “Highly efficient phase-conjugation of a 1 μm pico-second Laguerre-Gaussian beam,” *Opt. Express* 14, 2250 (2006).
- [30] Y. Tanaka, M. Okida, K. Miyamoto, and T. Omatsu, “High power picosecond vortex laser based on a large-mode-area fiber amplifier,” *Opt. Express* 17, 14362 (2009).



Chapter 6



**Application of the Self-Mode-Locked
High-Order HG Modes Lasers:
Determination of Thermal Lens with
Transverse Beat Frequencies**

6.1 Thermal Lens Effect

A configuration of fiber-coupled laser-diode end-pumped in solid-state lasers offers the possibility of achieving high conversion efficiencies for fundamental mode operation. With the development of high-power AlGaAs/GaAs laser diode as pumping source, the compact efficient lasers are scaling to higher output power and are rapidly becoming preferred source in material-processing application. However, the localized absorption and high density of pumped power in laser crystal lead to heat accumulation and generate a temperature profile across the gain medium. This temperature distribution of laser crystal is represented by a parabolic-logarithmic function [1]. Then, the temperature profile gives rise to the variation of refractive index of gain medium and make laser crystal act as a lens which is known as thermal lens (TL) [2]. The pumped induced thermal lens is of primary importance because of its significant influence on laser stability, oscillation mode size, maximum achievable average power, efficiency, and output beam quality [3-5]. Therefore, thermal lens needs to be thoroughly understood and characterized for optimization of laser system.

Koechner is one of those who first studied the thermal lens in solid-state laser to analytically. He gave the analytical solution and the equation of the TL focal length for uniform heating in 1970 [6]. For Gaussian distribution of the pumping beam, the expression of TL focal length was presented by Innocenzi in 1990 [7]

$$f_{th} = \frac{\pi K \omega_p^2}{\xi P_{in} (dn/dT)} \left[\frac{1}{1 - \exp(-\alpha l_c)} \right] = \frac{C \omega_p^2}{P_{in}} \quad (6.1.1)$$

where K is the thermal conductivity, ω_p is the pumping spot size, P_{in} is the incident pump power, ξ is the fractional thermal loading, dn/dT is the thermal optical coefficient, α is the absorption coefficient, l_c is the length of gain medium, and C is the proportional constant. Many authors report the methods for measuring the TL focal length. In traditionally, the method utilizes a second laser as probe laser to scan the thermal lens is widely used in solid-state laser [6,8-12]. However, in the case of end-pumping, due to the small size of pumping profile and the particular geometric arrangement, this method is difficult to use. Several different approaches to measure and quantify the thermal lens have been developed. Among these interferometric methods [13-17], measuring output beam parameters [18], using unstable-resonator method [19-21], using degeneration cavity length [22], or employing transverse mode beat frequencies [23] have been used. The transverse beat frequencies method is very precise, even for very weak thermal lensing the technique also can be applied. Recently, the large third-order nonlinearities of Nd-doped vanadate crystals have been successfully exploited to achieve the self-starting self-mode-locking operation without the need of any additional components [24]. More recently, with the off-axis pumping scheme, an efficient multi-gigahertz self-mode-locked high-order Hermite-Gaussian (HG) Nd-doped GdVO₄ laser has been reported [25]. For a pure HG mode, the laser exhibits a near perfect stable

mode-locking operation. However, when the laser excited not only the fundamental mode but also the nearly high-order mode, the laser output pulse trains were modulated by the transverse beat frequency. In this Letter, we demonstrate for the first time the determination of focal power for the modulated self-mode-locked Nd:YVO₄ laser with the coupling of HG TEM_{0,0} and TEM_{1,0} modes. By measuring the transverse beating frequencies at different pumping power, the focal powers are calculated. With the pumped power from 0.7 W to 2.3 W, the transverse beat frequencies vary in the range of 275 - 336 MHz and the corresponding focal powers are 0.45 - 1.66 m⁻¹.



6.2 Experimental Setup

Figure 6.2-1 depicts the experiment setup for the modulated self-mode-locked laser with an off-axis pumping scheme [26,27]. The cavity configuration is a simple concave-plano resonator. The gain medium is a-cut 0.2 at. % Nd:YVO₄ crystal with a length of 10 mm. Both end surface of the Nd:YVO₄ crystal were antireflection coated at 1064 nm and wedge 2° to suppress the Fabry-Perot etalon effect. The laser crystal was wrapped with indium foil and mounted in a water-cooled copper holder. The water temperature was maintained around 20 °C to ensure stable laser output. The input mirror was a 504 mm radius-of-curvature concave mirror with antireflection coating at 808 nm on the entrance face and with high-reflectance coating at 1064 nm (>99.8%) and high transmittance coating at 808 nm on the second surface. The pump source was a 3-W 808-nm fiber-coupled laser diode with a core diameter of 100 μm and a numerical aperture of 0.16. Focusing lens with 25 mm focal length and 85% coupling efficiency was used to re-image the pump beam into the laser crystal. The average pump size was approximately 70 μm.

The optical cavity length was set to be approximately 4.5 cm with the corresponding free spectral range (FSR) of 3.3 GHz. The mode-locked pulses were detected by a high-speed InGaAs photodetector, whose output signal was connected to a digital oscilloscope with 12 GHz electrical bandwidth. At the same time, the output signal of the photodetector was also analyzed by an RF spectrum analyzer.

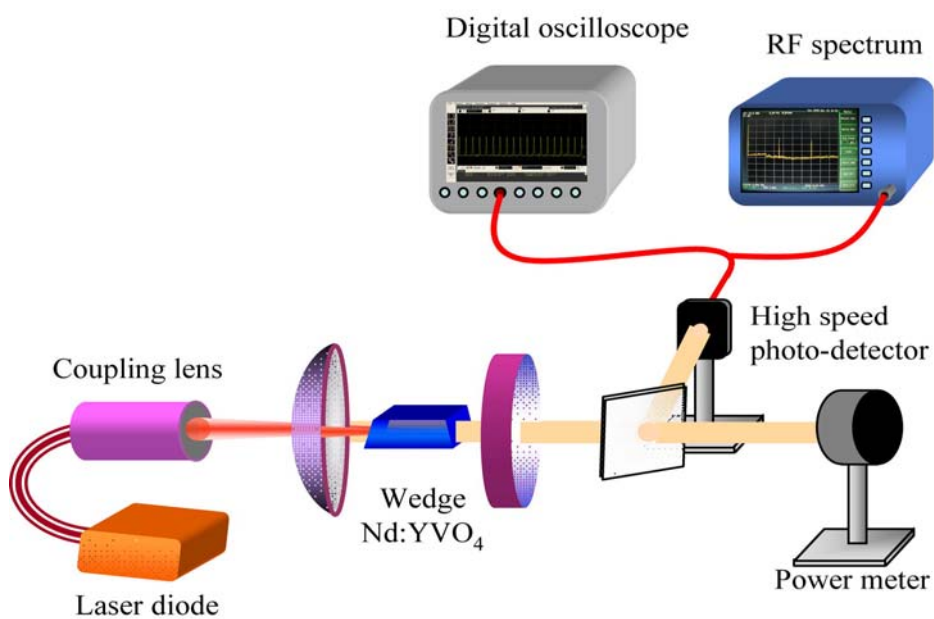


Fig. 6.2-1. Experimental setup of a self-mode-locked Nd:YVO₄ laser for measuring the focal length of thermal lens of the gain medium.

6.3 Experimental Results and Analysis

First of all, the pumping beam was focused right on the optical axis of laser cavity to obtain the maximum output power for fundamental mode. After finely adjusting the cavity alignment, the laser output can be found to display a stable self-mode-locked operation. Subsequently, the modulated mode-locked laser can be generated resulted from transverse modes coupling with off-axis pumping. Note that once the pumped power reaches the lasing threshold, the system instantaneously steps into the stable mode-locked operation. Figure 6.3-1(a) show the experimental pattern with on-axis pumping that was measuring using CCD camera. It can be seen that the laser demonstrates a nearly perfect fundamental mode output beam. The temporal trace for the operation of the single transverse mode is shown in Fig. 6.3-1(b). As shown in the figure, with time span of 50ns, the pulse trains display stable output, and the complete mode-locking is achieved. With off-axis pumping, the output transverse mode was not a fundamental mode but a superposition of the TEM_{00} as well as TEM_{10} modes, as shown in Fig. 6.3-1(c). When the laser excited not only the fundamental mode but also the nearly high-order mode, the stable mode-locked pulse trains were modulated. Figure 6.3-1(d) shows the pulse trains with time span 50 ns, demonstrating the modulated mode-locked pulses. Although the laser output was found to display a modulated pulse train, the pulse repetition rate corresponded to the longitudinal frequency spacing was confirmed and the modulated frequency was checked to come

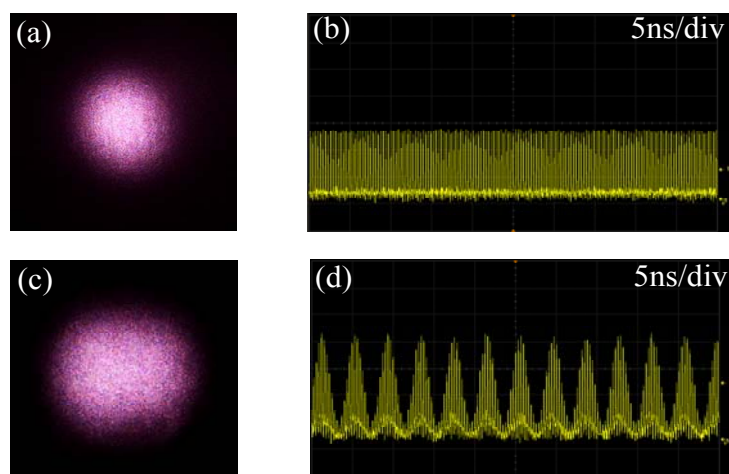


Fig. 6.3-1. Transverse patterns and pulse trains observed in the stable and modulated mode-locked operation. (a) Transverse pattern of pure fundamental mode. (b) Time span of 50 ns, demonstrating stable cw mode-locked pulses. (c) Transverse patterns of coupling TEM_{00} and TEM_{10} modes. (d) Time span of 50 ns demonstrating modulated mode-locked pulses.

from the beat of the TEM₀₀ and TEM₁₀ modes. The corresponding power spectrum is depicted in Fig. 6.3-2. With a pumping power of 1.1W, the center frequency is measured around 3.3GHz which corresponding to the pulse repetition rate. Beside the center frequency, the transverse beat frequencies are also detected with a frequency separation of 288 MHz. The relative frequency deviation, $\Delta\nu/\nu$, is experimentally found to be significantly small than 10^{-4} , where the ν is the center frequency of the power spectrum and $\Delta\nu$ is the frequency deviation of full width at half maximum.

The average output power of the modulated mode-locked laser is found approximately 95% of the stable cw mode-locked laser. Figure 6.3-3(a) depicts the average output powers versus the pumped power obtained at modulated mode-locked operation. The slope efficiency for the modulated mode-locked operation can be seen to be approximately up to 56% with respect to the incident pumped power, corresponding to an optical-optical efficiency of 50%. As shown in Fig. 6.3-3(b), the transverse beat frequencies versus the pumped powers are found in the range of 275-336 MHz. It can be seen that, even the weak thermal lensing resulted from low pumped power, the transverse beat frequencies are also can be experimentally measured.

In order to determination the focal power of thermal lens using the transverse beat frequencies method, the concept of the equivalent g-parameters are applied. An optical resonator with an internal thermal lens can be replaced by the empty cavity with the equivalent g-parameters g^* and the equivalent cavity length L^* which are given by [28]:

$$g_i^* = g_i - Dd_j \left(1 - \frac{d_i}{R_i}\right), \quad i, j = 1, 2; \quad i \neq j, \quad (6.3.1)$$

$$L^* = d_1 + d_2 - Dd_1d_2, \quad (6.3.2)$$

$$g_i = 1 - \frac{d_1 + d_2}{R_i} \quad (6.3.3)$$

where D is the focal power of thermal lens, R_i is the radius of curvature of mirror, and d_1, d_2 are the optical path length from the center of gain medium to the two mirrors. Because of the internal thermal lens, the Gaussian propagated with wavelength λ in the cavity exhibits two waists whose position and radius are a function of the focal length of thermal lens. By using the equivalent cavity parameter, the beam waists and their positions are given by

$$\omega_{0i} = \frac{\lambda L^*}{\pi} \cdot \frac{\sqrt{g_1^* \cdot g_2^* \cdot (1 - g_1^* g_2^*)}}{g_j^* \left(\frac{L^*}{R_i}\right) + g_i (1 - g_1^* g_2^*)}, \quad (6.3.4)$$

$$d_{0i} = L^* \cdot \frac{g_j^* \cdot \frac{L^*}{R_i}}{g_j^* \left(\frac{L^*}{R_i}\right)^2 + g_i (1 - g_1^* g_2^*)} \quad (6.4.5)$$

With the conventional model [29], the transverse beat frequencies of the adjacent modes can obtain from the Guoy phase shifts which are related to the Gaussian beam

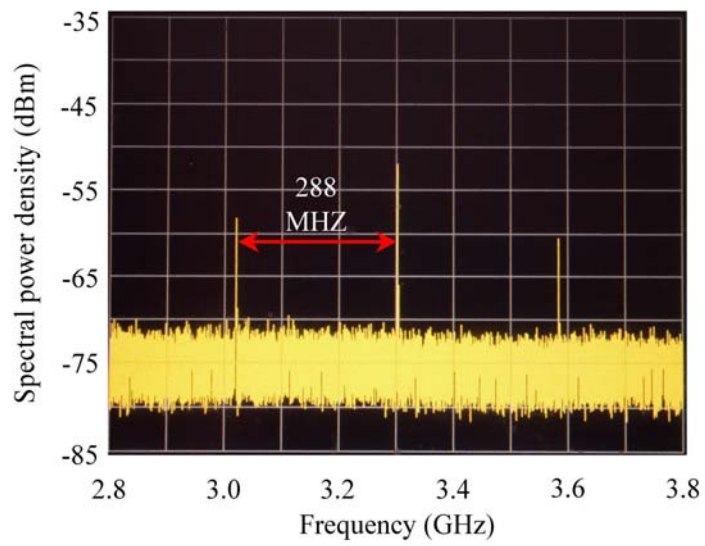


Fig. 6.3-2. Power spectrum in the modulated mode-locked operation.

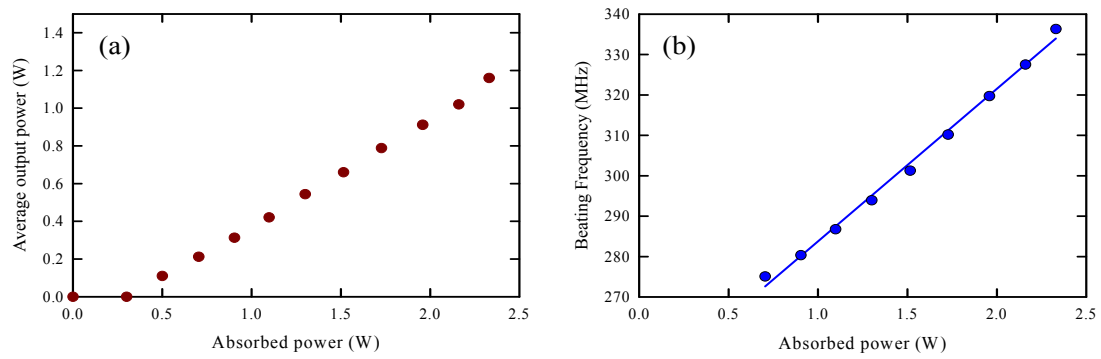


Fig. 6.3-3. (a) Average output powers versus the pumped powers for the modulated mode locking. (b) Transverse beat frequencies versus the pumped powers in the modulated mode-locked operation.

parameters by

$$\Theta(z) = \tan^{-1} \frac{z}{Z_0} \quad (6.3.6)$$

where $Z_0 = \pi\omega_0/\lambda$ is the Rayleigh range. After some algebra, the transverse beat frequencies can be expressed as

$$\Delta\nu_T(D) = \frac{1}{Tr \cdot \pi} \left[\tan^{-1} \left(\frac{d_1 - do_1}{Z_{o1}} \right) + \tan^{-1} \left(\frac{do_1}{Z_{o1}} \right) + \tan^{-1} \left(\frac{d_2 - do_2}{Z_{o2}} \right) + \tan^{-1} \left(\frac{do_2}{Z_{o2}} \right) \right] \quad (6.3.7)$$

where Tr is the round trip time. For modulated mode-locked at a beat frequency, the focal power are determined from the Eq. (6.3.7). The parameters used in the calculation are as follows: $d_1 = 14.3 \text{ mm}$, $d_2 = 13.3 \text{ mm}$, $R_1 = 504 \text{ mm}$, $R_2 = \infty$. Figure 6.3-4 shows the experimental results of the focal powers versus the pumped powers in the range of 0.45-1.66 m^{-1} . It can be seen that in Fig. 6.3-4, the focal powers of thermal lens can be determined precisely even for very weak thermal lens.

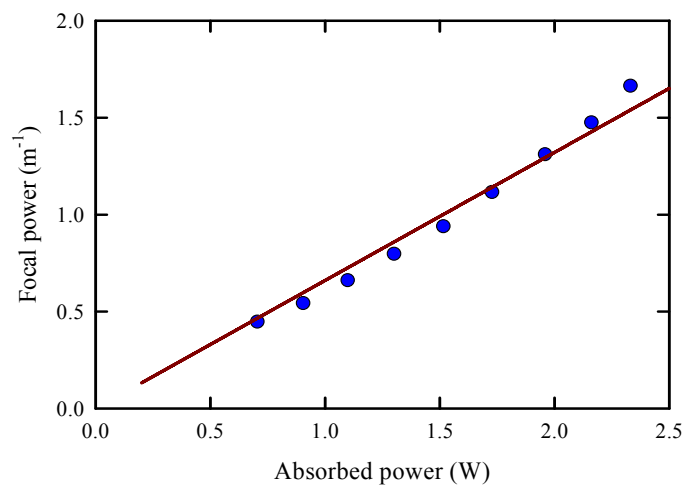
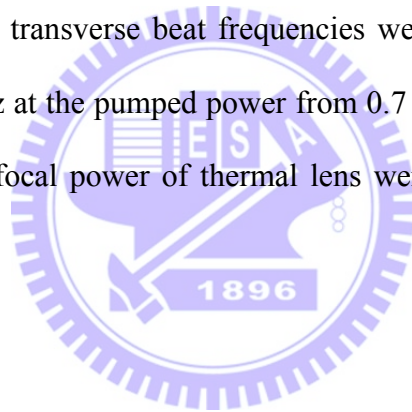


Fig. 6.3-4. The focal powers versus pumped powers in the modulated mode-locked laser.

6.4 Conclusion

In summary, we have demonstrated a modulated mode-locked Nd:YVO₄ laser with the combination of HG TEM_{0,0} and TEM_{1,0} modes. The modulated frequency was checked to come from the beat frequency of the TEM₀₀ and TEM₁₀ modes. By using the transverse beat frequency method [23], the focal powers of thermal lens can be determined precisely. The transverse beat frequencies were experimentally found in the range of 275-336 MHz at the pumped power from 0.7 to 2.3 W. Corresponding to the beat frequencies, the focal power of thermal lens were obtained in the range of 0.45-1.66 m⁻¹.



References

- [1] A. K. Cousins, "Temperature and thermal stress scaling in finite-length end-pumped laser rods," *IEEE J. Quantum Electron.* 28, 1057 (1992)
- [2] W. Koechner, *Solid-State Laser Engineering*, 6th ed. (Springer, New York, 2006), Chap. 7.
- [3] Y. F. Chen, T. M. Huang, C. F. Kao, C. L. Wang, and S. C. Wang, "Optimization in scaling fiber-coupling laser-diode end-pumped lasers to high power: influence of thermal effect," *IEEE Quantum Electron.* 33, 1424 (1997).
- [4] Y. F. Chen, C. F. kao, T. M. Huang, C. L. Wang, and S. C. Wang, "Influence of thermal effect on output power optimization in fiber-coupled laser-diode end-pumped lasers," *IEEE J. Sel. Top. Quantum Electron.* 3, 29 (1997).
- [5] W. A. Clarkson, "Thermal effects and their mitigation in end-pumped solid-state lasers," *J. Phys. D* 34, 2381 (2001).
- [6] W. Koechner, "Thermal lensing in a Nd:YAG laser rod," *Appl. Opt.* 9, 2548 (1970).
- [7] D. C. Burnham, "Simple measurement of thermal lensing effects in laser rods," *Appl. Opt.* 20, 1727 (1970).
- [8] D. C. Burnham, "Simple measurement of thermal lensing effects in laser rods," *Appl. Opt.* 20, 1727 (1970).

References

- [9] H. P. Kortz, R. Iffländer, and H. Weber, "Stability and beam divergence of multimode lasers with internal variable lenses," *Appl. Opt.* 20, 4124 (1981).
- [10] K. P. Driedger, W. Krause, and H. Weber, "Average refractive powers of an alexandrite rod," *Opt. Commun.* 57, 403 (1986).
- [11] D. S. Sumida, D. A. Rockwell, and M. S. Mangiv, "Energy storage and heating measurements in flashlamp-pumped Cr:Nd:GSGG and Nd:YAG," *IEEE J. Quantum Electron.* 24, 98 (1988).
- [12] R. Paugstadt and M. Bass, "A new technique for spatially resolved thermal lensing measurements," *Opt. Laser Technol.* 24, 151 (1992).
- [13] T. S. Chen, V. L. Anderson, and O. Kahan, "Measurements of heating and energy storage in diode pumped Nd:YAG," *IEEE J. Quantum Electron.* 26, 6 (1990).
- [14] S. C. Tidwell, J. F. Seamans, M. S. Bowers, and A. K. Cousins, "Scaling CW diode-end-pumped Nd:YAG lasers to high average powers," *IEEE J. Quantum Electron.* 28, 997 (1992).
- [15] C. Phstner, R. Weber, H. P. Weber, S. Merazzi, and R. Gruber, "Thermal beam distortions in end-pumped Nd:YAG, Nd:GSGG, and Nd:YLF rods," *IEEE J. Quantum Electron.* 30, 1605 (1994).
- [16] T. Omatsu, Y. kato, M. Shimosegawa, A. Hasegawa, and I. Ogura, "Thermal effects in laser diode pumped self-frequency-doubled $\text{Nd}_x\text{Y}_{1-x}\text{Al}_3(\text{BO}_3)_4$ (NYAB) microchip laser," *Opt. Commun.* 118, 302 (1995).
- [17] J. L. Blows, J. M. Dawes, and T. Omatsu, "Thermal lensing measurements in line-focus end-pumped neodymium yttrium aluminium garnet using holographic

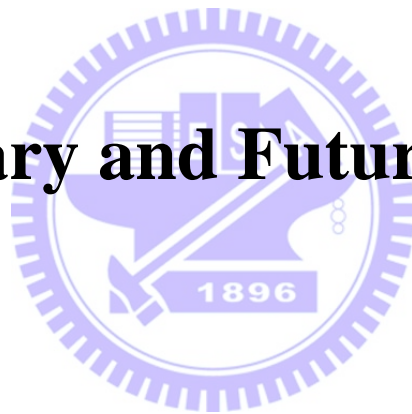
- lateral shearing interferometry,” *J. Appl. Phys.* 83, 2901 (1998).
- [18] B. Neuenschwander, R. Weber, and H. P. Weber, “Determination of the thermal lens in solid-state lasers with stable cavity,” *IEEE J. Quantum Electron.* 31, 1082 (1995).
- [19] D. G. Lancaster and J. M. Dawes, “Thermal-lens measurement of a quasi steady-state repetitively flashlamp-pumped Cr, Tm, Ho:YAG laser,” *Opt. Laser Technol.* 30, 103 (1998).
- [20] F. Song, C. Zhang, X. Ding, . Xu, G. Zhang, M. Leigh, and N. Peyghambarian, “Determination of thermal focal length and pumping radius in gain medium in laser-diode-pumped Nd:YVO₄ lasers,” *Appl. Phys. Lett.* 81, 2145 (2002).
- [21] Y. T. Chang, Y. P. Huang, K. W. Su, and Y. F. Chen, “Comparison of thermal lensing effects between single-end and double-end diffusion-bonded Nd:YVO₄ crystals for ${}^4F_{3/2} \rightarrow {}^4I_{11/2}$ and ${}^4F_{3/2} \rightarrow {}^4I_{13/2}$ transitions,” *Opt. Express* 16, 21155 (2008).
- [22] B. Ozygus, and Q. Zhang, “Thermal lens determination of end- pumped solid-state lasers using primary degeneration modes,” *Appl. Phys. Lett.* 71, 2590 (1997).
- [23] B. Ozygus and . Erhard, “Thermal lens determination of end- pumped solid-state lasers with transverse beat frequencies,” *Appl. Phys. Lett.* 67, 1361 (1995).
- [24] H. C. Liang, Ross C. C. Chen, Y. J. Huang, K. W. Su, and Y. F. Chen, “Compact efficient multi-GHz Kerr-lens mode-locked diode-pumped Nd:YVO₄ laser,” *Opt.*

References

- Express 16, 21149 (2008).
- [25] H. C. Liang, Y. J. Huang, Y. C. Lin, T. H. Lu, Y. F. Chen, and K. F. Huang, “Picosecond optical vortex converted from multigigahertz self-mode-locked high-order Hermite-Gaussian Nd:GdVO₄ lasers,” *Opt. Lett.* **34**, 3842 (2009).
- [26] Y. F. Chen, T. M. Huang, C.F. Kao, C. L. Wang, and S. C. Wang, “Generation of Hermite-Gaussian modes in fiber-coupled laser-diode end-pumped lasers,” *IEEE J. Quantum Electron.* **33**, 1025 (1997).
- [27] H. Laabs and B. Ozygus, “Excitation of Hermite Gaussian modes in end-pumped solid-state lasers via off-axis pumping,” *Opt. Laser Technol.* **28**, 213 (1996).
- [28] N. Hodgson and H. Weber, *Laser Resonators and Beam Propagation*, Second ed. (Springer, New York, 2005), Chap. 13.
- [29] A. E. Siegman, *Lasers*, (Mill Valley, California, 1986), Chap. 19.

Chapter 7

Summary and Future Work



7.1 Summary

In this work, we have studied the self-mode-locked lasers with a simplest linear cavity without the need of any additional elements and demonstrated the application of self-mode-locked lasers.

In chapter 2, we first introduce the compact efficient high power diode-end-pumped self-mode-locked lasers. In Sec. 2.1 the phenomena of spontaneous mode-locking (SML) are discussed. It points out that laser gain media with a large third-order nonlinearity are possible to be the promising host crystals for stable self-mode-locking. The wedge shapes of the laser gain medium and output coupler also played an important role for achieving a complete stable self-mode-locking. In Sec. 2.2 the experimental results of high-power multi-gigahertz self-mode-locked Nd:YVO₄ and Nd:GdVO₄ lasers at 1064 nm have been successfully demonstrated. For the Nd:YVO₄ laser, at a pumped power of 2.5 W, a maximum average output power of 0.8 W was obtained, which gives an optical conversion efficiency of 32%. The pulse width is generally less than 10 ps for the mode-locked frequency of 2-6 GHz. The experimental results of Nd:GdVO₄ laser are experimentally found to be similar to the Nd:YVO₄ laser. Besides the self-mode-locked lasers operating at the wavelength 1064 nm, the 1342 nm mode-locked Nd:YVO₄ laser is also demonstrated in Sec. 2.3. The average output power was up to 1.2 W at an incident pump power of 10.2 W,

which give an optical conversion efficiency of 11.7%. The pulse width was experimentally found as short as 11.5 ps and pulse repetition rate in the range of 2-6 GHz.

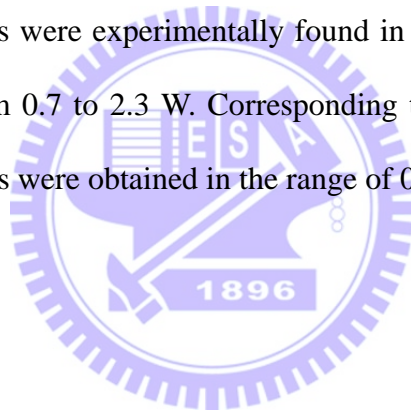
The technique of mode control for self-mode-locked lasers is important for achieving reliable self-mode-locking. In Sec. 3.3 we are experimentally found that by controlling the amount of spatial hole burning, the pulse width in the mode-locked lasers can be adjusted and the stability can be improved. In Sec. 3.4, considering the SHB effect, we have driven an analytical formula to establish the relationship between the number of longitudinal lasing modes and the crystal/mirror separation. The theoretical results are shown to be in good agreement with experimental observations.

Because of the further understanding of self-mode-locking and the achievement of reliable self-mode-locked laser, we have reported the application of self-mode-laser. In chapter 4, we have measured the refractive indexes of several crystals by estimating the pulse repetition rate shift. The experimental results are in good agreement with the results reported before. Besides, the refractive indexes of crystals, the thermal optical coefficients of Nd:YVO₄ are experimentally found by heating the crystals. The thermal optical coefficients are $7.6 \times 10^{-6}/K$ and $4.2 \times 10^{-6}/K$ at different axis of Nd:YVO₄ crystal.

In the Chap 5, we have investigated theoretical and experimental the self-mode-locked laser with transverse intensity distribution high order transverse modes. From the paraxial approximation Maxwell's equations, the wave functions of the spherical laser cavity can be obtained. In experimentally, we have realized an efficient 3.5 GHz self-mode-locked Nd:GdVO₄ laser for HG TEM_{0,m} modes with

$m = 0 - 9$. The average output powers for the $TEM_{0,m}$ modes from $m = 0$ to $m = 9$ were between 780 and 350 mW at a pump power of 2.2 W. With a simple cylindrical-lens converter, the picosecond optical vortex pulses have been generated by converting the mode-locked HG beams into LG modes.

As the discovery of the modulated mode-locked in high-order HG modes lasers, it can be applied to some applications. In Chap. 6, we have reported the determination of the thermal lens in diode-pumped mode-locked laser. By using the transverse beat frequency method, the focal powers of thermal lens can be determined precisely. The transverse beat frequencies were experimentally found in the range of 275-336 MHz at the pumped power from 0.7 to 2.3 W. Corresponding to the beat frequencies, the focal power of thermal lens were obtained in the range of 0.45-1.66 m⁻¹.



7.2 Future Works

One of our aims in this thesis is to study the self-mode-locked high-order Hermite-Gaussian (HG) Nd:YVO₄ lasers. Although, the spatial distribution in a general two-mirror laser cavity is commonly described in term of Hermite-Gaussian modes or Laguerre-Gaussian modes of the paraxial wave equation. However, when the optical cavity is aligned at a special cavity length which corresponds to the radii of curvature of mirrors, the dominating mode may be usually not any one of the pure HG modes or LG modes but can be alternatively viewed as multi-bounce Gaussian beams traveling in closed off-axis trajectories, which are called geometrical modes. Recently, several researchers reported that these geometrical modes closely resemble closed ray paths, and are the result of gain-guiding induced phase and frequency locking of Hermite-Gaussian mode. In additional, the experimental results have revealed that the stable mode-locked output pulse trains turn to modulated pulse trains when there are two adjacent transverse modes coupling. Therefore, it is possible to develop the lasers which are not only phase locking in the longitudinal modes but also phase locking in transverse modes. This topic is very important not only for understanding laser geometrical modes, but also providing analogous insight in to quantum ballistic transport in mesoscopic system. Our future researches will be focused on the self-mode-locked laser in geometrical modes.

Curriculum Vitae

Personal Data

Name: Hsing-Chih Liang

Sex: Male

Birthday: Oct. 26, 1982

Nationality: Taiwan (Republic of China)

Birthplace: Taoyuan County

E-mail: c2490111@gmail.com

jo3zpt@hotmail.com

Mobile Phone: 886-919-368073

Education

2005-2010 Ph.D. and M.S. in Department of Electrophysics, National
Chiao Tung University, Hsinchu, Taiwan.

2001-2005 B.S. in Department of Physics, National Cheng Kung
University, Tainan, Taiwan.

1998-2001 National Chung-Li Senior High School, Taoyuan, Taiwan.

Work Experience

2005-2008 T. A. of General Physics and Quantum Mechanics

Current Research Interests

Self-Mode-Locked Lasers

Vortex beams

Publication List

Journal papers

1. **H. C. Liang**, Y. J. Huang, W. C. Huang, K. W. Su, and Y. F. Chen, “High-power, diode-end-pumped, multigigahertz self-mode-locked Nd:YVO₄ laser at 1342 nm,” *Opt. Lett.* 35, 4 (2010).
2. **H. C. Liang**, Y. J. Huang, Y. C. Lin, T. H. Lu, Y. F. Chen, and K. F. Huang, “Picosecond optical vortex converted from multigigahertz self-mode-locked high-order Hermite-Gaussian Nd:GdVO₄ lasers” *Opt. Lett.* 34, 3842 (2009).
3. **H. C. Liang**, H. L. Chang, W. C. Huang, K. W. Su, Y. F. Chen, and Y. T. Chen, “Self-mode-locked Nd GdVO₄ laser with multi-GHz oscillations: manifestation of third-order nonlinearity,” *Appl. Phys. B* 97, 451 (2009).
4. **H. C. Liang**, Ross C. C. Chen, Y. J. Huang, K. W. Su, and Y. F. Chen, “Compact efficient multi-GHz Kerr-lens mode-locked diode-pumped Nd YVO₄ laser,” *Opt. Express* 16, 21149 (2008).
5. **H. C. Liang**, J. Y. Huang, K. W. Su, H. C. Lai, Y. F. Chen, K. F. Huang, H. J. Zhang, Y. J. Wang, and M. H. Jiang, “Passively Q-switched Yb³⁺ YCa₄O(BO₃)₃ laser with InGaAs quantum wells as a saturable absorbers,” *Appl. Opt.* 46, 2292 (2007).
6. T. H. Lu, Y. C. Lin, **H. C. Liang**, Y. J. Huang, Y. F. Chen, and K. F. Huang, “Observation of lasing modes with exotic localized wave patterns from astigmatic large-Fresnel-number cavities,” *Opt. Lett.* 35, 345 (2010).
7. J. Y. Huang, **H. C. Liang**, K. W. Su, and Y. F. Chen, “Analytical model for optimizing the parameters of an external passive Q-switch in a fiber laser,” *Appl. Opt.* 47, 2297 (2008).

8. J. Y. Huang, **H. C. Liang**, K. W. Su, and Y. F. Chen, “High power passively Q-switched ytterbium fiber laser with Cr⁴⁺ YAG as a saturable absorber,” *Opt. Express*. 15, 473 (2007).
9. Y. P. Huang, **H. C. Liang**, J. Y. Huang, K. W. Su, A. Li, Y. F. Chen, and K. F. Huang, “Semiconductor quantum-well saturable absorbers for efficient passive Q switching of a diode-pumped 946 nm NdYAG laser,” *Appl. Opt.* 46, 6273 (2007).
10. J. Y. Huang, **H. C. Liang**, K. W. Su, H. C. Lai, Y. F. Chen, and K. F. Huang, “InGaAs quantum well saturable absorbers for diode-pumped passively Q-switched Nd YAG laser at 1123 nm,” *Appl. Opt.* 46, 239 (2007).

Conferences

1. **H. C. Liang**, J. Y. Huang, S. C. Huang, K. W. Su, Y. F. Chen, and K. F. Huang, “AlGaInAs quantum wells as a saturable absorber,” *Solid State Lasers XVII, PW2008, Proceedings of SPIE 6871, San Jose, USA (Jan 2008)*.
2. J. Y. Huang, **H. C. Liang**, K. W. Su, and Y. F. Chen, “Analytical model for the design of external-cavity passively Q-switched fiber lasers” *Fiber Lasers V, PW2008, Proceedings of SPIE 6873, San Jose, USA (Jan 2008)*.
3. J. Y. Huang, **H. C. Liang**, K. W. Su, and Y. F. Chen, “Analytical model for optimizing the parameters of external cavity in passively Q-switched fiber lasers” *Annual Meeting of the Physical Society of Republic of China, HsinChu (Jan 2008)*
4. 黃哲彥, **梁興弛**, 蘇冠暉, 陳永富, 林志平, 陳思武, “光纖雷射研製計畫,” 96年度國防科技學術合作計畫成果發表會 55CS, 論文集 B-33, 龍潭 (2007).